



**BRNO UNIVERSITY OF TECHNOLOGY**  
VYSOKÉ UČENÍ TECHNICKÉ V BRNĚ



**FACULTY OF MECHANICAL ENGINEERING**  
**INSTITUTE OF PHYSICAL ENGINEERING**

FAKULTA STROJNÍHO INŽENÝRSTVÍ  
ÚSTAV FYZIKÁLNÍHO INŽENÝRSTVÍ

# **STUDY OF THE ELECTRON OPTICAL SYSTEMS WITH BROKEN ROTATIONAL SYMMETRY**

STUDIUM ELEKTRONOVĚ OPTICKÝCH SYSTÉMU S PORUŠENOU ROTAČNÍ SYMETRIÍ

**MASTER'S THESIS**  
DIPLOMOVÁ PRÁCE

**AUTHOR**  
AUTHOR PRÁCE

**Bc. MICHAL HORÁK**

**SUPERVISOR**  
VEDOUCÍ PRÁCE

**Ing. JAKUB ZLÁMAL, Ph.D.**

BRNO 2015



Vysoké učení technické v Brně, Fakulta strojního inženýrství

Ústav fyzikálního inženýrství

Akademický rok: 2014/2015

## **ZADÁNÍ DIPLOMOVÉ PRÁCE**

student(ka): Bc. Michal Horák

který/která studuje v **magisterském navazujícím studijním programu**

obor: **Fyzikální inženýrství a nanotechnologie (3901T043)**

Ředitel ústavu Vám v souladu se zákonem č.111/1998 o vysokých školách a se Studijním a zkušebním řádem VUT v Brně určuje následující téma diplomové práce:

### **Studium elektronově optických systémů s porušenou rotační symetrií**

v anglickém jazyce:

### **Study of the electron optical systems with broken rotational symmetry**

Stručná charakteristika problematiky úkolu:

Nepřesnosti výroby čoček v elektronově optických systémech vedou ke vzniku parazitických vad zobrazení, které je nutné korigovat pro dosažení požadované kvality obrazu. Tyto nepřesnosti se dají charakterizovat odchylkami od rotační symetrie. Simulovat jejich vliv potom můžeme buď využitím 3D softwaru pro výpočet polí, nebo použitím poruchové teorie za předpokladu, že odchylky jsou malé.

Cíle diplomové práce:

Prozkoumejte možnosti určení parazitních polí při porušení symetrie systému.

Porovnejte pole spočtená různými metodami.

Určete dosažitelnou přesnost určení poloh částic v těchto polích.

Seznam odborné literatury:

J. Orloff, Handbook of Charged Particle Optics, 2nd ed., CRC Press, New York, 2008, ISBN 978-1-4200-4554-3.

E. Munro, J. Vac. Sci. Technol. B 6 (1988) 941–948.

P. A. Sturrock, Philos. Trans. R. Soc. Lond. A 243 (1951) 387–429.

Vedoucí diplomové práce: Ing. Jakub Zlámal, Ph.D.

Termín odevzdání diplomové práce je stanoven časovým plánem akademického roku 2014/2015.

V Brně, dne 21.11.2014

L.S.

---

prof. RNDr. Tomáš Šíkola, CSc.  
Ředitel ústavu

---

prof. RNDr. Miroslav Doupovec, CSc., dr. h. c.  
Děkan fakulty

## Abstract

This thesis deals with computing of the magnetic lens with a perturbed pole piece due to manufacturing imperfections. Two possible ways of calculation are discussed — the perturbation theory and 3D computing. Three methods for evaluating axial multipole field functions from 3D fields are introduced. Beam spots in the image plane and aberration coefficients are computed and results obtained by the application of perturbation theory are compared to results evaluated from 3D simulations. Consequently, a suitability of using the perturbation theory is discussed.

## Key words

Magnetic lens, manufacturing imperfections, parasitic aberrations, axial multipole field function.

## Abstrakt

Tato práce se zabývá výpočty magnetické čočky, jejíž pólový nástavec má kvůli nepřesnostem ve výrobě porušenou rotační symetrii. Jsou diskutovány dva možné způsoby výpočtů — užití poruchové teorie a 3D výpočty. Jsou představeny tři metody pro určení osových multipólových funkcí ze 3D polí. Jsou vypočítány stopy svazku v obrazové rovině a aberrační koeficienty a výsledky získané použitím poruchové teorie jsou porovnány s výsledky vypočítanými s využitím 3D simulací. Na základě těchto výsledků je diskutována vhodnost použití poruchové teorie.

## Klíčová slova

Magnetická čočka, nepřesnosti výroby, vady seřízení, osové multipólové funkce.

HORÁK, M. *Studium elektronově optických systémů s porušenou rotační symetrií*.  
Brno: Vysoké učení technické v Brně, Fakulta strojíního inženýrství, 2015. 71 s. Vedoucí diplomové práce Ing. Jakub Zlámal, Ph.D.



## Prohlášení

Prohlašuji, že svou diplomovou práci na téma „Studium elektronově optických systému s porušenou rotační symetrií“ jsem vypracoval samostatně pod vedením vedoucího diplomové práce a s použitím odborné literatury a dalších informačních zdrojů, které jsou všechny citovány v práci a uvedeny v seznamu literatury na konci práce.

Jako autor uvedené diplomové práce dále prohlašuji, že v souvislosti s vytvořením této diplomové práce jsem neporušil autorská práva třetích osob, zejména jsem nezasáhl nedovoleným způsobem do cizích autorských práv osobnostních a jsem si plně vědom následků porušení ustanovení §11 a následujících autorského zákona č. 121/2000Sb., včetně možných trestněprávních důsledků vyplývajících z ustanovení §152 trestního zákona č. 140/1961Sb.

V Brně dne 29. 5. 2015

.....

Bc. Michal Horák



## **Acknowledgement**

The author kindly acknowledge Dr. Jakub Zlámal for efficient cooperation and supervising this diploma thesis. The institute of Physical engineering is acknowledged for providing computing capacity on servers and licenses of programs EOD, COMSOL, MATLAB, and Maple for purposes of this work. The author thanks to Dr. Vojtěch Uhlíř, Prof. Bohumila Lencová, and the staff of Campus Library for supplying full-text literature, Dr. Vladimír Kolařík for discussion and help with translation from French, and Prof. Jiří Komrška for discussion. This research was financially supported by FEI Company.



# Contents

<b>1</b>	<b>Introduction</b>	<b>13</b>
<b>2</b>	<b>Parasitic aberrations in literature</b>	<b>15</b>
2.1	Parasitic aberrations in books and book series . . . . .	15
2.2	Parasitic aberrations in papers . . . . .	17
<b>3</b>	<b>Radial expansion of static electromagnetic fields</b>	<b>21</b>
3.1	Electrostatic field . . . . .	21
3.2	Magnetic field . . . . .	23
<b>4</b>	<b>Calculation of perturbed electron optical systems</b>	<b>25</b>
4.1	Perturbation theory . . . . .	25
4.2	Computation of perturbed systems in 3D . . . . .	27
4.3	Short note comparing 2D and 3D computation . . . . .	28
<b>5</b>	<b>Calculation of axial multipole field functions from the 3D solution of the field</b>	<b>29</b>
5.1	Algorithm based on the Fourier series expansion . . . . .	29
5.2	Algorithm based on the wavelet interpolation . . . . .	32
5.3	Wavelet interpolation of radial dependence of Fourier components . . . . .	34
5.4	Magnetic lens with a hole in the pole piece . . . . .	35
<b>6</b>	<b>Calculation of optical properties of the lens with an elliptic polepiece</b>	<b>39</b>
6.1	Calculation of the magnetic field in lens . . . . .	39
6.2	Optimization of the axial field function evaluation . . . . .	41
6.3	Particle tracing . . . . .	44
6.4	Aberration coefficients . . . . .	45
<b>7</b>	<b>Comparison of 2D and 3D calculation of perturbed magnetic lens</b>	<b>47</b>
7.1	Influence of saturation of the magnetic lens with an elliptic pole piece . . . . .	47
7.2	Influence of the magnitude of ellipticity . . . . .	51
7.3	Misalignment of upper pole piece of the magnetic lens . . . . .	54
7.4	Tilt of upper pole piece of the magnetic lens . . . . .	57
<b>8</b>	<b>Conclusion</b>	<b>62</b>
	<b>Appendix A Useful relations</b>	<b>64</b>
A.1	Matrices used for the calculation of axial multipole field functions from the 3D solution of the field . . . . .	64
A.2	Derivatives of the Gaussian function . . . . .	66

<b>Appendix B</b>	<b>Fourier series of displaced circle and ellipse</b>	<b>67</b>
<b>Appendix C</b>	<b>Modification of the wavelet interpolation for 2D fields</b>	<b>69</b>
<b>References</b>		<b>71</b>
<b>List of symbols</b>		<b>75</b>
<b>List of figures</b>		<b>77</b>
<b>List of tables</b>		<b>80</b>

# 1 Introduction

Performance of electron optical system depends on the quality of lenses. Widely used electrostatic and magnetic lenses are rotationally symmetric, but limited machining precision of electrodes and pole pieces causes small perturbations from the ideal shape. These perturbations induce parasitic fields, which affect the optical properties of the lens. Aberrations corresponding to mechanical imperfections are usually called parasitic aberrations. Two principal ways to deal with the parasitic aberrations [1] are available. The first possibility is the "blind" alignment relying on improved manufacturing precision and alignment procedures to reduce the aberrations to acceptable values, without being able to address them individually. On the other hand, this very fine production could be too expensive for mass production of standard electron optical systems, especially if the device performance is affected negligibly by parasitic aberrations. The second alternative is to add optical elements that give the complete control over the aberrations. Therefore, often just basic correction by several stigmators and deflectors is sufficient. For the lens designer, it is important to estimate the influence of parasitic aberrations on system performance and suggest the adequate power of correcting elements. However, corrections of parasitic aberrations are beyond the interest of this thesis.

This thesis freely follows the doctoral thesis of Ondřej Sháněl [2] from 2014, the paper by Ondřej Sháněl, Jakub Zlámal and Martin Oral from 2014 [3], and contributions of Michal Horák and Jakub Zlámal [4], and Jakub Zlámal and Bohumila Lencová [5] to the 9<sup>th</sup> international conference on charged particle optics held in 2014 in Brno. The main goal of this work is to introduce a method for evaluating 3D electrostatic and magnetic fields and to explore the results obtained by two different techniques for computing electron optical systems with broken rotational symmetry — application of perturbation theory to 2D calculations and 3D simulations. As the result, limits of the perturbation theory are explored and illustrated on a magnetic objective lens.

Electron optical systems with broken rotational symmetry were studied for the first time by Walter Glaser in 1942 during his stay in Prague [6]. Parasitic aberrations of the magnetic objective lens caused by misaligned and elliptic pole pieces were observed and simply eliminated by James Hillier and E. G. Ramberg in 1946 [7]. The most important step in the progress of calculation of parasitic aberrations was the numerical computation of fields. The problems of tolerances of the shape of electron lenses graduate especially with the manufacturing of the high resolution microscopes. A brief survey of literature dealing with parasitic aberrations is in chapter 2.

A field close to the optical axis can be expressed using the axial potential in the case of an electrostatic lens, respectively using the axial magnetic flux density in the case of a magnetic lens [8, 9]. Analogously the parasitic fields can be simply characterized by the axial multipole field functions. The knowledge of the axial field functions is therefore important to evaluate optical properties and to interpolate the field using radial expansion of axial fields derived in chapter 3.

Nowadays, there are two possibilities of numerical computing of electron optical systems with broken rotational symmetry. The first alternative is to use the perturbation theory, which substitutes the impact of lens defects by parasitic multipole fields. The perturbation theory was introduced by François Berstein in 1948 [10] for electrostatic lenses and by Peter Andrew Sturrock in 1951 for magnetic lenses [11]. Three basic mechanical imperfections — ellipticity, misalignment, and tilt — of otherwise rotationally symmetric lens can be solved using the perturbation theory implemented in plug-in Tolerancing in Electron Optical Design (EOD) software [12]. The second possibility to study broken rotational symmetry is to use software, like COMSOL Multiphysics [13], which allows solving fully 3D problems. The simulation of perturbed electron optical systems is discussed in chapter 4.

It is advantageous for accurate interpolation and also evaluation of aberrations to substitute the 3D field by the axial multipole field functions. Computed 3D field can be affected by numerical errors. These errors are mainly caused by the shape and size of mesh elements. The mesh of 3D problems is not as dense as the mesh in 2D computation due to the memory consumption requirements in general. Three methods usable to determine the axial multipole field functions from the 3D field are introduced in chapter 5. Advantages and disadvantages of each method are shown on the example of the magnetic lens with a hole in the pole piece, discussed in [4].

Evaluation of the influence of different perturbations on optical properties of the magnetic lens consists of four parts — computation of the field, determination of the axial field functions, particle tracing, and calculation of relevant aberration coefficients. The process is introduced on the magnetic objective lens with an elliptic pole piece (chapter 6) and applied to different types of perturbations of the lens (chapter 7). The study is divided into four topics — influence of the saturation of magnetic materials (section 7.1), influence of the ellipticity magnitude (section 7.2), the misalignment magnitude (section 7.3), and the tilt magnitude (section 7.4) on optical properties of the magnetic objective lens. Finally, axial multipole field functions and selected aberration coefficients obtained using the perturbation theory in 2D are compared to the results evaluated using the 3D solution of the field to explore the limits of the perturbation theory.

## 2 Parasitic aberrations in literature

Despite that problems with manufacturing tolerances are interesting for companies producing modern sophisticated electron optics, there are only few recent publications dealing with the topic concerning parasitic aberrations. In the first section of this chapter are discussed contributions in books and book series, namely *Grundlagen der Elektronenoptik* by W. Glaser from 1952 [14], *Magnetic Electron Lenses* by P. W. Hawkes from 1982 [15], contribution of M. I. Yavor in *Advances in Electronics and Electron Physics* from 1993 [16], contribution of J. A. Rouse in *Advances in Optical and Electron Microscopy* from 1994 [17], *Principles of Electron Optics* by P. W. Hawkes and E. Kasper from 1996 [8], *Geometrical Charged-Particle Optics* by Harald H. Rose from 2009 [18], and *Handbook of Charged Particle Optics* by Jon Orloff from 2009 [9].

More interesting are papers, discussed in the second section of this chapter. Unfortunately it must be noticed that this survey is not complete. Only the papers accessible to the author are mentioned. Mainly papers introducing methods of calculation of perturbed lenses and related to round magnetic lenses are discussed. For more complete survey see [8, 9, 15, 16].

Algorithms for calculation of perturbed systems are covered by papers by F. Bertein from 1948 [10], by P. A. Sturrock from 1951 [11], by J. Janse from 1970 [19], by E. Munro from 1988 [20], by H. Liu and X. Zhu from 1990 [21], by C. J. Edgcombe from 1991 [22] by L. Wei and Y. Hanchun from 1999 [23], and by L. Wei and T. Yan from 1999 [24].

Round magnetic lenses are discussed in papers by J. Hillier and E. G. Ramberg from 1946 [7], by P. A. Sturrock from 1951 [11], by G. D. Archard from 1953 [25], by K. Amboss and J. C. E. Jennings from 1970 [26], and, finally, the most recent paper by O. Šáněl, J. Zlámal and M. Oral from 2014 [3].

### 2.1 Parasitic aberrations in books and book series

Walter Glaser covered electron optical systems with broken rotational symmetry in the first complex text dealing with electron optics *Grundlagen der Elektronenoptik* [14] (in German) from 1952 in chapter 22 on pages 452–466. Mainly the axial astigmatism is discussed.

Four chapters related to the parasitic aberrations are in the book *Magnetic Electron Lenses* edited by Peter W. Hawkes [15] from 1982. Section 1.5 on pages 50–51 is a brief and general introduction with a list of references. Section 2.1.2 on pages 60–61 covers Fourier series expansions of the scalar potential. The principle of the numerical treatment of lenses with small perturbations of the rotational symmetry is discussed in the section 2.6.1 on pages 105–106. And in the section 3.2 on pages 124–125 are useful notes about the field distribution in unsaturated and saturated lenses.

M. I. Yavor [16] in his chapter in *Advances in Electronics and Electron Physics* from 1993 presented an overview of methods for calculation of parasitic aberrations. Two dif-

ferent types of defects are introduced – manufacturing imperfections of electron optical elements leading to perturbations of their electromagnetic fields and displacements of elements relative to their nominal position. Effects of weak electromagnetic field disturbances on charged particle trajectories are discussed using equations for relativistic trajectories in a narrow beam with an arbitrary optical axis. An electrostatic lens with one elliptic electrode and a weakly disturbed inhomogeneous magnetic and electrostatic sector fields are discussed as examples. Four general methods for calculation of the perturbation due to electrode or pole piece distortions are summarized – an exact conformal mapping, Bertein’s perturbation method, a coordinate frame variation method, and a method of integral equations in variations.

The exact conformal mapping provides in some special cases an exact analytical expressions for field variations. The electrostatic field distribution in a cylindrical capacitor with a misaligned electrode is treated as an example.

Bertein’s perturbation method was the first application of the perturbation theory to investigate the parasitic aberrations in electron optical systems. Aberrations caused by small deformations of round lens electrodes are studied. This method is suitable only if a distortion of the boundary of electrodes, the distorted electrodes, and the potential distribution at the boundary are smooth.

Instead of determining a field potential disturbance at the ideal positions of electrode surfaces, as it is done in the Bertein’s perturbation theory, an appropriate coordinate frame – slightly different from the initial one – can be found, so that distorted electrodes take the perfect form in this new coordinate frame. This is the main idea of the coordinate frame variation method. Two examples are treated – a round immersion electrostatic lens with slightly elliptical electrodes and again the cylindrical capacitor with a misaligned electrode.

The electrostatic potential can be calculated as an integral of the surface charge density over all points on the surface of an electrode. If the variation of perturbed charge density is defined, the perturbation of the electrostatic potential at an arbitrary point inside the system can be determined. This is the principle of the method of integral equations in variations.

In the final part a field disturbance in electrostatic and magnetic sector analyzers is treated and several applications of approximate conformal mappings are discussed. Also a survey of literature related to the topic of parasitic aberrations is included.

John A. Rouse [17] in his chapter in *Advances in Optical and Electron Microscopy* from 1994 introduced software packages for 3D computer modelling of electron optical systems. The most important part is one of the tests of the software, which is the tolerance calculation for electric and magnetic lenses with elliptical defects. The comparison of results produced by the perturbation theory and 3D field computation is done. The first example is a bipotential lens. The bore radius of the lens is 20 mm and the elliptical defect is 1 mm. The astigmatism coefficient is determined by the distance between the positions where two perpendicular planes focus. The difference between 3D computation and the perturbation theory is below 0.5 %. The second example is a test of magnetic lens. The bore radius of the lens is 10 mm and the elliptical defect is from 0.5 mm to 5 mm. The astigmatism coefficients are computed by aberration integral. If the elliptic defect is 0.5 mm, the results of both methods are more less the same, respectively the difference is below 0.5 %. The difference rises with an increase of the defect. If the elliptic defect is 1 mm, the difference is approximately 5 %. This seems to be the limit of the perturbation theory. However, the usual elliptical defects are far below 0.1 mm with bore radius in units of mm, so the perturbation theory seems to be sufficiently precise for practical use.

The classical book *Principles of Electron Optics* by Peter W. Hawkes and Erwin Kasper [8] from 1996 covers in the chapter 31 on pages 470–479 the problems of parasitic aberrations. The most important conclusions are that the eccentricities in the sense of shift and tilt are producing very weak dipole fields, which can cause a very small lateral deflection of the whole electron beam. Ellipticity of pole pieces or electrodes causes quadrupole field producing an astigmatism. But there is much more important information, like the section 31.3 concerning numerical determination of parasitic aberrations, discussed in a friendly way. Also a short survey of pioneering contributions from 1940s and 1950s on page 471 can be useful.

In *Geometrical Charged-Particle Optics* by Harald H. Rose [18] from 2009 is the section 8.4.4 on pages 264–269 dealing with parasitic aberrations of quadrupole-octupole systems.

In the most recent *Handbook of Charged Particle Optics* edited by Jon Orloff [9] from 2009 can be found a nice survey of the literature, some basic information, and a table of different notations for the parasitic aberration coefficients of lenses in the section 6.5 on pages 291–293 and for electrostatic lenses in the section 5.3.4 on pages 190–191.

## 2.2 Parasitic aberrations in papers

James Hillier and E. G. Ramberg [7] observed astigmatism caused by misaligned and elliptic pole pieces. Simple compensating screws were implemented into the pole piece of the lens to correct these aberrations and to increase the quality of the image.

François Bertein [10] introduced the first application of the perturbation theory to the perturbed electrostatic systems. Real electron optical systems have perturbations from the ideal shape caused by inaccurate shape and alignment. Perturbations of the field can be expanded into the Fourier series and replaced by additional multipole potentials. Misalignment, in the sense of decentralization, is replaced by additional dipole field and causes a beam shift. However, Bertein did not consider aberrations, which are caused by the dipole field and affect the beam profile, like coma, therefore Bertein does not consider the misalignment to be a serious problem. Ellipticity is substituted by additional quadrupole field and causes an astigmatism. Perturbations with three-fold symmetry are much weaker than the perturbations with two-fold symmetry as the ellipticity. Finally, perturbations with four-fold and higher symmetry are negligible. Consequently, according to Bertein, the most important perturbation is the ellipticity of an electrode. Several electrostatic lenses with different shapes of electrodes are discussed.

Peter Andrew Sturrock [11] treated the mathematical problem of connection of parasitic aberrations to their causative machining defects. A computational procedure is set out for ascribing tolerances to a proposed lens design. The method may be divided into two parts. The first part is established for obtaining the perturbation of scalar magnetic potential from the known perturbation of its equipotential surfaces, assuming that the pole pieces are the magnetic scalar potential equipotentials. The second part covers the deduction of aberrations. Two classes of mechanical defects are introduced – misalignment, which means the misalignment of the individual axes of the pole pieces, and distortion, which means the deviation of the pole pieces from its ideal rotationally symmetric shape. Field perturbations and aberrations due to elliptic distortions, eccentricity and orientation are covered. It is shown that ellipticity and corrugation causes astigmatism. Eccentricity and misorientation causes astigmatism and coma. As an example the effect of ellipticity of bore of an idealized magnetic lens is discussed for the two cases – symmetrical and antisymmetrical. The symmetrical ellipticity means the major axes of

both pole pieces are parallel. In the case of the antisymmetrical ellipticity, the major axes of both pole pieces are perpendicular.

G. D. Archard [25] shortly summarized the most important results of previous studies and dealt with the application of the Sturrock's perturbation theory. The theory is applied to several practical cases with an attempt to the generalization and tries to specify mechanical tolerances with respect to the resolution due to aberrations. The criterion is to reach the resolution affected by coma, astigmatism, spherical aberration, and diffraction not much worse than the resolution influenced just by spherical aberration and diffraction. Graphs of the dependence of eccentricity, misorientation, ellipticity, and corrugation, which produces the resolution two times worse than the spherical aberration and diffraction, on the excitation of the lens for three different bore-to-gap ratios are included. The limiting eccentricity is around  $30\ \mu\text{m}$  and declines to  $1\ \mu\text{m}$  for higher excitation of the lens. The limiting orientation is around  $0.01\ \text{rad}$  and drops off for higher excitation of the lens even below  $1\ \text{mrad}$ . The restriction to the ellipticity is below  $0.1\ \mu\text{m}$  and slightly rises for higher excitation of the lens up to  $0.3\ \mu\text{m}$ . In conclusion, the correction of the parasitic aberrations caused by ellipticity using asymmetrical correcting devices or a stigmator is preferred to fine manufacturing, because the tolerances for ellipticity need to be very strict, therefore difficult to attain.

K. Amboss and J. C. E. Jennings [26] proved the Sturrock's perturbation theory experimentally. As the electron lens the winding air-cored solenoid was used and aberrations produced by small deformations of circular turns were investigated. Their apparatus consists of a tungsten electron source, the solenoid, two correctors, and a fluorescent screen. Axial astigmatism, coma, and anticoma were observed. The anticoma corresponds to the three-fold astigmatism.

J. Janse [19] investigated the deviation of the original paraxial trajectories due to the deviations from axial symmetry in electron lenses with the aid of perturbation theory. The Fourier series of the electrostatic potential is implemented into the Laplace equation which is solved using the method of successive overrelaxation. Several examples of frequently occurring asymmetries are mentioned. A changed electrode diameter and an axial shift of the cathode is approximated by an additional rotationally symmetric field, a shift of one of the electrodes and a tilted cathode is replaced by an additional dipole field, and an ellipticity of the electrode is alternated by an additional quadrupole field. A shift of the electrode in an einzel lens is discussed as a numerical example.

Eric Munro [20] introduced finite difference programs for computing tolerances for electrostatic lenses. The programs predict the beam displacement and coma, caused by misalignments and tilts, and the astigmatism, caused by ellipticities. The calculation is based on Bertein's principle of the equivalent perturbation of the boundary potential. The finite difference method is used to compute firstly the potential distribution of the unperturbed lens, secondly the perturbations effected by small changes in the position and shape of each electrode. The aberrations can be evaluated using aberration integrals. Three electrostatic lenses are studied as examples – a bipotential lens, an einzel lens, and a four-electrode lens for a focused ion beam system.

H. Liu and X. Zhu [21] discussed the numerical computation of the error effect in electron beam focusing and deflection systems using the perturbation theory and the finite element method. The important statement is that the assembling errors of deflectors and the elliptical errors of electrode or pole piece do not affect the first order optical properties and the first order chromatic aberrations. On the other hand, 42 additional aberration coefficients arise for the additional geometric aberrations for assembling errors. A magnetic focusing and deflection system is investigated as an illustrative example.

Christopher John Edgcombe [22] described a method for calculation of changes of paraxial trajectories in a given axisymmetric structure caused by both symmetric and asymmetric perturbations of the structure. Perturbations of electrodes include an axial displacement of an electrode, a change of diameter of an aperture, a displacement of an electrode transverse to the axis, and an ellipticity of an aperture. Effects of movement of parts of longitudinal sections, such as an axial displacement, a tilt, and a transverse shift of one part of a device to another, are also considered. Any of these perturbations, defined for a full circuit of the axis, can be expressed as a sum of Fourier components. Therefore, it is sufficient to establish the calculation for a general periodicity for the angular coordinate describing rotation round the axis. The perturbation potential is found using the new functional in the finite element method. Deviations of trajectories, computed separately from the unperturbed trajectory and directly from the perturbation potential, if possible, may be added linearly to the unperturbed trajectories. An electrostatic cathode lens is discussed as an example.

Lei Wei and Yin Hanchun [23] announced a method of prediction of the perturbation of particle trajectories caused by small displacement of electrodes. Unperturbed potential is calculated by the finite element method. Derivative of the potential with respect to the displacement vector is found from the variational principle, so the perturbed potential can be predicted. Variation of trajectory is found by solving the equation of motion for particles after the determination of perturbed potential. A bipotential lens is calculated to demonstrate this method.

Lei Wei and Tu Yan [24] proposed another method to determine the acceptable tolerance of manufacturing. The main idea is that the performance of electron optical system is usually determined by the electron trajectories. Hence acceptable tolerance can be obtained approximately by dividing the permissible perturbation of the trajectory in the image plane by the derivative of trajectory with respect to the vector of displacement of the perturbed electrode. Some typical perturbations of the main lens of cathode ray tube are analysed as an example. It is questionable if this method is enough accurate for purposes of electron microscopes design.

Ondřej Sháněl, Jakub Zlámal and Martin Oral [3] investigated compensation of parasitic aberrations of the saturated magnetic lens for a high resolution scanning transmission microscope. The setup consists of the objective lens, stigmators, and two deflectors. Two examples are discussed. The first example is the mechanical imperfection including an ellipticity of both pole pieces of  $0.25\ \mu\text{m}$ , a misalignment of the upper pole piece of  $0.25\ \mu\text{m}$ , and a tilt of upper pole piece of  $1\ \text{mrad}$ . The second example is the mechanical imperfection of  $0.5\ \mu\text{m}$  including the two times higher ellipticity and misalignment. The optimal excitation of the lens, the stigmators, and the deflector is calculated. The aberration coefficients are determined by ray tracing using the least squares fit of the aberration polynomial in the image plane. Further details can be found in the doctoral thesis by Ondřej Sháněl [2] as well.

Finally, some examples of papers related to other types of electron optical systems are listed below. The issue of multipoles is discussed in most cases. Paper by L. A. Baranova and F. H. Read from 2001 is covering aberrations caused by mechanical misalignments in an electrostatic quadrupole lens system [27]. Philip E. Batson in 2009 discussed parasitic aberrations in multipole optics, concretely finding of the optimal setup of a quadrupole-octupole third-order aberration corrector [28]. More complex paper written by G. W. Grime, F. Watt, G. D. Blower and J. Takacs from 1982 is dealing with real and parasitic aberrations of quadrupole probe-forming systems [29]. Aberrations of electrostatic systems with machining error are discussed in the paper by T. Tsumagari, J. Murakami,

H. Ohiwa and T. Noda from 1985 [30], where the extension of the perturbation theory for electrostatic lenses and deflectors is introduced. T. Ozaki, Y. H. Hisaoka and H. Murakami in the paper from 1993 [31] dealt with parasitic aberrations of an electrostatic deflector. Aberrations of microfabrication systems consisting of an electrostatic lens and an electrostatic deflector are introduced in the paper by Kenji Kurihara from 1990 [32]. Finally, the problems of parasitic aberrations in static sector field mass analyzers and their correction is covered by paper by M. I. Yavor and A. S. Berdnikov from 1993 [33].

# 3 Radial expansion of static electromagnetic fields

The field close to the optical axis can be interpolated from the axial potential. This is the most accurate interpolation method for solving the equation of motion of a particle close to the optical axis. For this reason, it is necessary to introduce radial expansion of axial fields, which is used for calculation of the axial multipole field functions from the 3D solution of the field in chapter 5 and for particle tracing in section 6.3.

Radial expansion of static electromagnetic fields can be easily derived from the Laplace equation. Exact definitions and derivations of most of used physical quantities, symbols, differential operators, and equations can be found in classical books of Electrodynamics by David J. Griffiths and Reed College [34] or by Jack Vanderlinde [35].

## 3.1 Electrostatic field

Scalar Laplace operator of an electrostatic potential in cylindrical coordinates is

$$\Delta\Phi = \frac{\partial^2\Phi}{\partial r^2} + \frac{1}{r}\frac{\partial\Phi}{\partial r} + \frac{1}{r^2}\frac{\partial^2\Phi}{\partial\varphi^2} + \frac{\partial^2\Phi}{\partial z^2}. \quad (3.1)$$

Let us assume that an electrostatic field is composed as a sum of a rotationally symmetric field and multipole fields with  $m$ -fold symmetry (namely rotationally symmetric for  $m = 0$ , dipole for  $m = 1$ , quadrupole for  $m = 2$ , hexapole for  $m = 3$ , etc.) as

$$\Phi(r, \varphi, z) = \sum_{m=0}^{\infty} \Phi_m(r, \varphi, z), \quad (3.2)$$

with

$$\Phi_m(r, \varphi, z) = F_m(r, z) \cos(m\varphi + \alpha_m), \quad (3.3)$$

where

$$F_m(r, z) = \sum_{n=0}^{\infty} f_{m,n}(z)r^n \quad (3.4)$$

and  $\alpha_m$  is the rotation of the  $m$ -th multipole field component. Then

$$\begin{aligned} \frac{\partial F_m}{\partial r} &= \sum_{n=0}^{\infty} n f_{m,n}(z) r^{n-1}, \\ \frac{\partial^2 F_m}{\partial r^2} &= \sum_{n=0}^{\infty} n(n-1) f_{m,n}(z) r^{n-2}, \\ \frac{\partial^2 F_m}{\partial z^2} &= \sum_{n=0}^{\infty} f''_{m,n}(z) r^n, \end{aligned} \quad (3.5)$$

with  $f''_{m,n}(z) \equiv \frac{\partial^2 f_{m,n}(z)}{\partial z^2}$ . Substituting (3.5) divided by  $r^m$  back to the Laplace equation (3.1) gives

$$\sum_{m=0}^{\infty} \sum_{n=0}^{\infty} [(n^2 - m^2) f_{m,n}(z) r^{n-m-2} + f''_{m,n}(z) r^{n-m}] \cos(m\varphi + \alpha_m) = 0. \quad (3.6)$$

Consequently, for every  $m$  must be satisfied

$$\begin{aligned} 0 = & -m^2 \frac{f_{m,0}(z)}{r^m} r^{-2} + (1 - m^2) \frac{f_{m,1}(z)}{r^m} r^{-1} + \\ & + \left[ (4 - m^2) \frac{f_{m,2}(z)}{r^m} + \frac{f''_{m,0}(z)}{r^m} (z) \right] r^0 + \dots + \\ & + \left[ (n^2 - m^2) \frac{f_{m,n}(z)}{r^m} + \frac{f_{m,n-2}(z)}{r^m} \right] r^{n-2} + \dots \end{aligned} \quad (3.7)$$

Equation (3.6), respectively (3.7), is fulfilled just when

$$f_{m,n}(z) = 0 \quad (3.8)$$

for every  $n < m$  and  $n > m$  with  $n$  of different parity than  $m$ . Let us define

$$\phi_m(z) \equiv \frac{f_{m,n}(z)}{r^m} \quad (3.9)$$

for every  $n = m$  with  $\phi_m$  as the  $m$ -th axial reduced potential, therefore

$$\frac{f_{m,n}(z)}{r^m} = \left( \prod_{j=m+2, m+4, \dots}^n \frac{-1}{j^2 - m^2} \right) \phi_m^{(n-m)}(z) \quad (3.10)$$

for every  $n > m$  with  $n$  of the same parity as  $m$ . Equation (3.10) can be rewritten as

$$\frac{f_{m,n}(z)}{r^m} = (-1)^i \frac{1}{4^i} \frac{m!}{i!(m+i)!} \phi_m^{(2i)}(z), \quad (3.11)$$

with  $2i = n - m$ .

According to (3.3), (3.4), and (3.11), equation (3.2) can be expressed as the power series

$$\Phi(r, \varphi, z) = \sum_{m=0}^{\infty} \sum_{i=0}^{\infty} (-1)^i \frac{1}{4^i} \frac{m!}{i!(m+i)!} \phi_m^{(2i)}(z) r^{2i+m} \cos(m\varphi + \alpha_m). \quad (3.12)$$

In the case of rotationally symmetric field, equation (3.12) transforms into the much more famous power series

$$\Phi_0(r, z) = \sum_{i=0}^{\infty} (-1)^i \frac{1}{4^i (i!)^2} \phi_0^{(2i)}(z) r^{2i}, \quad (3.13)$$

with  $\phi_0(z)$  as the axial potential. The same equation as (3.13) could be also found in the classical book of Electron optics by Peter W. Hawkes and Erwin Kasper [8] as equation (7.50) on page 85.

## 3.2 Magnetic field

In the case of magnetic field, a magnetic scalar potential is considered instead of the electrostatic potential. Equation (3.12) becomes

$$\Psi(r, \varphi, z) = \sum_{m=0}^{\infty} \sum_{i=0}^{\infty} (-1)^i \frac{1}{4^i} \frac{m!}{i!(m+i)!} \psi_m^{(2i)}(z) r^{2i+m} \cos(m\varphi + \alpha_m), \quad (3.14)$$

with  $\psi_m$  as the axial reduced magnetic potential. Similar equations as (3.14) can be found in the paper by Peter Andrew Sturrock [11] as equations (1.10) to (1.13) on page 394. The magnetic flux density in cylindrical coordinates is

$$\vec{B} = -\mu_0 \nabla \Psi = -\mu_0 \left( \frac{\partial \Psi}{\partial r}, \frac{1}{r} \frac{\partial \Psi}{\partial \varphi}, \frac{\partial \Psi}{\partial z} \right), \quad (3.15)$$

respectively

$$\begin{aligned} B_r &= -\mu_0 \sum_{m=0}^{\infty} \sum_{i=0}^{\infty} (-1)^i \frac{2i+m}{4^i} \frac{m!}{i!(m+i)!} \psi_m^{(2i)}(z) r^{2i+m-1} \cos(m\varphi + \alpha_m), \\ B_\varphi &= \mu_0 \sum_{m=0}^{\infty} \sum_{i=0}^{\infty} (-1)^i \frac{m}{4^i} \frac{m!}{i!(m+i)!} \psi_m^{(2i)}(z) r^{2i+m-1} \sin(m\varphi + \alpha_m), \\ B_z &= -\mu_0 \sum_{m=0}^{\infty} \sum_{i=0}^{\infty} (-1)^i \frac{1}{4^i} \frac{m!}{i!(m+i)!} \psi_m^{(2i+1)}(z) r^{2i+m} \cos(m\varphi + \alpha_m). \end{aligned} \quad (3.16)$$

At  $r = 0$ , which implies  $\varphi = 0$ , according to equations (3.16)

$$\begin{aligned} B_r &= -\mu_0 \psi_1, \\ B_\varphi &= 0, \\ B_z &= -\mu_0 \psi'_0. \end{aligned} \quad (3.17)$$

Let us define the axial multipole field function

$$D_m = -\mu_0 \psi_m. \quad (3.18)$$

Consequently, equations (3.16) transform into the power series

$$\begin{aligned} B_r &= \sum_{m=0}^{\infty} \sum_{i=0}^{\infty} (-1)^i \frac{2i+m}{4^i} \frac{m!}{i!(m+i)!} D_m^{(2i)}(z) r^{2i+m-1} \cos(m\varphi + \alpha_m), \\ B_\varphi &= -\sum_{m=0}^{\infty} \sum_{i=0}^{\infty} (-1)^i \frac{m}{4^i} \frac{m!}{i!(m+i)!} D_m^{(2i)}(z) r^{2i+m-1} \sin(m\varphi + \alpha_m), \\ B_z &= \sum_{m=0}^{\infty} \sum_{i=0}^{\infty} (-1)^i \frac{1}{4^i} \frac{m!}{i!(m+i)!} D_m^{(2i+1)}(z) r^{2i+m} \cos(m\varphi + \alpha_m). \end{aligned} \quad (3.19)$$

If the field is rotationally symmetric, it is useful to define the axial magnetic field

$$B_0 = D'_0 = -\mu_0 \psi'_0. \quad (3.20)$$

Therefore, equations (3.16) or (3.19) transform into the power series

$$\begin{aligned}
B_{r,0} &= \sum_{i=0}^{\infty} (-1)^{i+1} \frac{1}{(2i+2)4^i(i!)^2} B_0^{(2i+1)}(z) r^{2i+1}, \\
B_{\varphi,0} &= 0, \\
B_{z,0} &= \sum_{i=0}^{\infty} (-1)^i \frac{1}{4^i(i!)^2} B_0^{(2i)}(z) r^{2i}.
\end{aligned} \tag{3.21}$$

These power series (3.21) can be also derived via magnetic vector potential and vector Laplace equation. The same power series in slightly different form can be also found in the classical book of Electron optics by Peter W. Hawkes and Erwin Kasper [8] as equations (7.56a–c) on page 87.

In the case of the rotationally symmetric field, it is useful to know the power series for magnetic vector potential  $\vec{A} = (0, A_\varphi, 0)$  and magnetic flux  $\Phi_B$ . Especially if the software, like EOD [36], which solves the magnetic flux, is used. The power series for the magnetic vector potential is

$$A_\varphi(r, z) = \sum_{i=0}^{\infty} (-1)^i \frac{1}{(2i+2)4^i(i!)^2} B_0^{(2i)}(z) r^{2i+1}, \tag{3.22}$$

and the power series for magnetic flux is

$$\Phi_B(r, z) = \sum_{i=0}^{\infty} (-1)^i \frac{2\pi}{(2i+2)4^i(i!)^2} B_0^{(2i)}(z) r^{2i+2}. \tag{3.23}$$

# 4 Calculation of perturbed electron optical systems

This chapter summarizes two possible calculation strategies for computing field of the lens when the rotational symmetry is broken. The first method is calculation of the field in 2D. The perturbation theory is then used to calculate 2D parasitic fields arising due to broken rotational symmetry. The second method is the 3D computation of such systems. For this purpose, a list of software suitable for 3D calculations is included. A short comparison of 2D and 3D calculations is introduced in the final part of this chapter.

## 4.1 Perturbation theory

Let us start shortly with history. The perturbation theory was introduced by François Bertoin in 1948 for electrostatic lenses [10]. Unfortunately his work was published in French. Peter Andrew Sturrock in 1951 [11] applied this method to magnetic lenses. As the result the perturbation theory is in literature called after either Bertoin, or Sturrock.

It is necessary to consider, which order of the perturbation theory is used. Almost all authors are discussing only the first order perturbation theory, which substitutes the perturbation just by one parasitic field. Tsumagari and co-workers supposed also the higher order terms, but their analysis is confined to the first order terms [30]. On the contrary, Sturrock discussed also the higher order terms, therefore the perturbation can be replaced by more than one parasitic field [11].

The only problem of numerical determination of parasitic aberrations of perturbed systems is the computation of the field. The general first order perturbation theory is briefly introduced below. A rigorous calculation would proceed in these steps according to the chapter 31.3 in Principles of Electron optics by Peter W. Hawkes and Erwin Kasper [8] on pages 475–477:

1. The field of the perfect unperturbed system is computed in a standard way as a boundary-value problem in 2D cylindrical coordinates.
2. From the solution, the boundary values of the electric and magnetic intensity ( $\vec{E}$  and  $\vec{H}$ ) are determined.
3. Surface deformation  $\vec{s}$  is determined from ellipticities, misalignments, tilts, and other deformations, defined as the shift from a point at the ideal surface to the corresponding point at the real surface. If  $|\vec{s}|$  is small enough, the deformation  $\vec{s}$  corresponds to the parasitic potential on the ideal boundary of  $\delta\Phi = \vec{E} \cdot \vec{s}$ , respectively  $\delta\Psi = \vec{H} \cdot \vec{s}$ .
4. With these new boundary values  $\delta\Phi$ , respectively  $\delta\Psi$ , the boundary-value problem in the ideal (or undeformed) domain is solved and the parasitic potential is added

to the results of unperturbed system.

5. The total fields are known so particles can be traced or aberration integrals can be evaluated.

Any perturbation, which is defined for a full circuit of the axis, can be expressed as a sum of Fourier components [10, 22]. For further use in the following chapters, it is useful to discuss the perturbation theory for basic perturbations more precisely. Three main mechanical defects breaking rotational symmetry of electron optical system are covered by this theory — ellipticity, misalignment and tilt, using nomenclature as in [3] or [20], respectively elliptic distortion, eccentricity and orientation, using nomenclature by Sturrock [11].

Reflecting the first order perturbation theory, perturbations can be classified according to the periodicity  $m$  for the angular coordinate  $\varphi$ , describing rotation round the axis  $z$ , as [22]:

- $m = 0$  (no variation round the axis):
  - axial shift of an electrode, a pole piece, or a section
  - change in diameter of an electrode or a pole piece
- $m = 1$  (single cycle round the axis, one-fold symmetry):
  - tilt of an electrode, a pole piece, or a section
  - misalignment (transverse shift) of an electrode, a pole piece, or a section
- $m = 2$  (two cycles round the axis, two-fold symmetry):
  - ellipticity of an electrode or pole piece

According to the first order perturbation theory a perturbation of pole pieces causes the parasitic magnetic field, characterized by the multipole magnetic scalar potential, which fulfil the boundary condition  $\Psi_m$  on pole pieces and equals to zero on the axis of symmetry, unperturbed surfaces, and outer boundaries of computed region. In the case of an ellipticity, the quadrupole parasitic field characterized by

$$\Psi_2 = -H_r e \cos(2\varphi + \alpha) \quad (4.1)$$

appears. In the case of a misalignment, the dipole parasitic field characterized by

$$\Psi_1 = -H_r a \cos(\varphi + \alpha) \quad (4.2)$$

rises up, and, finally, a tilt of pole pieces causes also the dipole parasitic field characterized by

$$\Psi_1 = [rH_z - (z - z_t)H_r]t \cos(\varphi + \alpha), \quad (4.3)$$

with  $\vec{H} = (H_r, 0, H_z)$  as the magnetic field intensity of unperturbed lens and  $e$ ,  $a$ ,  $t$ ,  $z_t$ , and  $\alpha$  as parameters characterizing the perturbations (see figure 4.1) [3, 11]. In the case of an electrostatic lens, simply substitute  $\Psi_1$ ,  $\Psi_2$  by  $\Phi_1$ ,  $\Phi_2$  and  $\vec{H} = (H_r, 0, H_z)$  by  $\vec{E} = (E_r, 0, E_z)$  [8, 20].

This theory requires the field intensity to be perpendicular to the perturbed surface. Unfortunately this is fulfilled only for electrostatic and non-saturated magnetic lenses.

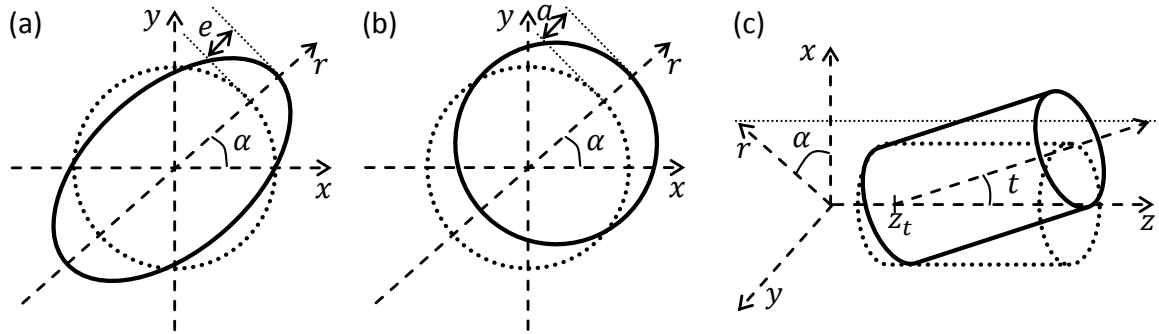


**Figure 4.1:** Three types of mechanical imperfections — (a) ellipticity, (b) misalignment, and (c) tilt, using nomenclature as in [3, 20], respectively (a) elliptic distortion, (b) eccentricity, and (c) orientation, using nomenclature by Sturrock [11]. Dotted lines show ideal unperturbed lenses, solid lines the perturbed lenses.

The magnetic field intensity in saturated magnetic lenses does not have to be perpendicular to the perturbed surface of pole pieces. Despite this the first order perturbation theory is a powerful method for calculation of imperfect lenses, which is implemented, for instance, in software EOD in module Tolerancing [12].

Reflecting the perturbation theory including the higher order terms, perturbations are substituted as [11]:

- ellipticity – additional quadrupole field,
- misalignment and tilt – additional dipole and quadrupole field.

The only difference to the standard first order perturbation theory is the additional quadrupole field in the case of a misalignment or a tilt. However, the additional quadrupole field is weaker than the additional quadrupole field caused by an ellipticity of similar magnitude. Also it is very unlikely that the real optical element would suffer, due to mechanical imperfections during manufacturing, just from one perturbation. Therefore, the standard first order perturbation theory seemed to be sufficient, if a combination of basic perturbations of similar magnitudes is considered.

## 4.2 Computation of perturbed systems in 3D

If the previously discussed technique cannot be used, the field must be solved as fully 3D problem. This is necessary, for example, in the case of a magnetic lens with a hole in the pole piece [4]. The 3D solution of the field can be computed in software like CPO3D and CPO3DS [37], SIMION [38], COMSOL Multiphysics [13] with AC/DC module, Field Precision [39], program LORENTZ by INTEGRATED Engineering Software [40], 3D software package by Munro’s Electron Beam Software Ltd. [41], and some others.

A brief description and illustration of suite of programs written for the computer-aided design of three-dimensional electron optical systems is in the chapter by John A. Rouse [17] and in the paper by John A. Rouse and Eric Munro [42]. The programs are based on the finite difference methods for calculation of the potentials at points on a 3D rectangular grid and can be used for analysis of electrostatic and magnetic systems.

There are some disadvantages of using 3D software. The powerful computer with enough memory is necessary, and the computational time can be rather long. The most important question is the accuracy of results, because the mesh cannot be usually as dense as in the 2D calculation. This is illustrated in the following section.

### 4.3 Short note comparing 2D and 3D computation

It is useful to illustrate the main differences between 2D and 3D computation on an example. The example is the magnetic objective lens of K. Tsuno [43] (figure 4.2). The magnetic lens is saturated, and the excitation of the lens is 10500 A-turns, which corresponds to the performance in a 200 kV high resolution scanning transmission electron microscope [3]. Comparison of the computation in 2D using EOD software and 3D using COMSOL Multiphysics is summed up in the table 4.1. It must be noticed that only one half of the lens is calculated in 3D. Despite that COMSOL allows using a mirror symmetry to get the whole 3D field, the particle tracing in such mirrored field is not possible. The difference in computational time and memory requirements is dramatic. This is the reason, why 2D calculation methods, including the perturbation theory, are important.

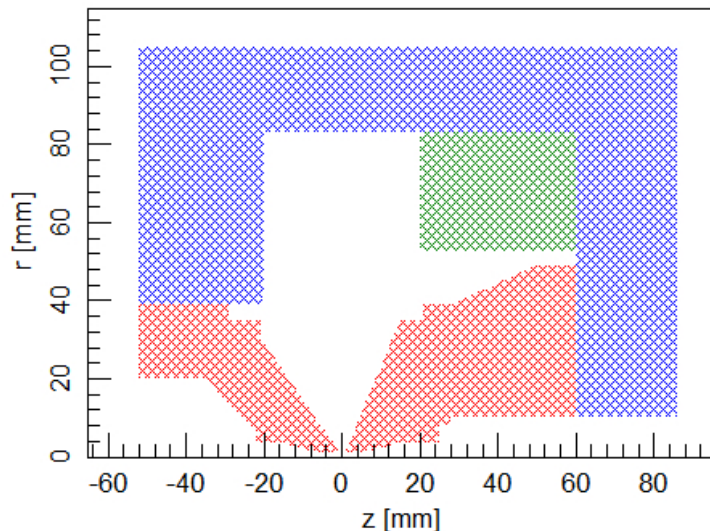


**Figure 4.2:** 200 kV magnetic objective lens – pole pieces (red), yoke (blue), coil (green). Bore diameter and gap are both 2 mm.

**Table 4.1:** Comparison of the computation in 2D and 3D.

	2D computation	3D computation
Performed in	EOD [36]	COMSOL [13]
Calculation algorithm of the field	1 <sup>st</sup> order finite element method	2 <sup>nd</sup> order finite element method
Smallest mesh element	0.05 mm	0.084 mm
Number of mesh elements	~ 0.5 million	~ 4.5 million
Relative accuracy	$1 \cdot 10^{-14}$	$5 \cdot 10^{-8}$
Computational time	1 minute	13 hours
Memory requirements for computation	100 MB	65 GB (half of the lens)
Memory requirements to display results	30 MB	6 GB

# 5 Calculation of axial multipole field functions from the 3D solution of the field

Particle tracing in the 3D fields is difficult due to problems with field interpolation. Electrons are typically moving in distances about  $100\ \mu\text{m}$  from the optical axis. It means, that the only one or two mesh elements near to the axis are used for interpolation of the field. Every small error, whether numerical or generated by inappropriate element shape, of calculated field in mesh nodes can have great influence on particle trajectory. In addition, the interpolation polynomial, usually of second or third order, cannot correctly express the field dependence on distance from the optical axis. A method to interpolate the field close to the axis using radial expansion of the axial field was introduced in section 3.2. Knowledge of axial fields is important for aberration theory, which requires derivatives of the axial field of high orders. Therefore, it is important to find a suitable method to calculate the axial multipole field functions from the 3D solution of the field.

Three different algorithms for the calculation of axial multipole field functions from the 3D solution are introduced. The first one is based on the Fourier series expansion, and the axial multipole field functions are evaluated at series of points on the optical axis. The Fourier expansion is introduced, for example, in the book *Magnetic Electron Lenses* edited by Peter W. Hawkes [15] in the section 2.1.2 on page 60. The second algorithm is based on the least square fit of the wavelets (sum of Gaussian functions), and the axial multipole field functions are determined in all positions along the optical axis. The wavelet interpolation is one of the method studied by Tomáš Radlička and Bohumila Lencová [44]. The third method combines the best parts of the previous ones.

All scripts evaluating the axial multipole functions are written in MATLAB [45]. The methods are discussed for magnetic fields, because magnetic lenses are more common in standard electron microscopes than electrostatic ones.

## 5.1 Algorithm based on the Fourier series expansion

This method was briefly introduced and used in [4]. The calculation process consists of three main steps repeated  $Z$ -times for all selected  $z$  coordinates  $z_1 < z_2 < \dots < z_Z$  along the axis. In the first step, components of the magnetic flux density (in cylindrical coordinates) are evaluated using built in interpolation methods of 3D software in points on  $R$  circles with increasing radius  $r_1 < r_2 < \dots < r_R$ , but the same  $z$  position of their centres on the optical axis (see figure 5.1).

In the second step, the magnetic field components on each circle are expanded into

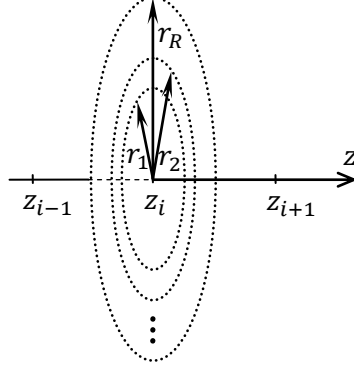


**Figure 5.1:** Components of the field are evaluated in points on  $R$  concentric circles.

the cosine, respectively the sine, Fourier series reflecting equations (3.19) as

$$\begin{aligned}
 B_r(r, \varphi, z) &\approx C_{r,0}(r, z) + \sum_{m=1}^M C_{r,m}(r, z) \cos(m\varphi + \alpha_m), \\
 B_\varphi(r, \varphi, z) &\approx \sum_{m=1}^M C_{\varphi,m}(r, z) \sin(m\varphi + \alpha_m), \\
 B_z(r, \varphi, z) &\approx C_{z,0}(r, z) + \sum_{m=1}^M C_{z,m}(r, z) \cos(m\varphi + \alpha_m),
 \end{aligned} \tag{5.1}$$

with  $\alpha_m$  as the rotation of  $m$ -th multipole field component.

If the rotation of the multipole field is known, for example, from the geometry of the lens, the Fourier coefficients are calculated as

$$\begin{aligned}
 C_{r,0}(r, z) &= \frac{1}{2\pi} \int_0^{2\pi} B_r(r, \varphi, z) d\varphi, \\
 C_{r,m}(r, z) &= \frac{1}{\pi} \int_0^{2\pi} B_r(r, \varphi, z) \cos(m\varphi + \alpha_m) d\varphi, \\
 C_{\varphi,m}(r, z) &= \frac{1}{\pi} \int_0^{2\pi} B_\varphi(r, \varphi, z) \sin(m\varphi + \alpha_m) d\varphi, \\
 C_{z,0}(r, z) &= \frac{1}{2\pi} \int_0^{2\pi} B_z(r, \varphi, z) d\varphi, \\
 C_{z,m}(r, z) &= \frac{1}{\pi} \int_0^{2\pi} B_z(r, \varphi, z) \cos(m\varphi + \alpha_m) d\varphi.
 \end{aligned} \tag{5.2}$$

The evaluation of the Fourier coefficients as integrals over angular coordinate  $\varphi$  for each circle also partially eliminates the fluctuation of the field due to numerical errors of the 3D field calculation in azimuthal direction.

With respect to equations (3.19), the Fourier coefficients are proportional to

$$\begin{aligned}
C_{r,0}(r, z) &\propto \sum_{i=0}^{N-1} B_0^{(2i+1)}(z)r^{2i+1}, \\
C_{r,m}(r, z) &\propto \sum_{i=0}^{N-1} D_m^{(2i)}(z)r^{2i+m-1}, \\
C_{\varphi,m}(r, z) &\propto \sum_{i=0}^{N-1} D_m^{(2i)}(z)r^{2i+m}, \\
C_{z,0}(r, z) &\propto \sum_{i=0}^{N-1} B_0^{(2i)}(z)r^{2i}, \\
C_{z,m}(r, z) &\propto \sum_{i=0}^{N-1} D_m^{(2i+1)}(z)r^{2i+m}.
\end{aligned} \tag{5.3}$$

In the third step, the axial multipole field functions at the given  $z$  coordinate are determined from the known multipole field components and their dependence on radial coordinate  $r$  by the least squares fit with respect to the equations (5.3). Usually only the first three terms of series are used, therefore  $N = 3$ , which means, the axial multipole field functions and their first five derivatives are computed. This least square fit eliminates the fluctuations of the 3D field interpolation in radial direction. Standard deviations  $SD(D_m)$  of fitted axial field functions  $D_m(z)$  are used as an index of quality of the least squares fit.

The least squares fit can be written in the matrix notation as [46]

$$\mathbf{A} = (\mathbf{M}' \cdot \mathbf{M}) \setminus \mathbf{M}' \cdot \mathbf{F}, \tag{5.4}$$

with  $\mathbf{A}$  as the vector of length  $2N = 6$  including the axial multipole field function  $D_m(z)$  with its derivatives,  $\mathbf{M}$  as the matrix of size  $2N \times 3R$  including coefficients from equations (5.3), and  $\mathbf{F}$  as the vector of length  $3R$  consisting of the Fourier coefficients  $C_{r,m}(r, z)$ ,  $C_{\varphi,m}(r, z)$ , and  $C_{z,m}(r, z)$ . For further details see equations (A.1) and (A.2) in appendix A.1 on page 64. The least squares fit is provided separately for every multipole component and for every  $z$  position along the axis.

The vector  $\mathbf{S}$  of the standard deviations  $SD(D_m)$  is calculated as

$$\mathbf{S} = \sqrt{\frac{(\mathbf{M} \cdot \mathbf{A} - \mathbf{F}') \cdot (\mathbf{M} \cdot \mathbf{A} - \mathbf{F}')}{3R - 2N}} \sqrt{\text{diag}(\text{inv}(\mathbf{M}' \cdot \mathbf{M}))}. \tag{5.5}$$

The axial multipole field functions and their first five derivatives (due to  $N = 3$ ) are known in all given  $z$  positions along the axis. The field needs to be interpolated between the given  $z$  positions, for example, using splines. Unfortunately, this method does not include any smoothing of the axial multipole field functions in the  $z$  direction, therefore, the interpolation may become unstable, due to the fluctuations of the axial multipole field functions. Consequently, the interpolated axial multipole field functions and their derivatives can be affected by a high degree of noise, which is the main disadvantage of this algorithm.

## 5.2 Algorithm based on the wavelet interpolation

The second method is much more compact and consists of just one step, because the axial field function is determined as a sum of Gaussian functions (wavelet). The Gaussian wavelet interpolation was introduced by Martin Berz [47] and is implemented, for example, in COSY INFINITY [48]. This interpolation method was used for electrostatic lenses, for instance, by Zhixiong Liu [49] and discussed as one of the interpolation method by Tomáš Radlička and Bohumila Lencová [44].

Let us assume the axial multipole field functions in the form of Gaussian wavelets. The base Gaussian functions have centres in  $J$  points  $z_j$  on the  $z$  axis. In the case of rotationally symmetric field

$$B_0 = \sum_{j=1}^J A_{0,j} \exp \left[ -\frac{(z - z_j)^2}{(\sigma d_z)^2} \right] \quad (5.6)$$

and in the case of multipole field

$$D_m = \sum_{j=1}^J A_{m,j} \exp \left[ -\frac{(z - z_j)^2}{(\sigma d_z)^2} \right], \quad (5.7)$$

where  $A_{m,j}$  are unknown parameters,  $\sigma$  is the parameter determining the width of the base Gaussian function, and  $d_z = z_{j+1} - z_j$  is the constant distance between two nearby node points.

Substituting (5.6) to (3.21) for the rotationally symmetric field and (5.7) to (3.19) for the multipole fields using the first  $N$  terms of the series

$$\begin{aligned} B_r(r, \varphi, z) &\approx \sum_{j=1}^J \sum_{i=0}^{N-1} (-1)^{i+1} \frac{1}{(2i+2)4^i(i!)^2} \frac{d^{2i+1}}{dz^{2i+1}} \left\{ \exp \left[ -\frac{(z - z_j)^2}{(\sigma d_z)^2} \right] \right\} r^{2i+1} A_{0,j} \\ &\quad + \sum_{m=1}^M \sum_{j=1}^J \sum_{i=0}^{N-1} (-1)^i \frac{2i+m}{4^i} \frac{m!}{i!(m+i)!} \frac{d^{2i}}{dz^{2i}} \left\{ \exp \left[ -\frac{(z - z_j)^2}{(\sigma d_z)^2} \right] \right\} \\ &\quad r^{2i+m-1} \cos(m\varphi + \alpha_m) A_{m,j} = \sum_{j=1}^J K_{r,0,j,N} A_{0,j} + \sum_{m=1}^M \sum_{j=1}^J K_{r,m,j,N} A_{m,j}, \\ B_\varphi(r, \varphi, z) &\approx - \sum_{m=1}^M \sum_{j=1}^J \sum_{i=0}^{N-1} (-1)^i \frac{m}{4^i} \frac{m!}{i!(m+i)!} \frac{d^{2i}}{dz^{2i}} \left\{ \exp \left[ -\frac{(z - z_j)^2}{(\sigma d_z)^2} \right] \right\} r^{2i+m-1} \\ &\quad \sin(m\varphi + \alpha_m) A_{m,j} = \sum_{m=1}^M \sum_{j=1}^J K_{\varphi,m,j,N} A_{m,j}, \\ B_z(r, \varphi, z) &\approx \sum_{j=1}^J \sum_{i=0}^{N-1} (-1)^i \frac{1}{4^i(i!)^2} \frac{d^{2i}}{dz^{2i}} \left\{ \exp \left[ -\frac{(z - z_j)^2}{(\sigma d_z)^2} \right] \right\} r^{2i} A_{0,j} \\ &\quad + \sum_{m=1}^M \sum_{j=1}^J \sum_{i=0}^{N-1} (-1)^i \frac{1}{4^i} \frac{m!}{i!(m+i)!} \frac{d^{2i+1}}{dz^{2i+1}} \left\{ \exp \left[ -\frac{(z - z_j)^2}{(\sigma d_z)^2} \right] \right\} r^{2i+m} \\ &\quad \cos(m\varphi + \alpha_m) A_{m,j} = \sum_{j=1}^J K_{z,0,j,N} A_{0,j} + \sum_{m=1}^M \sum_{j=1}^J K_{z,m,j,N} A_{m,j}, \end{aligned} \quad (5.8)$$

with  $\alpha_m$  as the rotation of  $m$ -th multipole field component. If this rotation is known, for instance, from the geometry of the lens, the only unknown parameters are just  $A_{m,j}$ .

Let us assume, that the magnetic flux density components  $B_r(\vec{r}_p)$ ,  $B_\varphi(\vec{r}_p)$  and  $B_z(\vec{r}_p)$  are known in  $P$  points  $\vec{r}_1, \vec{r}_2, \dots, \vec{r}_P$ . These points can be, for example, the nodal points of the 3D mesh in the area of interest – if the mesh is sufficiently dense. Consequently, the unknown parameters  $A_{m,j}$  can be calculated using the least squares fit. In the matrix notation

$$\mathbf{A} = (\mathbf{M}' \cdot \mathbf{M}) \setminus \mathbf{M}' \cdot \mathbf{F}, \quad (5.9)$$

with  $\mathbf{A}$  as the vector of length  $J \cdot M$  including the unknown parameters  $A_{m,j}$ ,  $\mathbf{M}$  as the matrix of size  $3P \times J \cdot M$  including the coefficients  $K_{r,m,j,N}$ ,  $K_{\varphi,m,j,M}$ , and  $K_{z,m,j,N}$  from equations (5.8), and  $\mathbf{F}$  as the vector of length  $3P$  consisting of the field components  $B_r(\vec{r}_p)$ ,  $B_\varphi(\vec{r}_p)$ , and  $B_z(\vec{r}_p)$ . For further details see equations (A.3) in appendix A.1 on page 65. The least squares fit is provided just once. The problematic part is the computation with two large matrices  $\mathbf{M}$  and  $\mathbf{M}'$ .

The vector  $\mathbf{S}$  of the standard deviations  $SD(A_{m,j})$  is calculated as

$$\mathbf{S} = \sqrt{\frac{(\mathbf{M} \cdot \mathbf{A} - \mathbf{F}') \cdot (\mathbf{M} \cdot \mathbf{A} - \mathbf{F}')}{3P - J \cdot M}} \sqrt{\text{diag}(\text{inv}(\mathbf{M}' \cdot \mathbf{M}))}. \quad (5.10)$$

Finally, the axial field  $B_0$  and the axial multipole field functions  $D_m$  are evaluated according to equations (5.6) and (5.7). Any of their derivative can be computed as

$$\frac{d^n B_0}{dz^n} = \sum_{j=1}^J A_{0,j} \frac{d^n}{dz^n} \left\{ \exp \left[ -\frac{(z - z_j)^2}{(\sigma d_z)^2} \right] \right\} \quad (5.11)$$

in the case of axial field, respectively

$$\frac{d^n D_m}{dz^n} = \sum_{j=1}^J A_{m,j} \frac{d^n}{dz^n} \left\{ \exp \left[ -\frac{(z - z_j)^2}{(\sigma d_z)^2} \right] \right\} \quad (5.12)$$

in the case of axial multipole field functions.

The standard deviations of the axial field  $B_0$  and axial multipole field functions  $D_m$  can be calculated as

$$SD(B_0(z)) = \sqrt{\sum_{j=1}^J \left\{ SD(A_{0,j}(z)) \exp \left[ -\frac{(z - z_j)^2}{(\sigma d_z)^2} \right] \right\}^2} \quad (5.13)$$

in the case of axial field, respectively

$$SD(D_m(z)) = \sqrt{\sum_{j=1}^J \left\{ SD(A_{m,j}(z)) \exp \left[ -\frac{(z - z_j)^2}{(\sigma d_z)^2} \right] \right\}^2} \quad (5.14)$$

in the case of axial multipole field functions. The standard deviations of their derivatives can be determined analogously.

To summarize, the axial multipole field functions and any of their derivatives are known in all  $z$  coordinates along the axis. The axial multipole field functions and their derivatives are smooth, which is necessary for accurate ray tracing and for evaluation of aberration integrals. This is the main advantage of this method. The only problem

can appear when the 3D calculated field suffers from a high degree of noise in azimuthal direction. This could cause an inaccuracy in the decomposition into the multipole components because this method is less stable than the calculation of Fourier coefficients as integrals. Unfortunately this algorithm needs working with two large matrices, so the memory consumption is significant. Due to this it is necessary to use a computer with enough memory. This is the only disadvantage of this method. Nevertheless, the computation of the 3D field requires a powerful computer as well so this problem should be in reality marginal.

### 5.3 Wavelet interpolation of radial dependence of Fourier components

The third method combines the main advantages of previous ones. The calculation process consists of three main steps. The first two steps are the same as in the first discussed method. Components of the field are evaluated using built in interpolation methods of 3D software in points on  $L$  circles with the radii  $r_1, r_2, \dots, r_L$  and the positions of centres  $z_1, z_2, \dots, z_L$  in the whole area of interest. The circles can be, for instance, the same as in the first method, which implies  $L = R \cdot Z$ . Afterwards the magnetic field components on each circle are expanded into the cosine, respectively the sine, Fourier series in the same way as in (5.1) and (5.2).

Calculated Fourier coefficients are used instead of the field components for the second method. Equations (5.8) change to

$$\begin{aligned}
C_{r,0}(r, z) &\approx \sum_{j=1}^J \sum_{i=0}^{N-1} (-1)^{i+1} \frac{1}{(2i+2)4^i(i!)^2} \frac{d^{2i+1}}{dz^{2i+1}} \left\{ \exp \left[ -\frac{(z-z_j)^2}{(\sigma d_z)^2} \right] \right\} r^{2i+1} A_{0,j} \\
&= \sum_{j=1}^J K_{r,0,j,N} A_{0,j}, \\
C_{r,m}(r, z) &\approx \sum_{j=1}^J \sum_{i=0}^{N-1} (-1)^i \frac{2i+m}{4^i} \frac{m!}{i!(m+i)!} \frac{d^{2i}}{dz^{2i}} \left\{ \exp \left[ -\frac{(z-z_j)^2}{(\sigma d_z)^2} \right] \right\} r^{2i+m-1} A_{m,j} \\
&= \sum_{j=1}^J K_{r,m,j,N} A_{m,j}, \\
C_{\varphi,m}(r, z) &\approx - \sum_{j=1}^J \sum_{i=0}^{N-1} (-1)^i \frac{m}{4^i} \frac{m!}{i!(m+i)!} \frac{d^{2i}}{dz^{2i}} \left\{ \exp \left[ -\frac{(z-z_j)^2}{(\sigma d_z)^2} \right] \right\} r^{2i+m-1} A_{m,j} \\
&= \sum_{j=1}^J K_{\varphi,m,j,N} A_{m,j}, \\
C_{z,0}(r, z) &\approx \sum_{j=1}^J \sum_{i=0}^{N-1} (-1)^i \frac{1}{4^i(i!)^2} \frac{d^{2i}}{dz^{2i}} \left\{ \exp \left[ -\frac{(z-z_j)^2}{(\sigma d_z)^2} \right] \right\} r^{2i} A_{0,j} \\
&= \sum_{j=1}^J K_{z,0,j,N} A_{0,j},
\end{aligned} \tag{5.15}$$

$$\begin{aligned}
C_{z,m}(r, z) &\approx \sum_{j=1}^J \sum_{i=0}^{N-1} (-1)^i \frac{1}{4^i} \frac{m!}{i!(m+i)!} \frac{d^{2i+1}}{dz^{2i+1}} \left\{ \exp \left[ -\frac{(z-z_j)^2}{(\sigma d_z)^2} \right] \right\} r^{2i+m} A_{m,j} \\
&= \sum_{j=1}^J K_{z,m,j,N} A_{m,j}.
\end{aligned}$$

The only unknown parameters  $A_{m,j}$  are calculated by the least squares fit, which is provided separately for the rotationally symmetric and every multipole component. In the matrix notation

$$\mathbf{A} = (\mathbf{M}' \cdot \mathbf{M}) \setminus \mathbf{M}' \cdot \mathbf{F}, \quad (5.16)$$

with  $\mathbf{A}$  as the vector of length  $J$  including the unknown parameters  $A_{m,j}$ ,  $\mathbf{M}$  as the matrix of size  $3L \times J$  including the coefficients  $K_{r,m,j,N}$ ,  $K_{\varphi,m,j,N}$ , and  $K_{z,m,j,N}$  from equations (5.15), and  $\mathbf{F}$  as the vector of length  $3L$  consisting of the Fourier coefficients  $C_{r,m}(\vec{r})$ ,  $C_{\varphi,m}(\vec{r})$ , and  $C_{z,m}(\vec{r})$ . For further details see equations (A.4) in appendix A.1 on page 65. The least squares fit is calculated  $(M+1)$ -times.

The vector  $\mathbf{S}$  of the standard deviations  $SD(A_{m,j})$  is calculated as

$$\mathbf{S} = \sqrt{\frac{(\mathbf{M} \cdot \mathbf{A} - \mathbf{F}') \cdot (\mathbf{M} \cdot \mathbf{A} - \mathbf{F}')}{3L - J}} \sqrt{\text{diag}(\text{inv}(\mathbf{M}' \cdot \mathbf{M}))}. \quad (5.17)$$

Finally, the axial field  $B_0$  and the axial multipole field functions  $D_m$  are evaluated according to equations (5.6) and (5.7). Their standard deviations are calculated using (5.13) and (5.14). Any of their derivatives are computed via (5.11) and (5.12).

The axial multipole field functions and any of their derivatives are known in all  $z$  coordinates after applying this algorithm. The axial multipole field functions and their derivatives are smooth, which is necessary for accurate ray tracing, for evaluation of aberration integrals, or for computing aberration coefficients using differential algebra [49]. This method seems to be the most powerful, thanks to applying the best parts of previously described algorithms.

## 5.4 Magnetic lens with a hole in the pole piece

To compare three presented algorithms and examine their advantages and disadvantages, the magnetic objective lens of K. Tsuno [43] with a hole drilled into the pole piece perpendicular to the optical axis, discussed in [4], is studied. The position of the hole is  $z = -10$  mm and the diameter is 5 mm (figure 5.2). The hole drilled into the pole piece of the lens causes a change of rotationally symmetric axial field and rises additional multipole fields – dipole field, weak quadrupole field, and even more weaker hexapole field [4]. The magnetic lens is saturated, and the excitation of the lens is 10 500 A-turns, which corresponds to the performance in a 200 kV high resolution scanning transmission electron microscope [3].

The smallest mesh element size, used for the 3D calculation (performed in COMSOL Multiphysics [13]), was reduced to 0.12 mm in the gap region from  $z = -2$  mm to  $z = 2$  mm and in the surrounding regions close to the axis the mesh size was rising up to 0.2 mm to achieve sufficient accuracy of the field, reasonable memory consumption (70 GB), and computation time. Second order finite element method was used to calculate the field. The smallest possible relative accuracy of the field computation  $5 \cdot 10^{-8}$ , for which the solution still converges, was used. Components of the magnetic flux density were evaluated

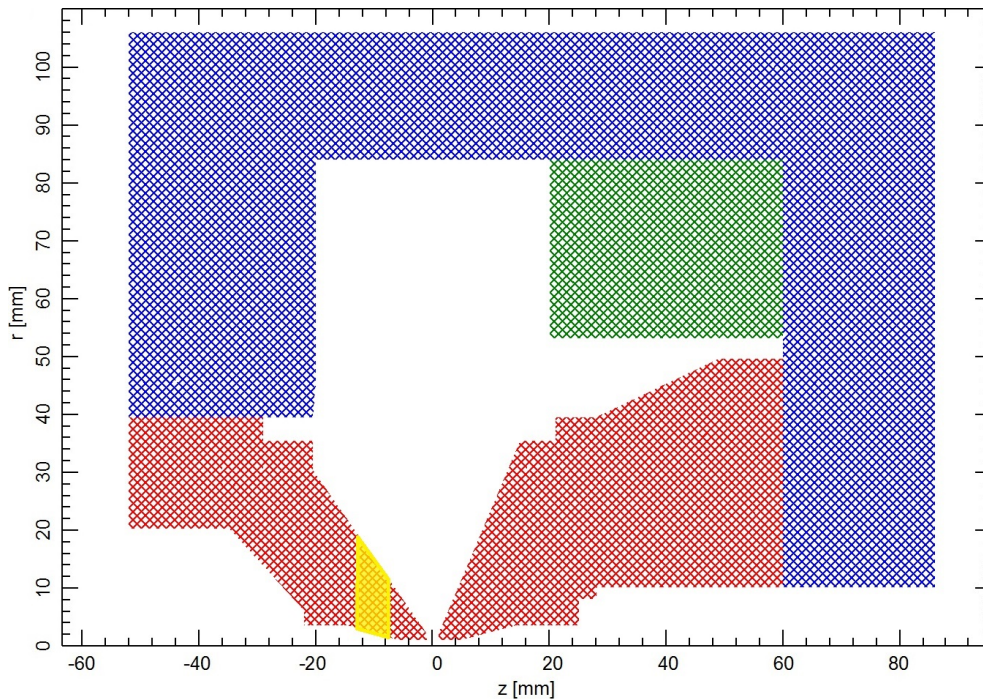


**Figure 5.2:** Magnetic lens with the hole drilled perpendicular to the optical axis – hole (yellow), pole pieces (red), yoke (blue), coil (green).

using built in interpolation methods of COMSOL Multiphysics in 360 points on  $R = 50$  circles with radii from 0.01 mm to 0.50 mm. The sampling step in axial direction was 0.01 mm. The area of interest was from  $z = -20$  mm to  $z = 10$  mm, which implies  $Z = 301$   $z$  positions of circles, respectively  $L = 15\,050$  circles in total. The components of the magnetic flux density in  $P = 19\,283$  nodal points of the 3D mesh in the area of interest were exported to MATLAB as well. Finally, the axial field functions of the lens with the hole in the pole piece were determined by three discussed algorithms. Memory requirements of all three algorithms are between 1 and 2 GB, therefore the axial multipole field functions were calculated on a standard personal computer and the calculation lasted between 10 and 30 minutes.

Using the algorithm based on Fourier series expansion, the axial multipole functions are calculated in the series of 301 points along the axis (figure 5.3, green points). Especially the hexapole component suffers from a relatively high degree of noise. Consequently, it is necessary to apply some de-noising process before further use of the axial field functions.

Applying the algorithm based on wavelet interpolation, the continuous axial multipole functions are evaluated (figure 5.3, red solid lines). Parameters of the least squares fit were optimized to get the functions with the lowest level of noise, which is fulfilled for  $N = 4$ ,  $d_z = 0.2$  mm, and  $\sigma = 2.2$  chosen according to results of [44]. However, the multipole field functions suffer from the parasitic peaks in the gap region. This inaccuracy can be affected by too large mesh elements in the gap region. Unfortunately, computation with mesh with smaller mesh step in the gap could not be performed due to available memory restriction.

Employing the wavelet interpolation of radial dependence of Fourier components, the smooth continuous axial multipole functions are determined (figure 5.3, black dashed lines). This algorithm evidently provides the best results. Parameters of the least square fit are optimized to obtain the higher derivatives of the functions with the lowest level of noise. The optimal values seemed to be  $N = 4$ ,  $\sigma = 2.2$ , and  $d_z = 0.4$  mm. The first three

derivatives of the axial field functions are shown in figure 5.4 to illustrate the capabilities of this method.

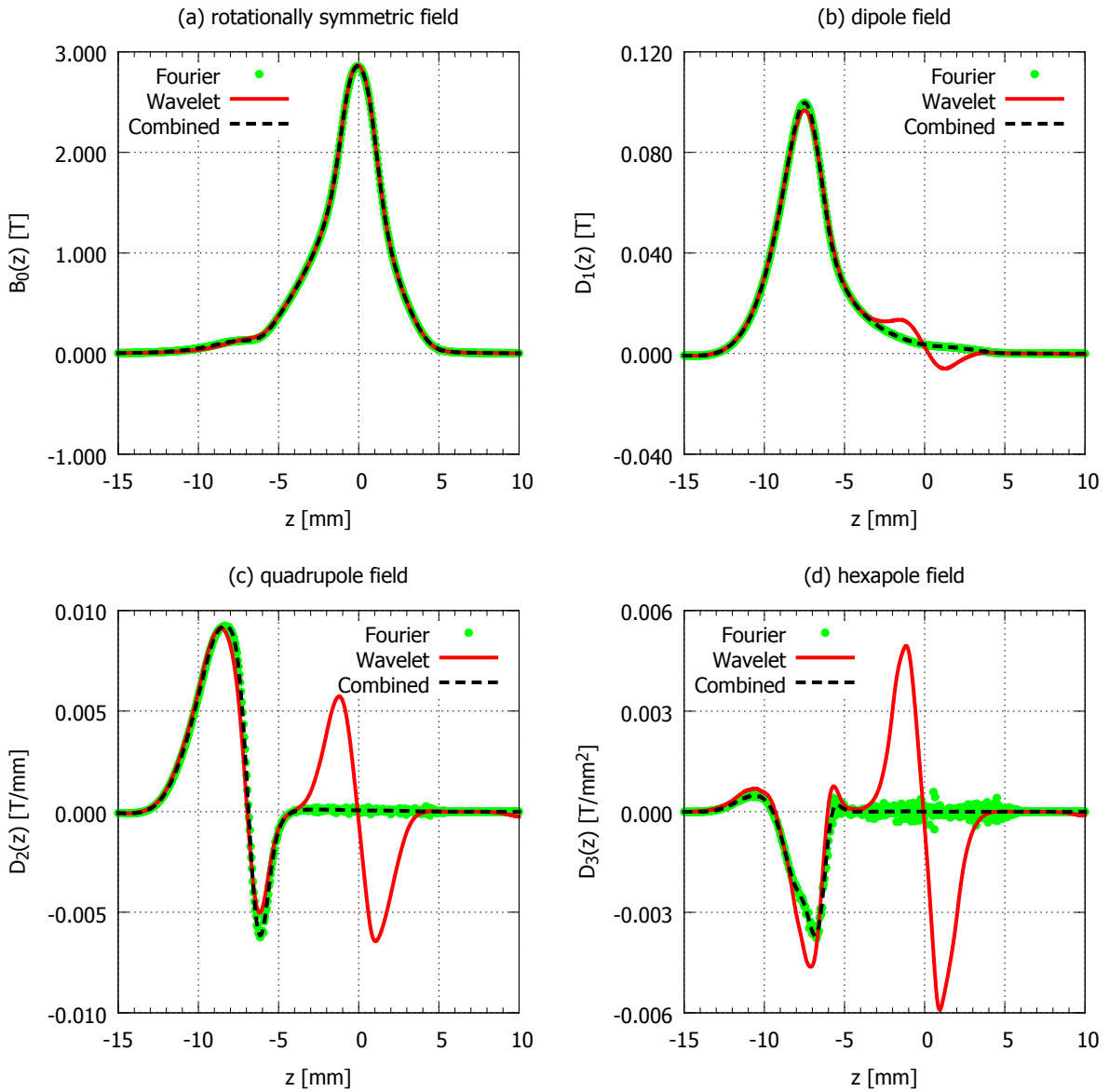


**Figure 5.3:** Axial field functions of the magnetic objective lens with the hole in the pole piece determined by three discussed methods – method based on the Fourier series expansion (green points), method based on the wavelet interpolation (red solid lines), and the combined method (black dashed line).

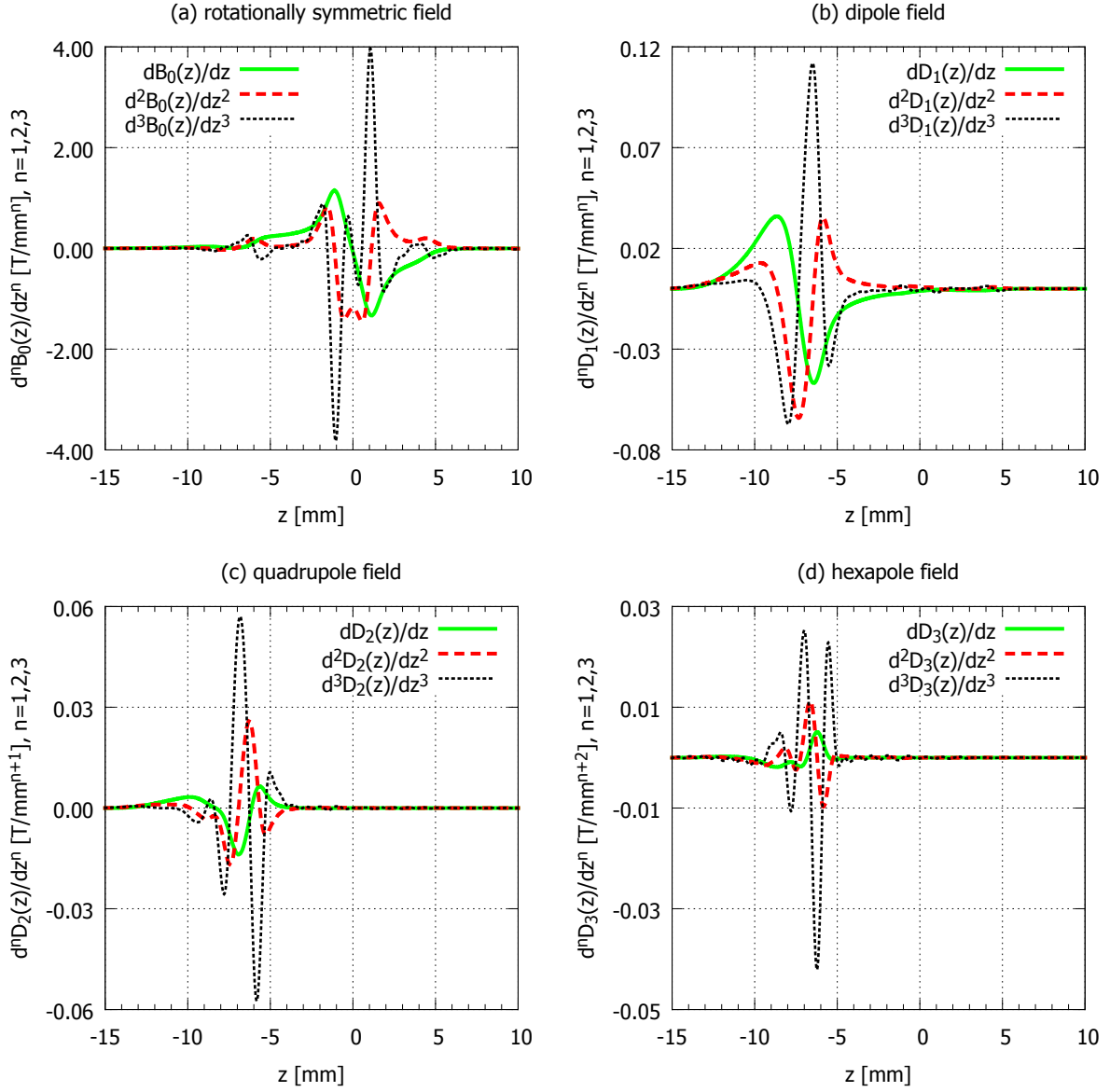


**Figure 5.4:** The first three derivatives of the axial field functions of the magnetic objective lens with the hole in the pole piece evaluated by the combined algorithm.

# 6 Calculation of optical properties of the lens with an elliptic polepiece

Influence of different perturbations of pole piece shape of magnetic lens on optical properties is studied in the following chapter. The method used to calculate axial field functions from the results of 3D calculation and evaluation of aberration coefficients is described in this chapter. At the beginning, the field of the lens is computed. Afterwards, the axial field functions are determined. In the next step, electrons are traced through the lens using radial expansion of the axial field functions interpolation method. Finally, the aberration coefficients are evaluated.

The process is presented on a magnetic lens with an elliptic pole piece. The ellipticity of upper pole piece is 0.1 mm, and the excitation of the lens is 1 000 A-turns.

## 6.1 Calculation of the magnetic field in lens

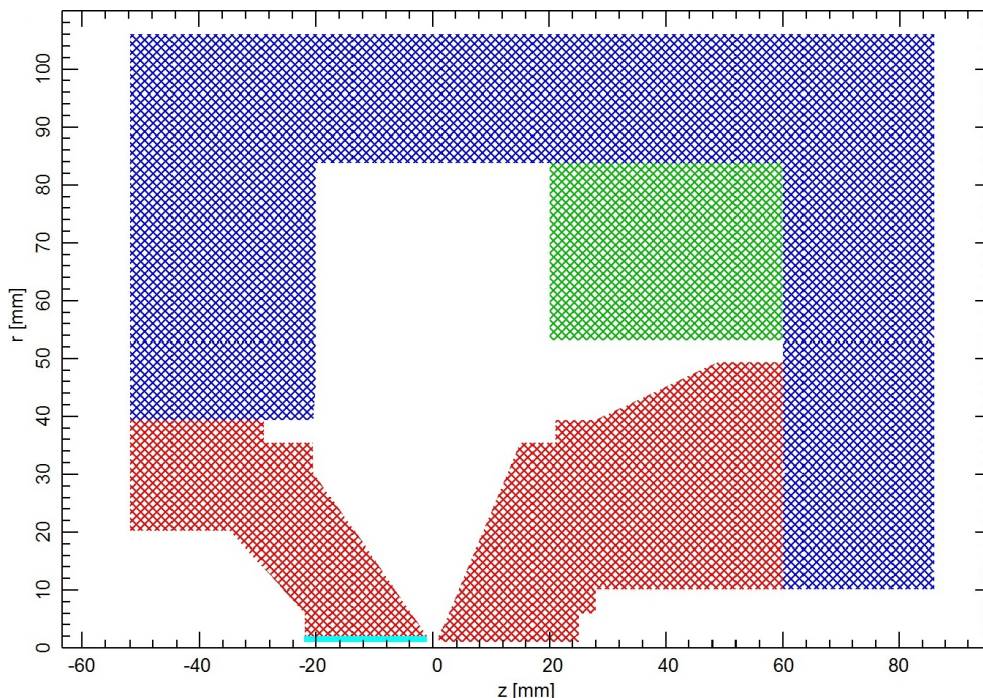


**Figure 6.1:** Magnetic lens with an elliptic pole piece – coil (green), yoke (blue), pole pieces (red), perturbed part of pole piece (light blue). Bore diameter and gap are both 2 mm.

Properties of the modified magnetic objective lens of K. Tsuno [43] with an elliptic pole piece (figure 6.1) are studied. The region of pole pieces parallel to the optical axis

is extended and conical parts of pole pieces are removed. This modification is necessary to avoid an influence of the change of geometry to results of the perturbation theory in the case of highly saturated lens [5]. The axial field of the modified lens is the same as the axial field of the lens with original pole pieces (figure 6.2). The original shape of pole piece is shown in figure 4.2 on page 28.

This exploratory study is performed in EOD [36] using the fine mesh with step 0.05 mm in the area of interest close to the gap, which implies approximately 0.5 million mesh points. The highest possible relative accuracy of the non-linear solver  $1 \cdot 10^{-14}$  is chosen.

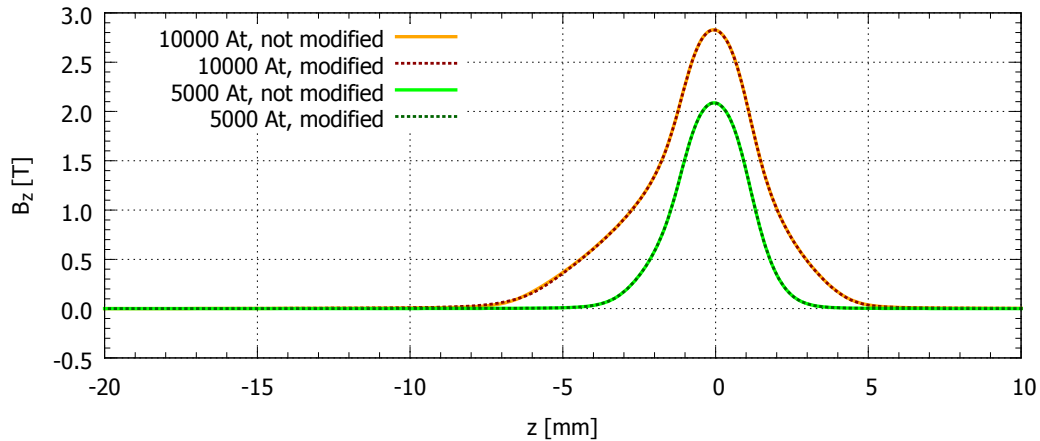


**Figure 6.2:** Comparison of the axial magnetic flux density of the magnetic objective lens and the magnetic objective lens with modified shape of pole pieces for two excitations.

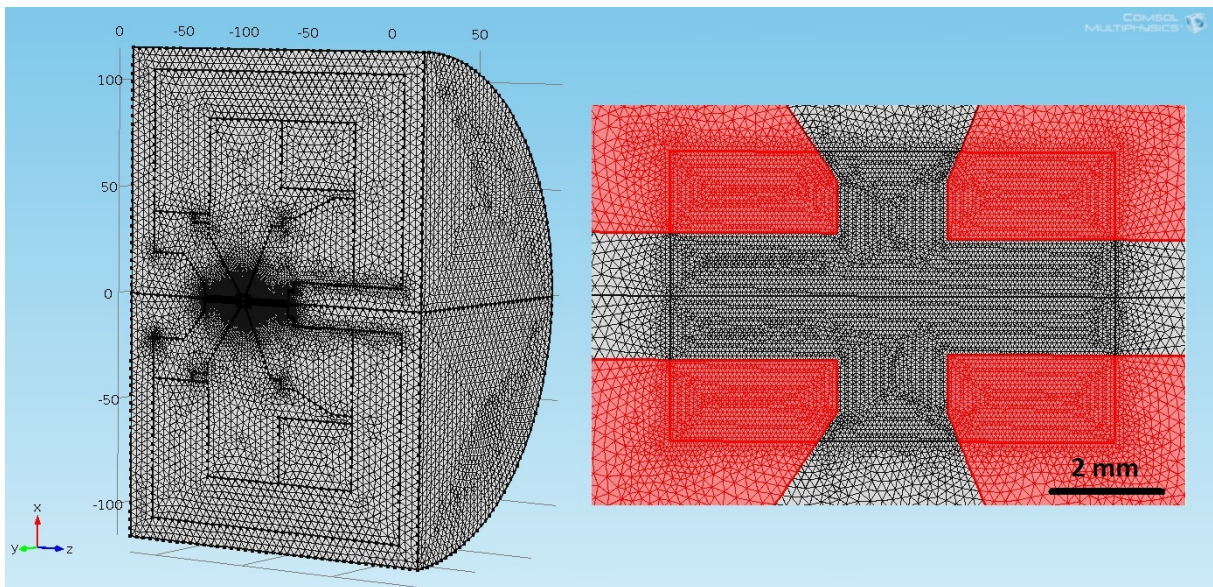


**Figure 6.3:** Fine mesh of the magnetic lens in COMSOL Multiphysics. The undistinguishable black region corresponds to the area of the smallest mesh elements in the gap region, which is shown in detail on the right. Polepieces in the detailed view are red coloured.

The 3D calculation is performed in COMSOL Multiphysics [13] with AC/DC module using the second order finite element method. The smallest mesh element size, used for the 3D calculation, is reduced to 0.084 mm in the gap region close to the axis to achieve sufficient accuracy of the field and reasonable memory consumption. Despite that only

one half of the lens is computed (figure 6.3), the memory consumption is almost 70 GB. The total number of degrees of freedom is about 25 million. Again the relative accuracy of the field computation  $5 \cdot 10^{-8}$  is used. Components of the magnetic flux density are evaluated using built in interpolation methods of COMSOL Multiphysics in 360 points on 50 circles with radii from 0.01 mm to 0.50 mm. The sampling step in axial direction is 0.01 mm.

The 2D calculation applying the perturbation theory is performed in EOD [36] with plugin Tolerancing [12] with the same mesh as for the calculation of magnetic field in the exploratory study discussed above in this section.

## 6.2 Optimization of the axial field function evaluation

The wavelet interpolation of radial dependence of Fourier components, introduced in the section 5.3, is used for determining the axial field functions. Optimization consists of selecting the proper parameters  $d_z$  and  $\sigma$ . The parameters can be optimized according to three different criterions:

1. to get the axial functions oscillation as low as possible
2. to get the standard deviation of the axial function as low as possible
3. to get the higher derivatives of the functions with the lowest level of noise

The first criterion is the simplest one, but also the least strict. Therefore, the results are not necessary as accurate as possible. The second criterion should be more strict, but it is disputable. Are the lowest standard deviation really necessary? Probably they are not, because the lowest standard deviation do not have to imply having the higher derivatives smooth. Especially if the 3D field suffers from a high degree of numerical errors. Consequently, the best criterion seemed to be the third one. Similar criterion as the third one is used by Radlička to find the optimal  $\sigma$  in wavelet interpolation in [44].

In the first optimization step, the optimal  $d_z$  parameter is found. This is provided by varying  $d_z$  with fixed  $\sigma = 2$ . The parameter  $d_z$  was changed from 0.04 mm to 0.50 mm. Seventh derivative of the quadrupole axial field function for different values of  $d_z$  is shown in figure 6.4. Only selected axial field functions from all tested are displayed. The interval of optimal values of  $d_z$  seems to be from 0.08 mm to 0.16 mm. The seventh derivative have perfect shape of maxima and relatively low degree of noise around the nonzero axial field area in this region. For values of  $d_z$  less than 0.06 and greater than 0.2, the seventh derivative is fluctuating.

The second optimization step searches the optimal value of  $\sigma$  parameter. This is provided by varying  $\sigma$  with fixed  $d_z = 0.12$  mm. The parameter  $\sigma$  was changed from 1 to 5. Seventh derivative of the quadrupole axial field function for selected values of  $\sigma$  is shown in figure 6.5. The interval of optimal values seems to be from 1.8 to 3. In this region, the seventh derivative has relatively low degree of noise. For other values of  $\sigma$  the seventh derivative is fluctuating.

As the result, parameters  $d_z = 0.12$  mm and  $\sigma = 2.2$ , which are in the middle of intervals mentioned above, are chosen for further calculations. The axial field functions and their first seven derivatives for the rotationally symmetric and the quadrupole field are shown in figure 6.6. The axial field functions and their derivatives are smooth. A

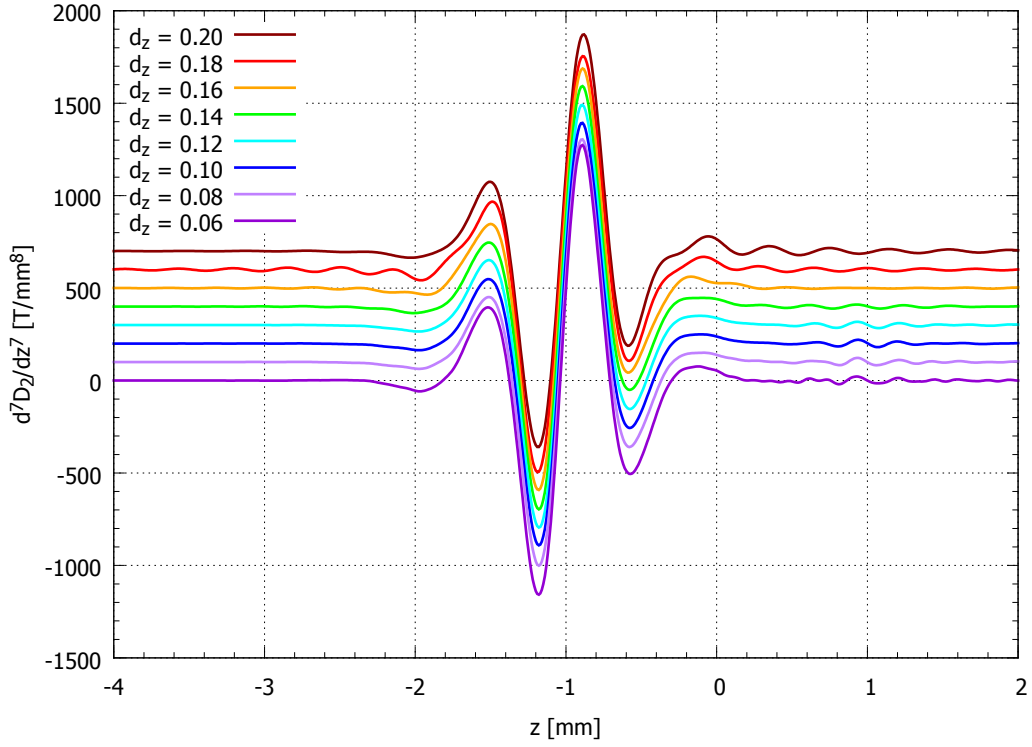


**Figure 6.4:** Seventh derivative of the quadrupole axial field function for different values of  $d_z$ . The second parameter  $\sigma = 2$  is fixed. The functions are shifted with step of  $100 \text{ T mm}^{-8}$ . The ellipticity of upper pole piece is  $100 \mu\text{m}$ , and the excitation of the lens is  $1000 \text{ A-turns}$ .

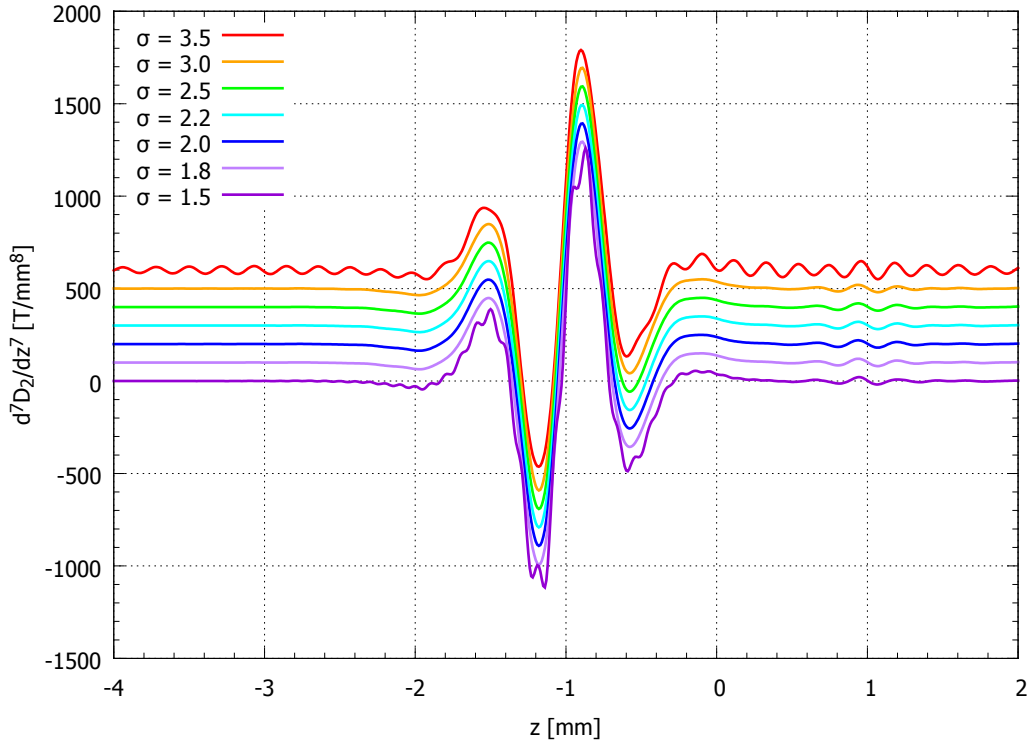


**Figure 6.5:** Seventh derivative of the quadrupole axial field function for different values of  $\sigma$ . The second parameter is fixed to  $d_z = 0.12 \text{ mm}$ . The functions are shifted with step of  $100 \text{ T mm}^{-8}$ . The ellipticity of upper pole piece is  $100 \mu\text{m}$ , and the excitation of the lens is  $1000 \text{ A-turns}$ .

low fluctuation is noticeable only around  $z = 1$  mm in the case of the seventh derivative of the quadrupole field function. This is probably caused by numerical errors in the 3D calculation. However, this assumption cannot be confirmed by calculation of field in denser mesh because of limited computer memory.

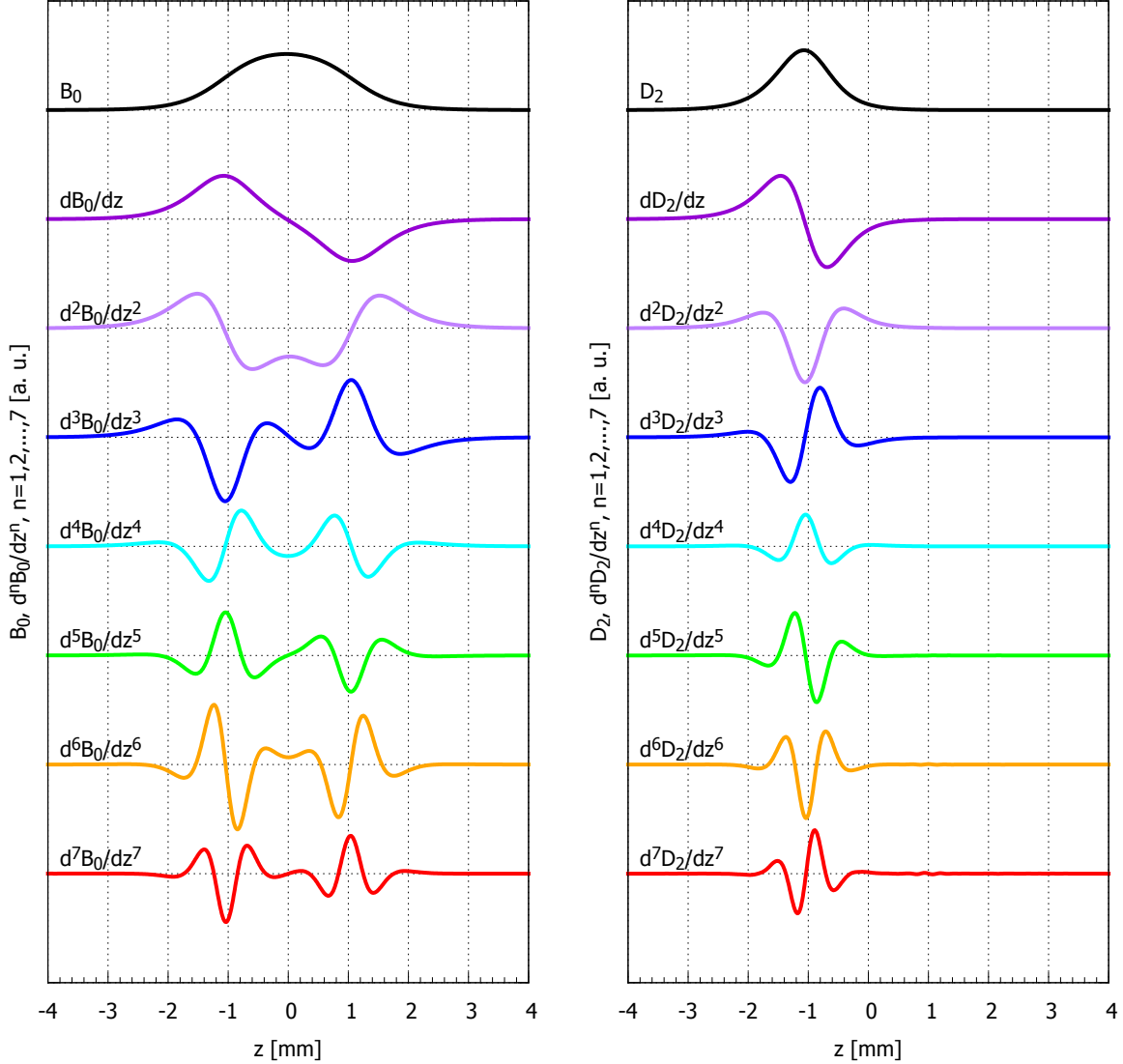


**Figure 6.6:** Axial field functions and its first seven derivatives for the rotationally symmetric (left) and quadrupole (right) field using  $d_z = 0.12$  mm and  $\sigma = 2.2$ . The ellipticity of upper pole piece is 100  $\mu$ m, and the excitation of the lens is 1 000 A-turns.

Figure 6.7 shows the comparison of the axial field functions of the modified magnetic objective lens with ellipticity of upper pole piece of 100  $\mu$ m and excitation of 1 000 A-turns evaluated from the 3D field and computed using the 2D perturbation theory. Rotationally symmetric axial field function evaluated from the 3D field is in very good agreement with the axial field calculated in 2D and its standard deviation is below 1%. A small difference of 3% is observed between the quadrupole axial field function evaluated from the 3D calculation and computed by the perturbation theory in 2D. The standard deviation of the quadrupole axial field function is again below 1%. Finally, the octupole axial field function is evaluated from the 3D field. Its standard deviation is approximately 7% of the value at the minimum. The perturbation theory by Sturrock [11], including the high order terms, does not take into account the octupole component of the field. However, if

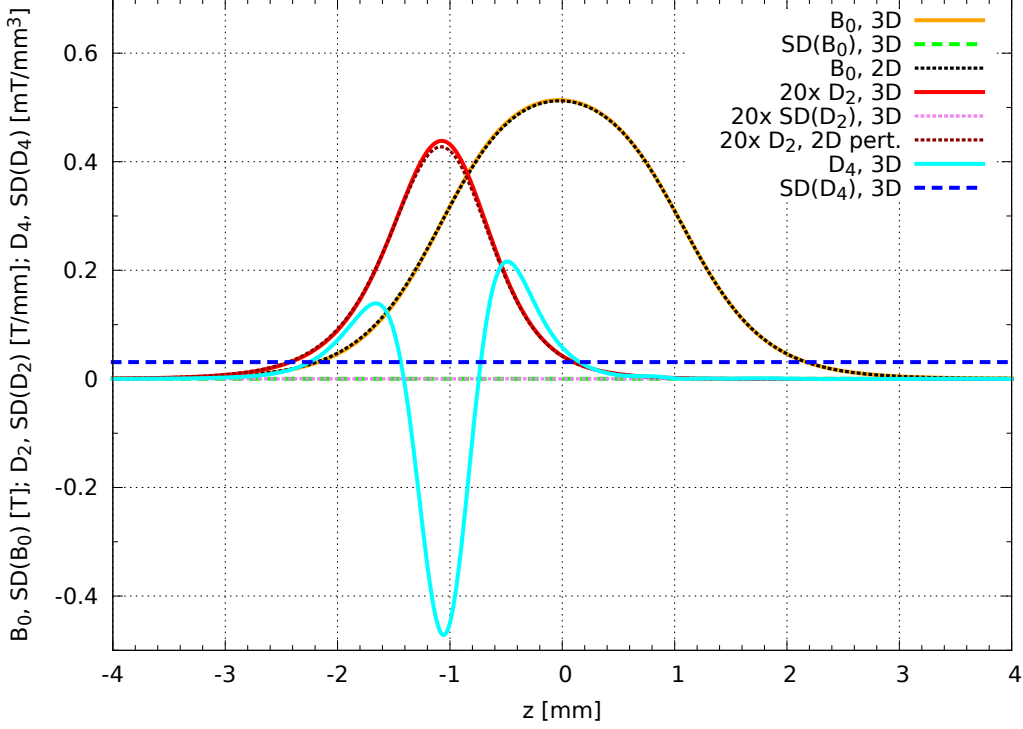


**Figure 6.7:** Comparison of the axial field functions evaluated from the 3D field and computed using the 2D perturbation theory of the lens with the ellipticity of upper pole piece of  $100\ \mu\text{m}$  and the excitation of 1 000 A-turns.

a pure geometrical point of view on transformation of a circle to an ellipse is considered, the octupole field appears (for further details see appendix B on page 67). Finally, the influence of the octupole axial field function on electron trajectories is negligible (figure 6.8), which is in agreement with [10]. Other multipole components are not present.

### 6.3 Particle tracing

To evaluate optical properties of the lens with perturbed pole piece, it is necessary to define the object and the image plane of imaging. Inspiration is found in [3], where the non-modified lens acts as an objective lens for a 200 kV high resolution scanning transmission electron microscope. The object position is  $z_o = -130\ \text{mm}$  and the Gaussian image plane is  $z_i = 0\ \text{mm}$ . Energy of electrons is properly adjusted according to the lens excitation.

The axial field functions and its first five derivatives are imported to EOD using external field interpolation option. Trajectories are computed with the variable-step seventh/eight-order Runge-Kutta-Fehlberg method with relative accuracy  $10^{-14}$  using the first three terms of radial expansion of axial field interpolation method.

Particle tracing consists of two steps. In the first step, the energy of electrons is found using focusing by energy from  $z_o = -130\ \text{mm}$  to  $z_i = 0\ \text{mm}$ . Excitation of 1 000 A-turns implies the energy of 2.107 keV. In the second step, trajectories of an electron beam are calculated. Positions of electrons in the Gaussian image plane  $z_i = 0\ \text{mm}$  are shown in figure 6.8. The electron beam consists of 51 particles – one axial particle and 50 particles with step  $\pi/20\ \text{rad}$  around the  $z$ -axis with the slope from 0.01 to 0.10 mrad in the object plane. Positions of electrons traced using the axial field functions evaluated from the 3D field without the octupole component and including the octupole component are the same.

Positions of electrons traced using the axial field functions computed by the perturbation theory are slightly different, which is caused by the small difference in quadrupole axial field functions.

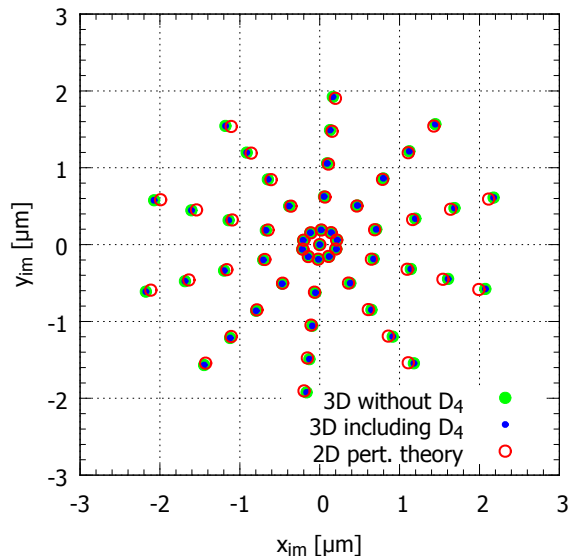


**Figure 6.8:** Comparison of positions of electrons in the Gaussian image plane  $z_i = 0$  mm calculated using the axial field functions evaluated from the 3D field without the octupole component (green), including the octupole component (blue), and calculated using the axial field functions computed by the perturbation theory (red).

## 6.4 Aberration coefficients

Aberration coefficients can be calculated using aberration integrals [8, 9], or by a polynomial least squares fit of particle positions in the Gaussian image plane [3, 46, 50]. The positions of particles  $w_i = x_i + iy_i$  ( $x_i$  and  $y_i$  are Cartesian coordinates) in the Gaussian image plane  $z = z_i$  caused by aberrations are expressed by equation

$$w_i = L_D \gamma_i \omega_i \bar{\omega}_i + \frac{1}{2} \bar{L}_D \bar{\gamma} \omega_i^2 + A_D \gamma_i^2 \bar{\omega}_i + C_F \omega_i + A_1 \bar{\omega}_i + C_S \omega_i^2 \bar{\omega}_i, \quad (6.1)$$

where  $\gamma_i$  is the deflection and  $\omega_i$  is the complex slope of the trajectory at the Gaussian image plane. The meaning of coefficients is:  $L_D$  – coma of deflection,  $A_D$  – astigmatism of deflection,  $C_F$  – defocus with field curvature,  $A_1$  – two-fold axial astigmatism, and  $C_S$  – spherical aberration.

Aberration coefficients  $L_D$ ,  $A_D$ , and  $C_S$  are calculated using aberration integrals implemented in EOD software. Evaluation of  $A_1$ , which is an important defect caused by the parasitic quadrupole field in the case of an ellipticity, is not implemented in EOD software, therefore the two-fold axial astigmatism aberration coefficient needs to be evaluated by the least squares fit of the analytical model — equation (6.1).

Two-fold axial astigmatism coefficient  $A_1$  is evaluated by the least squares fit of an analytical model to the positions of the electrons in the Gaussian image plane  $z_i$ . Figure 6.9 shows the fitted and traced positions of electrons in the Gaussian image plane. Fitted positions and positions of electrons calculated by tracing are in good agreement. Other aberration coefficients are calculated using aberration integrals implemented in EOD.

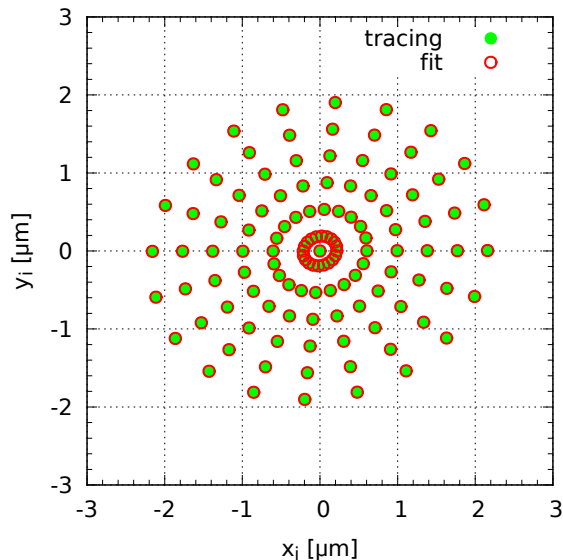


**Figure 6.9:** Comparison of fitted (red) and traced (green) positions of electrons in the Gaussian image plane using the axial field functions evaluated from the 3D field. The magnetic lens pole piece ellipticity is  $100\ \mu\text{m}$  and the excitation of the lens is  $1\ 000\ \text{A-turns}$ .

Aberration coefficients are summarized in table 6.1. The aberration coefficients evaluated using the axial field functions calculated from the 3D field and computed by the 2D perturbation theory are similar. Small difference in range of units of per cent is in the two-fold axial astigmatism coefficient.

**Table 6.1:** Selected aberration coefficients ( $C_S$  and  $A_1$ ) of the magnetic lens with ellipticity of  $100\ \mu\text{m}$  and excitation of  $1\ 000\ \text{A-turns}$ .

aberration coefficient	value
spherical aberration (2D) [mm]	0.417
spherical aberration (3D) [mm]	0.416
two-fold axial astigmatism (2D) [ $\mu\text{m}$ ]	$(84.892\ 4 + i78.137\ 3) \pm (0.001\ 2 + i0.001\ 2)$
two-fold axial astigmatism (3D) [ $\mu\text{m}$ ]	$(83.845\ 1 + i82.106\ 1) \pm (0.001\ 3 + i0.001\ 3)$

# 7 Comparison of 2D and 3D calculation of perturbed magnetic lens

The main goal of this thesis is to explore and illustrate limits of the perturbation theory. The limits can be divided into two groups. The first group covers effects caused by saturation of the lens. The second group deals with magnitudes of perturbations. Modern machining can achieve the tolerances of the pole pieces under  $2\ \mu\text{m}$ . Considering the real tolerances measured in [2], the most of perturbations are below  $20\ \mu\text{m}$  for an ellipticity and a misalignment, respectively  $20\ \text{mrad}$  in the case of a tilt. Perturbations up to  $100\ \mu\text{m}$ , respectively  $100\ \text{mrad}$ , are studied to explore the limits of perturbation theory in this thesis. These limits are demonstrated on the modified magnetic objective lens (figure 6.1 on page 39). Parameters of the axial field function evaluation, introduced in section 5.3, are  $M = 5$ , which means, multipole fields up to decapole component are investigated,  $N = 5$ , which means, the first five terms of series are used, and  $d_z = 0.1\ \text{mm}$  and  $\sigma = 2.2$ , according to section 6.2. The object position is  $z_o = -130\ \text{mm}$  and the Gaussian image plane is  $z_i = 0\ \text{mm}$ . Energy of electrons is properly adjusted according to the lens excitation, similarly as in section 6.3.

## 7.1 Influence of saturation of the magnetic lens with an elliptic pole piece

An influence of saturation of the magnetic lens on suitability of the perturbation theory is investigated by comparing the results obtained by 3D calculations and by calculations using the perturbation theory. The ellipticity of the pole piece is  $2\ \mu\text{m}$ , and the excitation is 1 000, 2 000, 3 000, 4 000, 5 000, and 10 500 A-turns. Table 7.1 summarizes optical properties of the magnetic lens for different excitations calculated using EOD software.

**Table 7.1:** Optical properties of the magnetic lens for different excitations calculated using EOD software. Object and image planes of the lens are  $z_o = -130\ \text{mm}$  and  $z_i = 0\ \text{mm}$ .

excitation [A-turns]	beam energy [keV]	magnification	beam rotation [rad]	spherical aberration [mm]
1 000	2.107	$-5.674 \cdot 10^{-3}$	2.036	0.429
2 000	8.380	$-5.705 \cdot 10^{-3}$	2.038	0.432
3 000	18.772	$-5.854 \cdot 10^{-3}$	2.047	0.439
4 000	34.285	$-6.638 \cdot 10^{-3}$	2.083	0.461
5 000	52.721	$-7.598 \cdot 10^{-3}$	2.135	0.474
10 500	198.582	$-1.428 \cdot 10^{-2}$	2.315	0.596

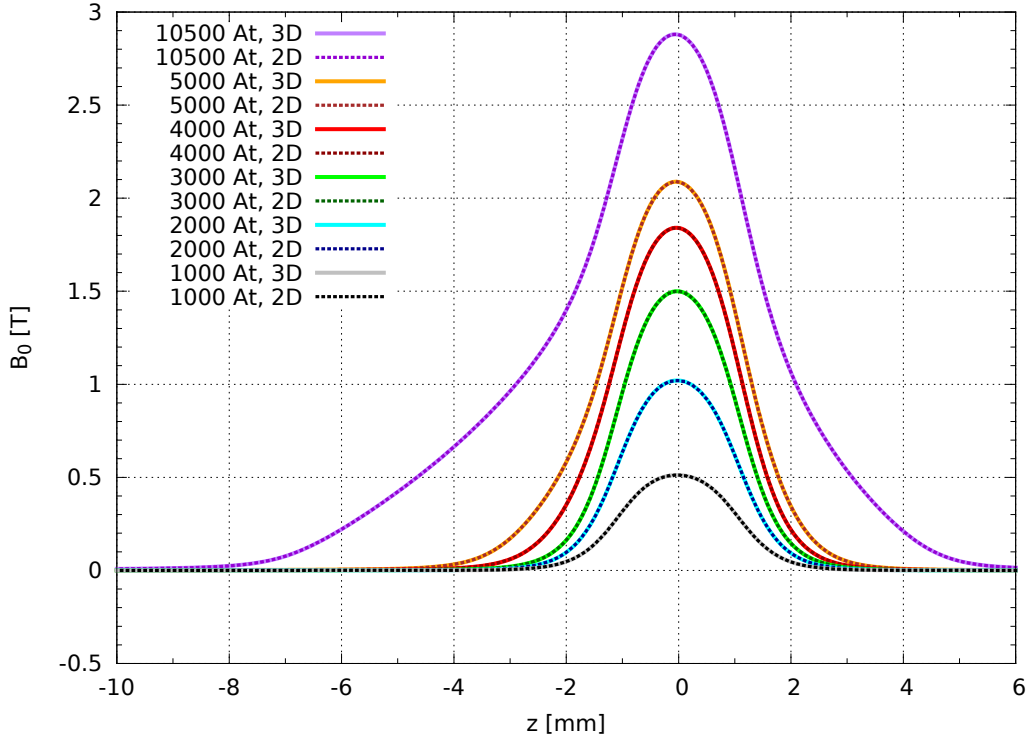


**Figure 7.1:** Rotationally symmetric axial field components  $B_0$  for different exciations of the lens computed using 2D (dotted lines) and 3D calculation (solid lines).

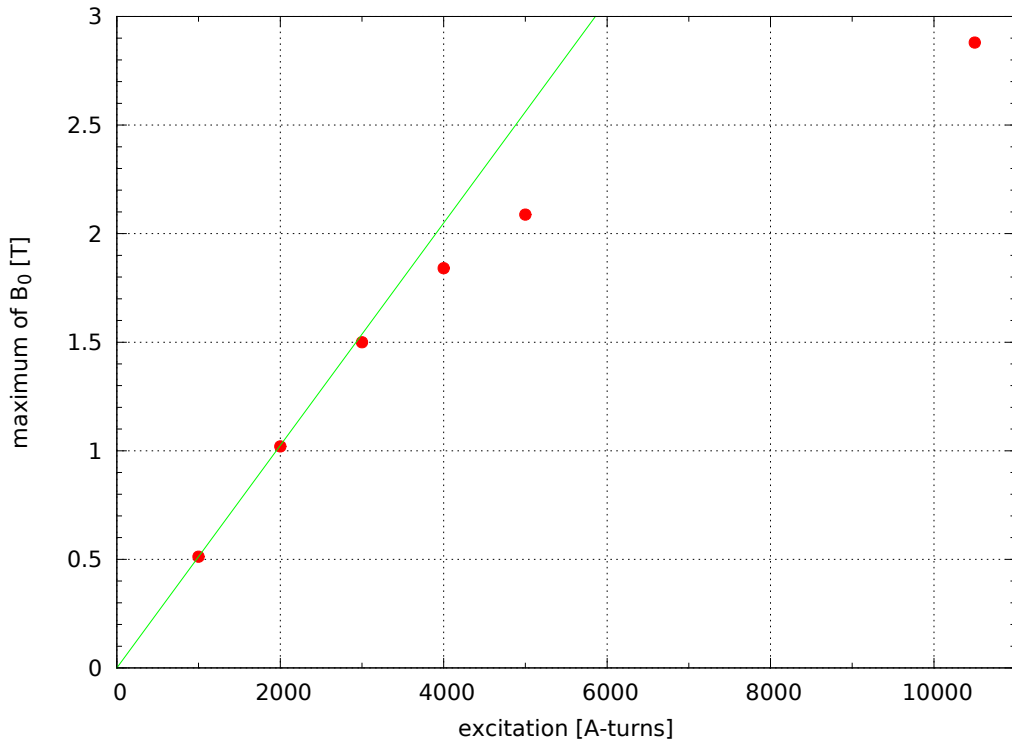


**Figure 7.2:** Maxima of the rotationally symmetric axial field components  $B_0$  for different exciations of the lens. If the lens is not saturated, the maximum of  $B_0$  is linear to the excitation. The linear dependence, shown by the green line, is extrapolated from the maximum of  $B_0$  for the excitation of 1000 A-turns.

Rotationally symmetric axial field components  $B_0$  are shown in figure 7.1. Standard deviations of  $B_0$  evaluated from the 3D solution of the field are below 1% of value of maxima. Saturation of the lens is noticeable in figure 7.2. If the lens is not saturated, the maxima of  $B_0$  are linear to the excitation, which is fulfilled for excitations of 1 000, 2 000, and 3 000 A-turns. In the case of non-saturated lens, the axial field  $B_0$  rises in the same position around  $z = -3$  mm. For higher excitations the lens saturates and the axial field rises in the lower values of  $z$  coordinate (figure 7.1).

Quadrupole axial field functions  $D_2$  are shown in figures 7.3 and 7.4. Standard deviations of  $D_2$  evaluated from the 3D solution of the field are below 1% of value of maxima. The function computed using the perturbation theory is for lower excitations of the lens (1 000 and 2 000 A-turns) in perfect agreement with the function evaluated from the 3D field. For higher excitations, the function calculated using the perturbation theory reaches higher values than the corresponding function determined from the 3D field. The differences are below 1%. In the case of excitation 3 000 A-turns, the shape is similar, but the maximum of  $D_2$  computed using the perturbation theory is about 3% higher. For 4 000 A-turns, the shape is slightly different and the maximum of  $D_2$  by the perturbation theory is approximately 7% higher. The different shape of the axial function is more significant for higher saturation of the lens. The onset and the end of the axial function is similar, but the middle part is different. The function calculated using the perturbation theory rises more rapidly, whereas the function evaluated from the 3D field has a staircase growth in two steps — the first is the onset; the second is approximately in the area of the onsets of functions for lower excitations around  $z = -2$  mm. The maximum of  $D_2$  computed using the perturbation theory is about 10% higher in the case of 5 000 A-turns. The difference rises up to 16% for the excitation of 10 500 A-turns, which is corresponding to the performance of the lens situated as an objective lens in the 200 kV scanning transmission electron microscope. Differences in maxima of the axial quadrupole field function are summarized in the table 7.2.

Another important effect, connected to the saturation of magnetic materials, is the penetration of the perturbation multipole field into the material. Consequently, if the lens is saturated, the relative permeability of material can be very low [5]. Influence of the relative permeability of the material near the pole piece tip to the difference in maxima of the quadrupole axial field functions of the magnetic lens with an elliptic pole piece is summarized in table 7.2. The perturbation theory is perfectly suitable, if the relative permeability of material is high, respectively if the lens is not saturated. With rising excitation, the lens becomes saturated and the relative permeability of material decreases. If the relative permeability is below 100, the results obtained using the perturbation theory are inaccurate. This conclusion is in agreement with [5].

**Table 7.2:** Relative permeability  $\mu_r$  of the material near the pole piece tip and difference in the maxima of the quadrupole axial field functions  $D_2$  of the magnetic lens with an elliptic pole piece for different excitations of the lens. The ellipticity of the lens is 2  $\mu$ m.

excitation [A-turns]	$\mu_r$ near the pole piece tip	difference in $D_2$
1 000	$\sim 1\,500$	$< 1\%$
2 000	$\sim 700$	$< 1\%$
3 000	$\sim 100$	3%
4 000	$\sim 15$	7%
5 000	$\sim 10$	10%
10 500	$\sim 5$	16%

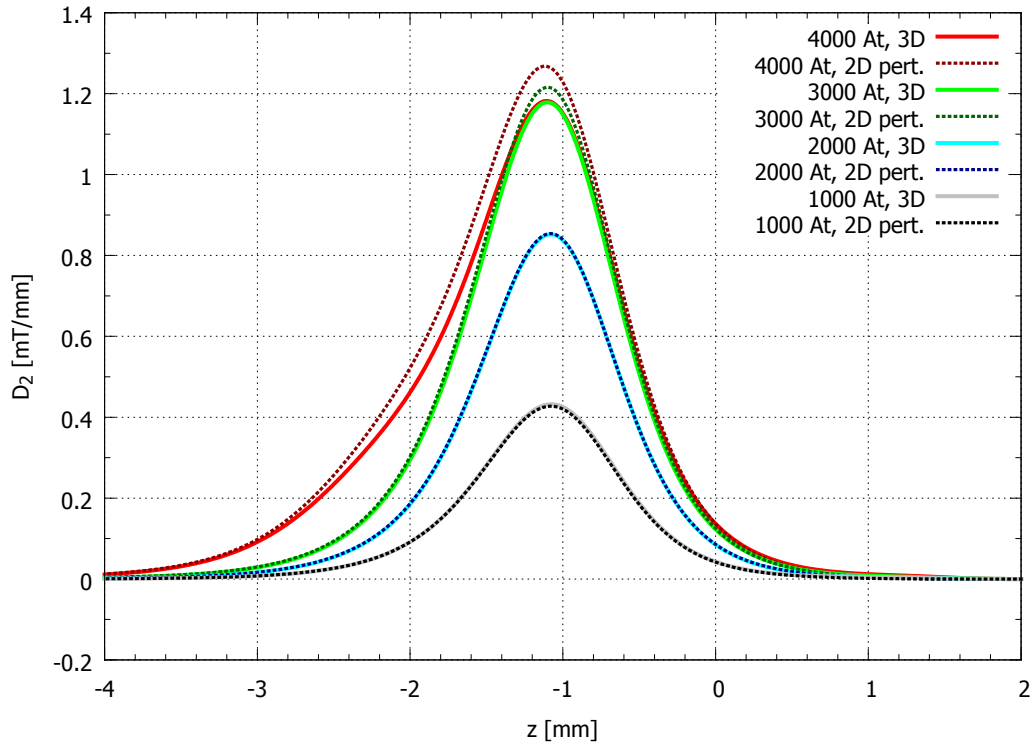


**Figure 7.3:** Quadrupole axial field functions  $D_2$  for different exciations of the undersaturated lens computed using 2D perturbation theory (dotted lines) and 3D calculation (solid lines). The ellipticity of the pole piece is  $2\ \mu\text{m}$ .

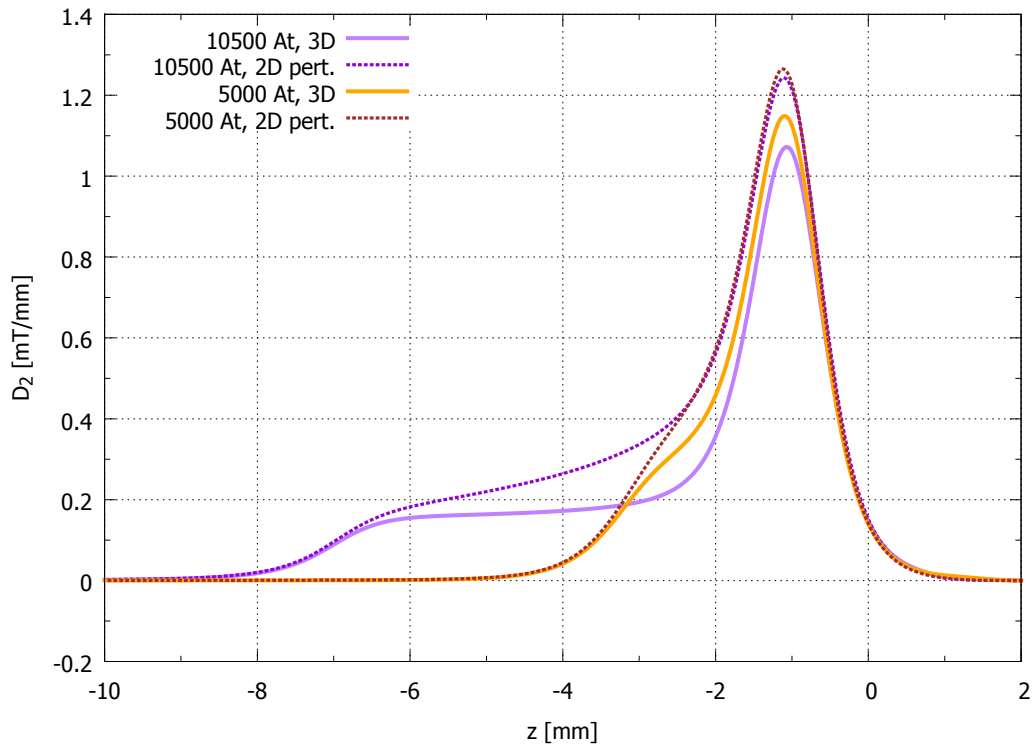


**Figure 7.4:** Quadrupole axial field functions  $D_2$  for different exciations of the saturated lens computed using 2D perturbation theory (dotted lines) and 3D calculation (solid lines). The ellipticity of the pole piece is  $2\ \mu\text{m}$ .

An elliptic pole piece of the lens, respectively the parasitic quadrupole field, causes a two-fold astigmatism. Two-fold astigmatism aberration coefficients, evaluated by the least square fit introduced in the section 6.4, are summarized in the table 7.3. Standard deviations of the aberration coefficients are around 1%. Magnitudes of the coefficients evaluated using the perturbation theory and the 3D field are almost the same up to the excitation of 4 000 A-turns. For higher excitations, the difference between the coefficients is getting higher as the difference in maxima and shape of the quadrupole axial field functions rises. The two-fold astigmatism aberration coefficient evaluated using the axial field functions calculated using the perturbation theory is approximately 1.5-times higher than the coefficient calculated using the axial field functions evaluated from the 3D solution of the field for the excitation of 10 500 A-turns, so the perturbation theory does not produce accurate results. According to this, it is disputable, how accurate are results in [3].

**Table 7.3:** Size of two-fold axial astigmatism aberration coefficients  $|A_1|$  caused by the quadrupole field component of the magnetic lens with an elliptic pole piece for different excitations of the lens calculated by the fit. The ellipticity of the lens is  $2\ \mu\text{m}$ .

excitation [A-turns]	$ A_1 $ (2D) [ $\mu\text{m}$ ]	$ A_1 $ (3D) [ $\mu\text{m}$ ]	difference in $ A_1 $
1 000	2.31	2.34	1 %
2 000	2.25	2.33	3 %
3 000	2.26	2.33	3 %
4 000	2.50	2.42	3 %
5 000	2.73	2.39	14 %
10 500	4.04	2.70	50 %

Standard deviations of other multipole axial field functions are similar or higher than the function values, therefore no other multipole fields are present. However, if the pure geometrical point of view on elliptic deformation of a circle is considered, additional octupole field can appear (for further details see appendix B on page 67).

## 7.2 Influence of the magnitude of ellipticity

The limiting ellipticity magnitude of the magnetic lens pole piece for the legitimacy of the perturbation theory is examined in the same way as in the previous section. Results obtained by 3D calculations and by calculations employing the 2D perturbation theory are compared for the ellipticity of the pole piece of  $2\ \mu\text{m}$ ,  $20\ \mu\text{m}$ ,  $50\ \mu\text{m}$ , and  $100\ \mu\text{m}$ . The excitation of the lens is 1 000 A-turns.

Quadrupole axial field functions  $D_2$  computed using the perturbation theory seems to be for lower magnitudes of the ellipticity in perfect agreement with the function evaluated from the 3D field (figure 7.5). The shape of the functions is similar for all discussed elliptic pole pieces. However, the maximum of the function calculated using the perturbation theory is lower than the maximum of the function determined from the 3D field. The difference of maxima is approximately 1% for the ellipticity of  $2\ \mu\text{m}$ , 2% for  $20\ \mu\text{m}$ , 2% for  $50\ \mu\text{m}$ , and 3% for  $100\ \mu\text{m}$ . Standard deviations of quadrupole axial field functions evaluated from the 3D solution of the field are below 1% of value at the maxima.

The presence of elliptic pole piece of the lens causes the parasitic quadrupole field, which inflicts the two-fold astigmatism. Two-fold astigmatism aberration coefficients, evaluated by the least square fit introduced in the section 6.4, are summarized in the table 7.4. Standard deviations of the aberration coefficients are around 1%. Magnitudes of the

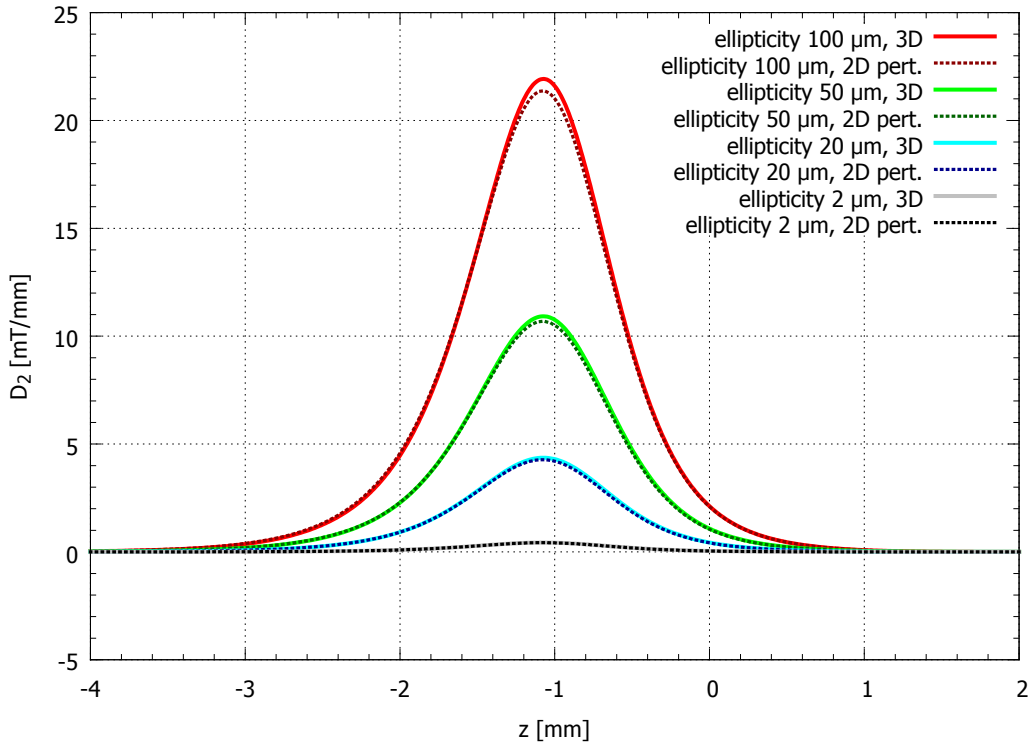


**Figure 7.5:** Quadrupole axial field functions  $D_2$  for different values of the ellipticity computed using 2D perturbation theory (dotted lines) and 3D calculation (solid lines). The excitation of the lens is 1 000 A-turns.

coefficients evaluated using the perturbation theory are perfectly linear to the ellipticity (figure 7.6). The magnitude of the coefficients evaluated using the perturbation theory and the 3D field is almost the same, respectively the coefficients calculated using 3D field are slightly higher, which is noticeable mainly for higher magnitudes of ellipticity. The perturbation theory provides relatively accurate results. Similar analysis was done by J. A. Rouse [17], summarized on page 58 in figure 34. However, in his study the coefficients calculated using 3D field are lower than the coefficients evaluated using the perturbation theory. On the other hand, the discussed magnetic lenses are entirely different.

**Table 7.4:** Size of two-fold axial astigmatism aberration coefficients  $|A_1|$  caused by the quadrupole field component of the magnetic lens with an elliptic pole piece for different magnitudes of ellipticity calculated by the least square fit. The excitation of the lens is 1 000 A-turns.

ellipticity [ $\mu\text{m}$ ]	$ A_1 $ (2D) [ $\mu\text{m}$ ]	$ A_1 $ (3D) [ $\mu\text{m}$ ]	difference in $ A_1 $
2	2.31	2.34	1 %
20	23.0	23.7	3 %
50	57.6	59.2	3 %
100	115	117	2 %

Octupole axial field functions  $D_4$  evaluated from the 3D field are shown in figure 7.7. Standard deviations of  $D_4$  are almost the same for all values of the ellipticity and almost in the same range as the function values. However, this is not true in the case of the highest ellipticity (100  $\mu\text{m}$ ), where the standard deviation is around 6 % of the value at the minimum of  $D_4$ . The presence of the octupole field component is in agreement with the pure geometric interpretation (see appendix B on page 67). However, this field affects

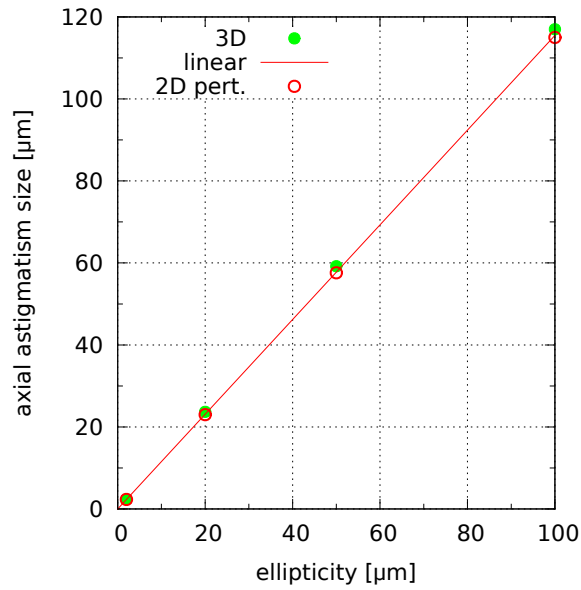


**Figure 7.6:** Two-fold axial astigmatism size  $|A_1|$  calculated by the least square fit as a function of the ellipticity. Linear dependency is extrapolated from the  $|A_1|$  for the ellipticity of  $2\ \mu\text{m}$ . The excitation of the lens is  $1\ 000\ \text{A-turns}$ .

the electron trajectories negligibly (figure 6.8 on page 45).

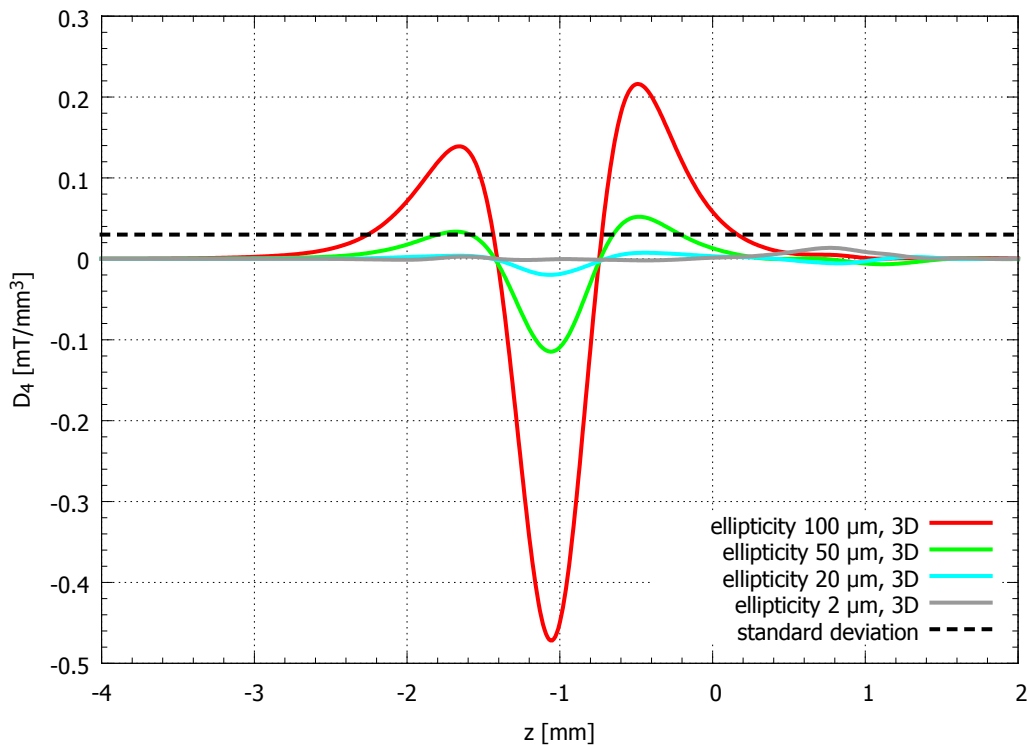


**Figure 7.7:** Octupole axial field functions  $D_4$  for different values of the ellipticity evaluated from the 3D solution of the field. The excitation of the lens is  $1\ 000\ \text{A-turns}$ .

Standard deviations of other multipole axial field functions are higher than their values, therefore no other multipole fields — dipole, hexapole, and decapole — are present. The pure geometric analysis of possible parasitic fields arising from the ellipticity (discussed

in appendix B) predicts the same results.

### 7.3 Misalignment of upper pole piece of the magnetic lens

Misalignment of upper pole piece of the magnetic lens is explored in a similar way as the ellipticity. The misalignment of the pole piece is tested for values  $2\ \mu\text{m}$ ,  $20\ \mu\text{m}$ ,  $50\ \mu\text{m}$ , and  $100\ \mu\text{m}$ . The excitation of the lens is again 1 000 A-turns.

The first order (standard) perturbation theory predicts the presence of parasitic dipole field caused by the pole piece misalignment (introduced in section 4.1). Axial dipole field functions  $D_1$  computed using the perturbation theory seems to be for smaller misalignments in perfect agreement with the functions evaluated from the 3D field (figure 7.8). The shape of the functions is similar for all studied misalignments. Nevertheless, the maximum of the function calculated using the perturbation theory is lower than the maximum of the function determined from the 3D field. The difference of maxima is approximately 1% for the misalignment of  $2\ \mu\text{m}$ , 2% for  $20\ \mu\text{m}$ , 2% for  $50\ \mu\text{m}$ , and 3% for  $100\ \mu\text{m}$ . Standard deviations of dipole axial field functions evaluated from the 3D solution of the field are below 1% of value at the maxima.

The parasitic dipole field caused by the misaligned pole piece of the lens provides a beam deflection and aberrations — coma of deflection and astigmatism of deflection.

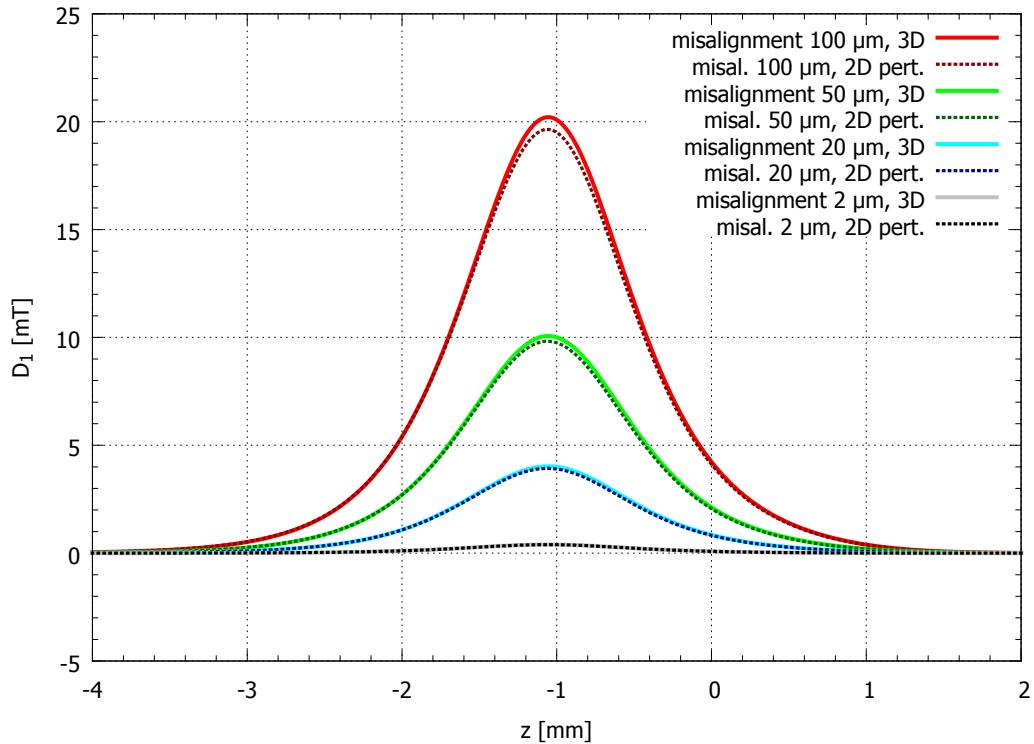


**Figure 7.8:** Dipole axial field functions  $D_1$  for different values of the misalignment computed using 2D perturbation theory (dotted lines) and 3D calculation (solid lines). The excitation of the lens is 1 000 A-turns.

Table 7.5 summarizes beam deflections  $\gamma_i$  caused by the parasitic dipole field. Beam deflections evaluated using the perturbation theory in 2D depend linearly on the misalign-

ment magnitude. Beam deflections calculated using the axial field functions evaluated from the 3D solution of field reach slightly higher values and are also almost linear.

**Table 7.5:** Beam deflection  $\gamma_i$  of the magnetic lens with a misaligned pole piece for different magnitudes of misalignment. The excitation of the lens is 1 000 A-turns.

misalignment [ $\mu\text{m}$ ]	$\gamma_i$ (2D) [ $\mu\text{m}$ ]	$\gamma_i$ (3D) [ $\mu\text{m}$ ]
2	2.00 – i0.03	2.06 – i0.04
20	20.0 – i0.3	20.7 – i0.5
50	50.0 – i0.7	51.8 – i1.2
100	100 – i1	104 – i2

Table 7.6 summarizes coma sizes  $|L_D\gamma_i|$  caused by the parasitic dipole field calculated by the aberration integral implemented in EOD software. Coma size calculated using the 2D perturbation theory is linear to the misalignment. Coma size calculated using the axial field functions evaluated from the 3D field reaches higher values and depends linearly on the misalignment, too (figure 7.9 left).

**Table 7.6:** Coma size  $|L_D\gamma_i|$  of the lens with a misaligned pole piece for different magnitudes of misalignment. The excitation of the lens is 1 000 A-turns.

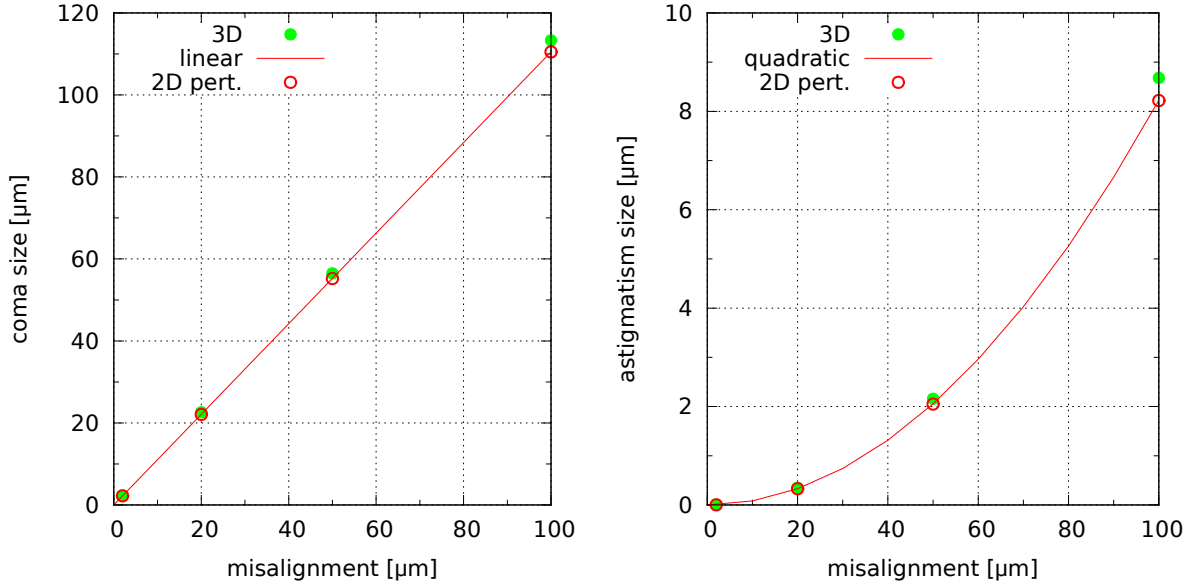
misalignment [ $\mu\text{m}$ ]	$ L_D\gamma_i $ (2D) [ $\mu\text{m}$ ]	$ L_D\gamma_i $ (3D) [ $\mu\text{m}$ ]	difference in $ L_D\gamma_i $
2	2.21	2.25	2 %
20	22.1	22.6	2 %
50	55.2	56.5	2 %
100	110	113	3 %

Table 7.7 summarizes astigmatism sizes  $|A_D\gamma_i^2|$  caused by the parasitic dipole field calculated by the integral implemented in EOD software. Astigmatism size calculated using the 2D perturbation theory depends quadratic on the misalignment. Astigmatism size calculated using the axial field functions evaluated from the 3D field reaches higher values and is also almost quadratic to the misalignment (figure 7.9 right).

**Table 7.7:** Astigmatism size  $|A_D\gamma_i^2|$  of the magnetic lens with a misaligned pole piece for different magnitudes of misalignment. The excitation of the lens is 1 000 A-turns.

misalignment [ $\mu\text{m}$ ]	$ A_D\gamma_i^2 $ (2D) [ $\mu\text{m}$ ]	$ A_D\gamma_i^2 $ (3D) [ $\mu\text{m}$ ]	difference in $ A_D\gamma_i^2 $
2	0.003 3	0.003 4	3 %
20	0.329	0.346	5 %
50	2.05	2.16	5 %
100	8.22	8.68	5 %

Also non-negligible quadrupole axial field functions  $D_2$  are detected in the 3D field (figure 7.10) in addition to expected dipole field. Presence of the quadrupole field is predicted using the perturbation theory including higher order terms [11] mentioned in section 4.1 and corresponds to the geometric interpretation (appendix B on page 67). Standard deviations of quadrupole axial field functions are almost the same for all values of the misalignment in range of units of per cent of the maxima, respectively minima, of the functions.



**Figure 7.9:** Coma size  $|L_D\gamma_i|$  (left) and astigmatism size  $|A_D\gamma_i^2|$  (right) as a function of misalignment. Linear dependency is extrapolated from the  $|L_D\gamma_i|$  for the misalignment of  $2\ \mu\text{m}$ , respectively quadratic dependency is extrapolated from the  $|A_D\gamma_i^2|$  for the misalignment of  $2\ \mu\text{m}$ . The excitation of the lens is 1000 A-turns.

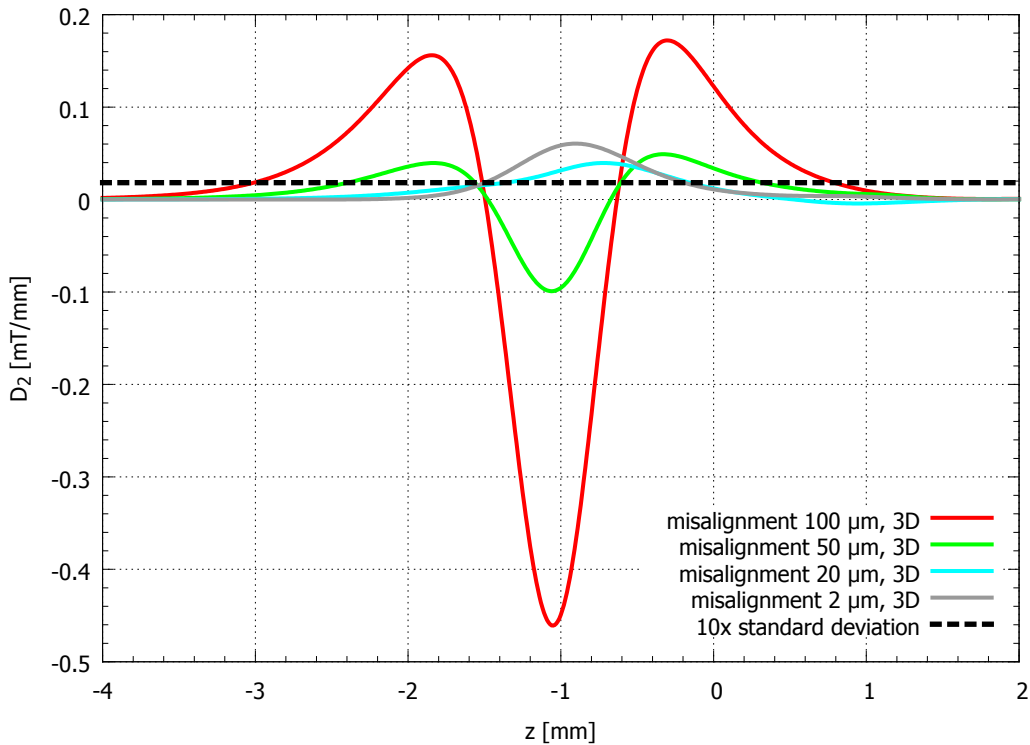


**Figure 7.10:** Quadrupole axial field functions  $D_2$  for different magnitudes of the misalignment evaluated from the 3D solution of the field. The excitation of the lens is 1000 A-turns.

Influence of the parasitic quadrupole field on the beam deflection is negligible. Table 7.8 summarizes axial astigmatism sizes  $|A_1|$  caused by the quadrupole field component, evaluated from the 3D field of the magnetic lens with a misaligned pole piece, for different misalignments calculated by the least square fit. Values of  $|A_1|$  caused by the misalignment

are much smaller than values of  $|A_1|$  caused by the ellipticity (table 7.4). However, the two-fold axial astigmatism is approximately 70-times greater than the astigmatism of deflection for the smallest value of misalignment ( $2\ \mu\text{m}$ ). For greater misalignments, the astigmatism of deflection prevails.

**Table 7.8:** Size of two-fold axial astigmatism aberration coefficients  $|A_1|$  caused by the quadrupole field component, evaluated from the 3D field of the magnetic lens with a misaligned pole piece, for different magnitudes of misalignment calculated by the least square fit. The excitation of the lens is 1 000 A-turns.

misalignment [ $\mu\text{m}$ ]	$ A_1 $ (3D) [ $\mu\text{m}$ ]
2	0.232
20	0.165
50	0.187
100	0.942

Standard deviations of other multipole axial field functions are higher than the function values, therefore multipole fields of higher periodicity — hexapole, octupole, and decapole — are either not present, or are really weak and strongly affected by numerical errors. However, according to the purely geometric point of view, really weak octupole field should appear (appendix B on page 67).

To conclude, the standard (first order) perturbation theory is not as good approximation of pure misalignment as it is traditionally assumed especially for small values of misalignment. It is necessary to consider the parasitic quadrupole field to get the correct result, therefore the perturbation theory including the second order term should be used. On the other hand, the quadrupole field component and the axial astigmatism caused by the misalignment is much smaller than the quadrupole field component and axial astigmatism caused by the ellipticity, therefore if both perturbations — misalignment and ellipticity — are present, the standard first order perturbation theory seems to be an applicable approximation.

## 7.4 Tilt of upper pole piece of the magnetic lens

Tilt of upper pole piece of the magnetic lens is investigated in the same way as the misalignment. The tilt of the pole piece is tested for values 2 mrad, 20 mrad, 50 mrad, and 100 mrad. The axis of tilted pole piece intersects the  $z$ -axis in  $z_t = 0\ \text{mm}$ . The excitation of the lens is 1 000 A-turns. It must be noticed, that the largest tilt is in the case of considered lens in reality unrealizable, because the mass of the tilted pole piece overlaps the optical axis. Nevertheless, this effect does not affect results for  $z > -5\ \text{mm}$ , where the perturbation field is present, therefore it is ignored.

The first order (standard) perturbation theory again predicts the presence of parasitic dipole field caused by the tilted pole piece (introduced in section 4.1). Axial dipole field functions  $D_1$  computed using the perturbation theory are slightly lower than the functions evaluated from the 3D field (figure 7.11). The difference of maxima is approximately 3 % for the tilt of 2 mrad, respectively 4 % for the tilt of 20 mrad, 50 mrad, and 100 mrad. The shape of the functions is similar for all studied tilts. Standard deviations of dipole axial field functions evaluated from the 3D solution of the field are below 1 % of value at the maxima.

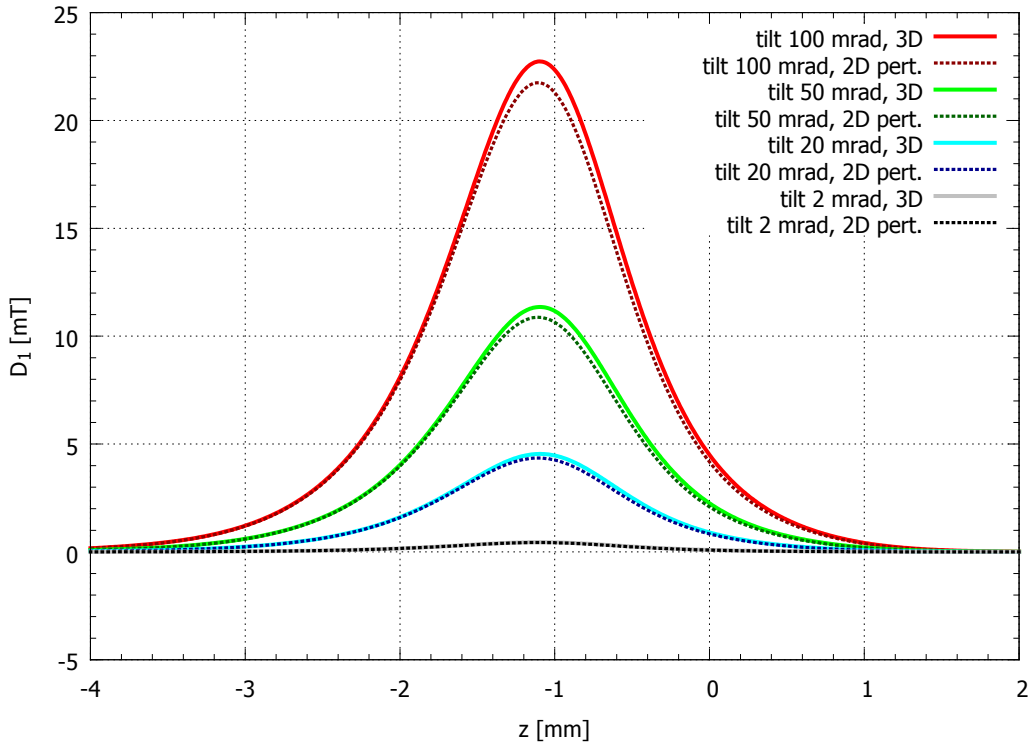


**Figure 7.11:** Dipole axial field functions  $D_1$  for different values of the tilt computed using 2D perturbation theory (dotted lines) and 3D calculation (solid lines). The axis of tilted pole piece intersects the  $z$ -axis in  $z_t = 0$  mm. The excitation of the lens is 1 000 A-turns.

The parasitic dipole field caused by the tilted pole piece of the lens provides, similarly as in the case of the misaligned pole piece discussed in the previous section, a beam deflection and aberrations — coma of deflection and astigmatism of deflection.

Table 7.9 summarizes beam deflections  $\gamma_i$  caused by the parasitic dipole field. Beam deflections evaluated using the perturbation theory in 2D depends linearly on the tilt magnitude. Beam deflections calculated using the axial field functions evaluated from the 3D solution of field reach slightly higher values are linear to the tilt magnitude, too.

**Table 7.9:** Beam deflection  $\gamma_i$  of the magnetic lens with a tilted pole piece for different magnitudes of tilt. The axis of tilted pole piece intersects the  $z$ -axis in  $z_t = 0$  mm. The excitation of the lens is 1 000 A-turns.

tilt [mrad]	$\gamma_i$ (2D) [ $\mu\text{m}$ ]	$\gamma_i$ (3D) [ $\mu\text{m}$ ]
2	$2.49 + i0.08$	$2.55 + i0.09$
20	$24.9 + i0.8$	$25.7 + i0.6$
50	$62.2 + i2.0$	$64.2 + i1.5$
100	$124 + i4$	$128 + i3$

Table 7.10 summarizes coma sizes  $|L_D \gamma_i|$  caused by the parasitic dipole field calculated by the aberration integral implemented in EOD software. Coma size calculated using the 2D perturbation theory is linear to the tilt. Coma size calculated using the axial field functions evaluated from the 3D field reaches slightly higher values and also depends linearly on the tilt (figure 7.12 left).

Table 7.11 summarizes astigmatism sizes  $|A_D \gamma_i^2|$  caused by the parasitic dipole field calculated by the aberration integral implemented in EOD software. Astigmatism size

**Table 7.10:** Coma size  $|L_D\gamma_i|$  of the magnetic lens with a tilted pole piece for different magnitudes of tilt. The axis of tilted pole piece intersects the  $z$ -axis in  $z_t = 0$  mm. The excitation of the lens is 1 000 A-turns.

tilt [mrad]	$ L_D\gamma_i $ (2D) [ $\mu\text{m}$ ]	$ L_D\gamma_i $ (3D) [ $\mu\text{m}$ ]	difference in $ L_D\gamma_i $
2	2.98	3.01	1 %
20	29.8	30.2	1 %
50	74.6	75.7	1 %
100	149	152	2 %

calculated using the 2D perturbation theory depends quadratic on the tilt. Astigmatism size calculated using the axial field functions evaluated from the 3D field reaches higher values and is also almost quadratic to the tilt (figure 7.12 right).

**Table 7.11:** Astigmatism size  $|A_D\gamma_i^2|$  of the magnetic lens with a tilted pole piece for different magnitudes of tilt. The axis of tilted pole piece intersects the  $z$ -axis in  $z_t = 0$  mm. The excitation of the lens is 1 000 A-turns.

tilt [mrad]	$ A_D\gamma_i^2 $ (2D) [ $\mu\text{m}$ ]	$ A_D\gamma_i^2 $ (3D) [ $\mu\text{m}$ ]	difference in $ A_D\gamma_i^2 $
2	0.005 7	0.005 8	2 %
20	0.573	0.591	3 %
50	3.58	3.70	3 %
100	14.3	14.9	4 %

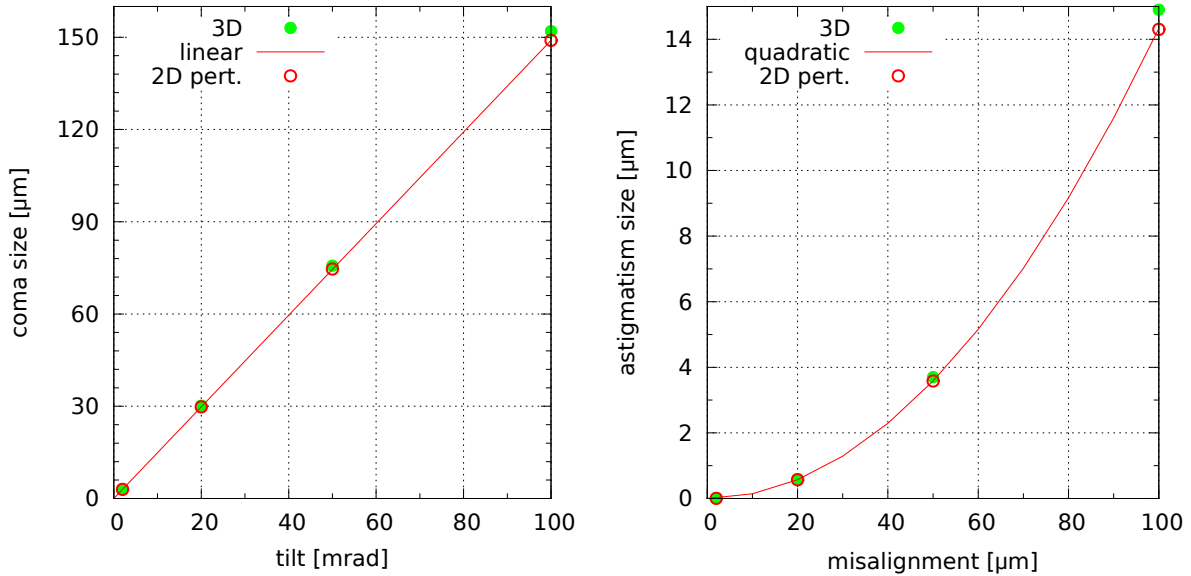


**Figure 7.12:** Coma size  $|L_D\gamma_i|$  (left) and astigmatism size  $|A_D\gamma_i^2|$  (right) as a function of tilt. Linear dependency is extrapolated from the  $|L_D\gamma_i|$  for the tilt of 2 mrad, respectively quadratic dependency is extrapolated from the  $|A_D\gamma_i^2|$  for the tilt of 2 mrad. The axis of tilted pole piece intersects the  $z$ -axis in  $z_t = 0$  mm. The excitation of the lens is 1 000 A-turns.

Again non-negligible quadrupole axial field functions  $D_2$  are detected in the computed 3D field (figure 7.13). Presence of the quadrupole field is predicted using the perturbation theory including higher order terms [11] and corresponds to the geometric interpretation

(appendix B on page 67), similarly as in the case of the misalignment. Standard deviations of quadrupole axial field functions are almost the same for all values of the tilt in range of units of per cent at the maxima of the functions.

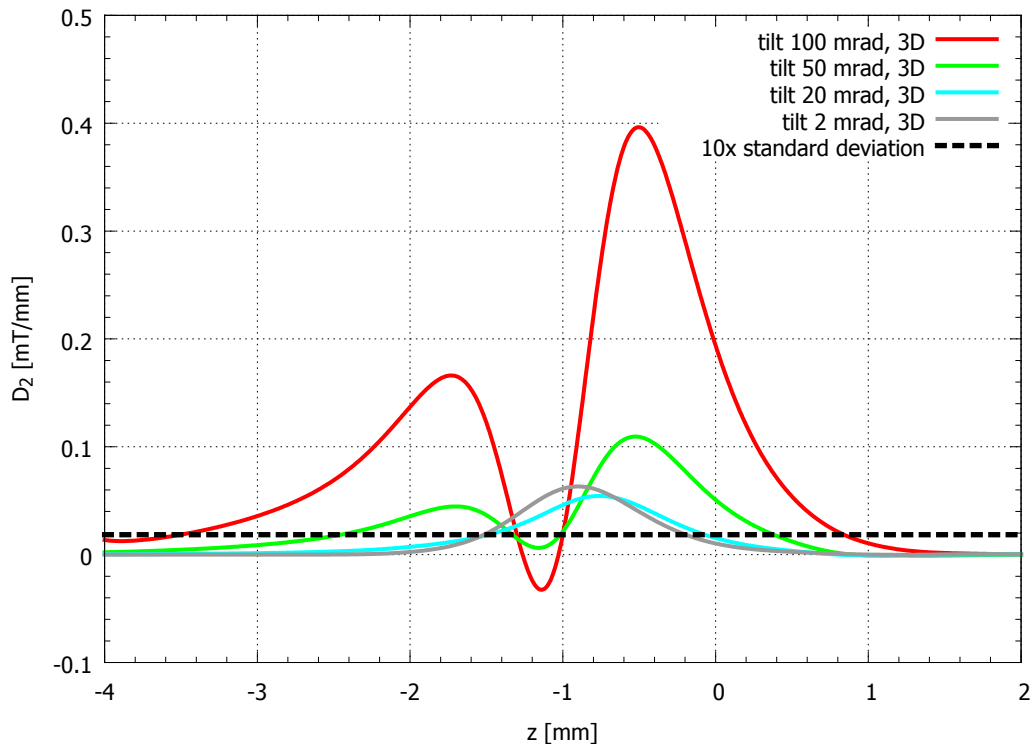


**Figure 7.13:** Quadrupole axial field functions  $D_2$  for different values of the tilt evaluated from the 3D solution of the field. The axis of tilted pole piece intersects the  $z$ -axis in  $z_t = 0$  mm. The excitation of the lens is 1 000 A-turns.

Influence of the parasitic quadrupole field on the beam deflection is again negligible. Table 7.12 summarizes axial astigmatism size  $|A_1|$  caused by the quadrupole field component, evaluated from the 3D field of the magnetic lens with a tilted pole piece, for different magnitudes of tilt calculated by the least square fit. Values of  $|A_1|$  caused by the tilt are also much smaller than values of  $|A_1|$  caused by the ellipticity (table 7.4). However, the two-fold axial astigmatism is approximately 40-times greater than the astigmatism of deflection for the tilt of 2 mrad. For greater tilts, the astigmatism of deflection prevails.

**Table 7.12:** Size of two-fold axial astigmatism aberration coefficients  $|A_1|$  caused by the quadrupole field component, evaluated from the 3D field of the magnetic lens with a tilted pole piece, for different magnitudes of tilt. The axis of tilted pole piece intersects the  $z$ -axis in  $z_t = 0$  mm. The excitation of the lens is 1 000 A-turns.

tilt [mrad]	$ A_1 $ (3D) [ $\mu\text{m}$ ]
2	0.245
20	0.219
50	0.353
100	1.15

Standard deviations of other multipole axial field functions are higher than the function values, therefore multipole fields of higher periodicity — hexapole, octupole, and decapole — are either not present, or are really weak and strongly affected by numerical errors.

However, according to the geometric interpretation, really weak octupole field should appear (appendix B on page 67), similarly as for the lens with a misaligned pole piece.

The conclusion is the same as in the case of misaligned pole piece in the previous section. The standard (first order) perturbation theory is not as good approximation of pure tilt as it is traditionally assumed especially for small tilts. It is necessary to consider the parasitic quadrupole field to get the correct result, therefore the perturbation theory including the second order term should be used. On the other hand, the quadrupole field component and the axial astigmatism caused by the tilt is much lower than the quadrupole field component and axial astigmatism caused by the ellipticity, therefore if both perturbations — tilt and ellipticity — are present, the standard first order perturbation theory seems to be an applicable approximation.

## 8 Conclusion

Rotationally symmetric electron lenses may suffer from parasitic aberrations caused by limited machining precision of otherwise rotationally symmetric electrodes or pole pieces. The imperfection can be classified as an ellipticity, a misalignment, a tilt, or a combination of previous types. The main goal of this work was to introduce a method for evaluating the axial field functions from the 3D solution of the field and to explore the results obtained by the two different techniques for computing electron optical systems with broken rotational symmetry — application of perturbation theory to 2D calculations and 3D simulations. As the result, limits of the perturbation theory were explored and illustrated on the magnetic objective lens used in a high resolution 200 kV scanning transmission electron microscope.

Three different algorithms for the calculation of axial multipole field functions from the 3D solution of the field were introduced (chapter 5) and tested on the magnetic objective lens with the hole in the pole piece (section 5.4). The best results were obtained using the wavelet interpolation of radial dependence of Fourier components described in section 5.3. The functions are interpolated in all positions along the optical axis from multipole components of the field. Evaluated axial multipole field functions and their derivatives were smooth and continuous, which is necessary for accurate ray tracing, for evaluation of aberration integrals, or for computing aberration coefficients using differential algebra method. Design of 3D field interpolation algorithm is very important result of this thesis. It offers an opportunity of very accurate calculation of optical properties of lenses with complicated geometry, which is impossible to reach with standard field interpolation in the mesh nodes.

The limits of the perturbation theory were explored by the comparison of axial multipole field functions and selected aberration coefficients obtained using the perturbation theory in 2D to the results evaluated using the 3D solution of the field. The study covered the influence of magnetic saturation of the material (section 7.1) and the influence of magnitudes of different perturbations (sections 7.2 to 7.4).

The standard perturbation theory is suitable for non-saturated magnetic lenses, but it provides inaccurate results for saturated magnetic lenses. With rising excitation (over 3000 A-turns), the lens becomes saturated and the relative permeability of material decreases. If the relative permeability of pole piece tip is below 100, the results using the perturbation theory are inaccurate, as was predicted in [5]. For the excitation of 10500 A-turns, which corresponds to the performance of the lens situated as an objective lens in the 200 kV scanning transmission electron microscope, the difference at the maximum of the quadrupole axial field function was 16% and the two-fold astigmatism aberration coefficient evaluated using the axial field functions calculated using the perturbation theory was approximately 1.5-times higher than the coefficient calculated using the axial field functions evaluated from the 3D solution of the field. According to this, it is disputable, how accurate are results published in [3]. Consequently, an extension of the standard

perturbation theory to the saturated magnetic lenses would be useful.

Influence of the pole piece ellipticity, misalignment, and tilt were further studied on non-saturated lens. The standard first order perturbation theory, which substitutes the ellipticity of pole piece by parasitic quadrupole field, provides applicable results for all studied ellipticity magnitudes (from  $2\ \mu\text{m}$  to  $100\ \mu\text{m}$ ). The difference at the maxima of quadrupole axial field functions and the difference in the corresponding two-fold axial astigmatism size were both less than 4%. In the case of the ellipticity of  $100\ \mu\text{m}$ , the noticeable parasitic octupole field was determined from the 3D solution of the field in addition to the quadrupole field. However, the weak octupole field had negligible effect on the optical properties.

The standard first order perturbation theory predicts only the presence of parasitic dipole field caused by the pole piece misalignment. However, the analysis of the 3D field gave parasitic dipole and quadrupole fields, as was predicted by the Fourier analysis of a misaligned circle (appendix B). Differences in dipole axial field functions, beam deflection and related aberrations — coma of deflection and astigmatism of deflection — were less than 5%, which means still sufficient approximation compared to the fully 3D solution. The main problem is the additional parasitic quadrupole field causing the two-fold axial astigmatism. In the case of  $2\ \mu\text{m}$  misalignment, the two-fold axial astigmatism is approximately 70-times greater than the astigmatism of deflection, therefore the standard first order perturbation theory is not as good approximation. A possible solution could be applying the perturbation theory including higher order terms [11], which means, the misalignment of pole piece would be substituted by two parasitic fields — dipole and quadrupole.

In the case of the tilt, the situation is the same as for the misalignment. The standard first order perturbation theory again predicts only the presence of parasitic dipole field caused by the tilted pole piece. However, the analysis of the 3D field gave, in agreement with the Fourier analysis of a misaligned circle, parasitic dipole and quadrupole fields. Differences in dipole axial field functions, beam deflection and related aberrations — coma of deflection and astigmatism of deflection — were less than 5%, which again means sufficient approximation compared to the fully 3D solution. The main problem is again the parasitic quadrupole field causing the two-fold axial astigmatism. In the case of  $2\ \text{mrad}$  tilt, the two-fold axial astigmatism is approximately 40-times greater than the astigmatism of deflection, therefore the standard first order perturbation theory is not as good approximation. A possible solution could be applying the perturbation theory including higher order terms [11] similarly as in the case of misalignment, which means, the tilt of pole piece would be substituted by two parasitic fields — dipole and quadrupole.

The standard perturbation theory is a powerful tool for fast computation of electrostatic and non-saturated magnetic lenses with elliptic electrodes or pole pieces. In the case of misalignment and tilt, it is important to consider also the second order term of the perturbation theory causing the axial astigmatism. Perturbation theory is often used to determine the strength of stigmators and deflectors, which are necessary to correct parasitic aberrations arising from the inaccuracy of machining of the lens. If the axial astigmatism of misalignment and tilt is not considered, the power of stigmators may be underestimated. If the same size of ellipticity and misalignment is assumed the difference of stigmator power is about 10%.

# A Useful relations

## A.1 Matrices used for the calculation of axial multipole field functions from the 3D solution of the field

The matrices in equation (5.4) on page 31 are

$$\mathbf{A} = \begin{bmatrix} B_0(z) \\ B_0(z)' \\ B_0(z)'' \\ B_0(z)^{(3)} \\ B_0(z)^{(4)} \\ B_0(z)^{(5)} \end{bmatrix}, \mathbf{F} = \begin{bmatrix} C_{z,0}(r_1, z) \\ C_{z,0}(r_2, z) \\ \dots \\ C_{z,0}(r_R, z) \\ C_{r,0}(r_1, z) \\ \dots \\ C_{r,0}(r_R, z) \end{bmatrix}, \quad (\text{A.1})$$

$$\mathbf{M} = \begin{bmatrix} 1 & 0 & \frac{-1}{4}r_1^2 & 0 & \frac{1}{64}r_1^4 & 0 \\ 1 & 0 & \frac{-1}{4}r_2^2 & 0 & \frac{1}{64}r_2^4 & 0 \\ & & & \dots & & \\ 1 & 0 & \frac{-1}{4}r_R^2 & 0 & \frac{1}{64}r_R^4 & 0 \\ 0 & -\frac{1}{2}r_1 & 0 & \frac{1}{16}r_1^3 & 0 & -\frac{1}{384}r_1^5 \\ & & & \dots & & \\ 0 & -\frac{1}{2}r_r & 0 & \frac{1}{16}r_R^3 & 0 & -\frac{1}{384}r_R^5 \end{bmatrix}$$

in the case of rotationally symmetric field and

$$\mathbf{A} = \begin{bmatrix} D_m(z) \\ D_m(z)' \\ D_m(z)'' \\ D_m(z)^{(3)} \\ D_m(z)^{(4)} \\ D_m(z)^{(5)} \end{bmatrix}, \mathbf{F} = \begin{bmatrix} C_{z,m}(r_1, z) \\ C_{z,m}(r_2, z) \\ \dots \\ C_{z,m}(r_R, z) \\ C_{r,m}(r_1, z) \\ \dots \\ C_{r,m}(r_R, z) \\ S_{\varphi,m}(r_1, z) \\ \dots \\ S_{\varphi,m}(r_R, z) \end{bmatrix}, \quad (\text{A.2})$$

$$\mathbf{M} = \begin{bmatrix} 0 & r_1^m & 0 & \frac{-1}{4(m+1)}r_1^{m+2} & 0 & \frac{1}{32(m+1)(m+2)}r_1^{m+4} \\ 0 & r_2^m & 0 & \frac{-1}{4(m+1)}r_2^{m+2} & 0 & \frac{1}{32(m+1)(m+2)}r_2^{m+4} \\ & & \dots & & & \\ 0 & r_R^m & 0 & \frac{-1}{4(m+1)}r_R^{m+2} & 0 & \frac{1}{32(m+1)(m+2)}r_R^{m+4} \\ mr_1^{m-1} & 0 & \frac{-(m+2)}{4(m+1)}r_1^{m+1} & 0 & \frac{m+4}{32(m+1)(m+2)}r_1^{m+3} & 0 \\ & & \dots & & & \\ mr_R^{m-1} & 0 & \frac{-(m+2)}{4(m+1)}r_R^{m+1} & 0 & \frac{m+4}{32(m+1)(m+2)}r_R^{m+3} & 0 \\ mr_1^{m-1} & 0 & \frac{-m}{4(m+1)}r_1^{m+1} & 0 & \frac{m}{32(m+1)(m+2)}r_1^{m+3} & 0 \\ & & \dots & & & \\ mr_R^{m-1} & 0 & \frac{-m}{4(m+1)}r_R^{m+1} & 0 & \frac{m}{32(m+1)(m+2)}r_R^{m+3} & 0 \end{bmatrix}$$

in the case of multipole field.

The matrices in equation (5.9) on page 33 are

$$\mathbf{A} = \begin{bmatrix} A_{0,1} \\ A_{1,1} \\ \dots \\ A_{M,1} \\ A_{0,2} \\ \dots \\ A_{M,J} \end{bmatrix}, \mathbf{F} = \begin{bmatrix} B_r(\vec{r}_1) \\ B_\varphi(\vec{r}_1) \\ B_z(\vec{r}_1) \\ B_r(\vec{r}_2) \\ \dots \\ B_z(\vec{r}_P) \end{bmatrix}, \quad (\text{A.3})$$

$$\mathbf{M} = \begin{bmatrix} K_{r,0,1,N}(\vec{r}_1) & K_{r,1,1,N}(\vec{r}_1) & \dots & K_{r,M,1,N}(\vec{r}_1) & K_{r,0,2,N}(\vec{r}_1) & \dots & K_{r,M,J,N}(\vec{r}_1) \\ 0 & K_{\varphi,1,1,N}(\vec{r}_1) & \dots & K_{\varphi,M,1,N}(\vec{r}_1) & 0 & \dots & K_{\varphi,M,J,N}(\vec{r}_1) \\ K_{z,0,1,N}(\vec{r}_1) & K_{z,1,1,N}(\vec{r}_1) & \dots & K_{z,M,1,N}(\vec{r}_1) & K_{z,0,2,N}(\vec{r}_1) & \dots & K_{z,M,J,N}(\vec{r}_1) \\ K_{r,0,1,N}(\vec{r}_2) & K_{r,1,1,N}(\vec{r}_2) & \dots & K_{r,M,1,N}(\vec{r}_2) & K_{r,0,2,N}(\vec{r}_2) & \dots & K_{r,M,J,N}(\vec{r}_2) \\ & & \dots & & & & \\ K_{z,0,1,N}(\vec{r}_P) & K_{z,1,1,N}(\vec{r}_P) & \dots & K_{z,M,1,N}(\vec{r}_P) & K_{z,0,2,N}(\vec{r}_P) & \dots & K_{z,M,J,N}(\vec{r}_P) \end{bmatrix}.$$

The matrices in equation (5.16) on page 35 are

$$\mathbf{A} = \begin{bmatrix} A_{m,1} \\ A_{m,2} \\ \dots \\ A_{m,J} \end{bmatrix}, \mathbf{F} = \begin{bmatrix} C_{r,m}(r_1, z_1) \\ C_{\varphi,m}(r_1, z_1) \\ C_{z,m}(r_1, z_1) \\ C_{r,m}(r_2, z_2) \\ \dots \\ C_{z,m}(r_L, z_L) \end{bmatrix}, \quad (\text{A.4})$$

$$\mathbf{M} = \begin{bmatrix} K_{r,m,1,N}(r_1, z_1) & K_{r,m,2,N}(r_1, z_1) & \cdots & K_{r,m,J,N}(r_1, z_1) \\ K_{\varphi,m,1,N}(r_1, z_1) & K_{\varphi,m,2,N}(r_1, z_1) & \cdots & K_{\varphi,m,J,N}(r_1, z_1) \\ K_{z,m,1,N}(r_1, z_1) & K_{z,m,2,N}(r_1, z_1) & \cdots & K_{z,m,J,N}(r_1, z_1) \\ K_{r,m,1,N}(r_2, z_2) & K_{r,m,2,N}(r_2, z_2) & \cdots & K_{r,m,J,N}(r_2, z_2) \\ & & \cdots & \\ K_{z,m,1,N}(r_L, z_L) & K_{z,m,2,N}(r_L, z_L) & \cdots & K_{z,m,J,N}(r_L, z_L) \end{bmatrix}.$$

## A.2 Derivatives of the Gaussian function

It is useful to know the derivatives of the exponential function in (5.6) and (5.7). If the series (5.8) are calculated with  $N$  equals to five, it is necessary to know the derivatives up to the ninth order. Substituting  $v = z - z_j$  and  $s = \sigma d_z$ , these derivatives are

$$\begin{aligned} g &= \exp\left(-\frac{v^2}{s^2}\right), \\ \frac{dg}{dz} &= -\frac{2v}{s^2} \exp\left(-\frac{v^2}{s^2}\right), \\ \frac{d^2g}{dz^2} &= \left[\frac{4v^2}{s^4} - \frac{2}{s^2}\right] \exp\left(-\frac{v^2}{s^2}\right), \\ \frac{d^3g}{dz^3} &= \left[-\frac{8v^3}{s^6} + \frac{12v}{s^4}\right] \exp\left(-\frac{v^2}{s^2}\right), \\ \frac{d^4g}{dz^4} &= \left[\frac{16v^4}{s^8} - \frac{48v^2}{s^6} + \frac{16}{s^4}\right] \exp\left(-\frac{v^2}{s^2}\right), \\ \frac{d^5g}{dz^5} &= \left[-\frac{32v^5}{s^{10}} + \frac{160v^3}{s^8} - \frac{120v}{s^6}\right] \exp\left(-\frac{v^2}{s^2}\right), \\ \frac{d^6g}{dz^6} &= \left[\frac{64v^6}{s^{12}} - \frac{480v^4}{s^{10}} + \frac{720v^2}{s^8} - \frac{120}{s^6}\right] \exp\left(-\frac{v^2}{s^2}\right), \\ \frac{d^7g}{dz^7} &= \left[-\frac{128v^7}{s^{14}} + \frac{1344v^5}{s^{12}} - \frac{3360v^3}{s^{10}} + \frac{1680v}{s^8}\right] \exp\left(-\frac{v^2}{s^2}\right), \\ \frac{d^8g}{dz^8} &= \left[\frac{256v^8}{s^{16}} - \frac{3584v^6}{s^{14}} + \frac{13440v^4}{s^{12}} - \frac{13440v^2}{s^{10}} + \frac{1680}{s^8}\right] \exp\left(-\frac{v^2}{s^2}\right), \\ \frac{d^9g}{dz^9} &= \left[-\frac{512v^9}{s^{18}} + \frac{9216v^7}{s^{16}} - \frac{48348v^5}{s^{14}} + \frac{80640v^3}{s^{12}} - \frac{30240v}{s^{10}}\right] \exp\left(-\frac{v^2}{s^2}\right). \end{aligned} \tag{A.5}$$

## B Fourier series of displaced circle and ellipse

Analysis of multipole field components arising due to perturbations discussed in chapter 6 and 7 can be explored from a pure geometrical point of view. It is necessary to introduce equations of a circle and an ellipse in polar coordinates. In the case of a displaced circle with radius  $\rho$  and center in  $(a, 0)$  (figure B.1, left), the equation is

$$r(\varphi) = a \cos \varphi + \sqrt{\rho^2 - \frac{a^2}{2} + \frac{a^2}{2} \cos 2\varphi}. \quad (\text{B.1})$$

For an ellipse with center in the origin  $(0, 0)$ , major semiaxis  $\rho + e$ , and minor semiaxis  $\rho - e$  (figure B.1, right), the equation is

$$r(\varphi) = \frac{\rho^2 - e^2}{\sqrt{\rho^2 + e^2 + 2\rho e \cos 2\varphi}}. \quad (\text{B.2})$$

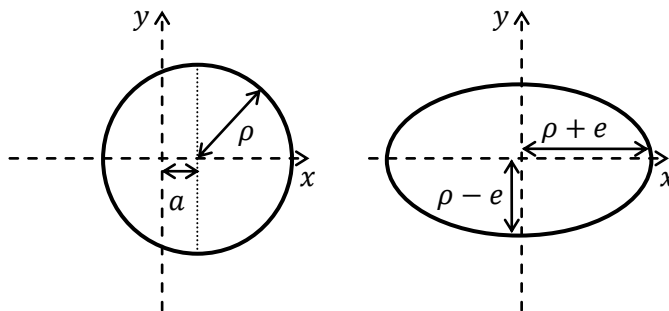


**Figure B.1:** Displaced circle with radius  $\rho$  and center in  $(a, 0)$  (left), ellipse with center in the origin, major semiaxis  $\rho + e$ , and minor semiaxis  $\rho - e$  (right).

Coefficients of the Fourier series are calculated as

$$\begin{aligned} C_0 &= \frac{1}{2\pi} \int_0^{2\pi} r(\varphi) d\varphi, \\ C_m &= \frac{1}{\pi} \int_0^{2\pi} r(\varphi) \cos(m\varphi) d\varphi. \end{aligned} \quad (\text{B.3})$$

The analysis is performed in Maple [51]. Non-zero Fourier coefficients up to  $m = 5$  for different perturbation parameters  $a$  and  $e$  from 0 to 100  $\mu\text{m}$  are shown in figure B.2. Parameter  $\rho$  is equal to 1 mm. These parameters are chosen similarly to the parameters

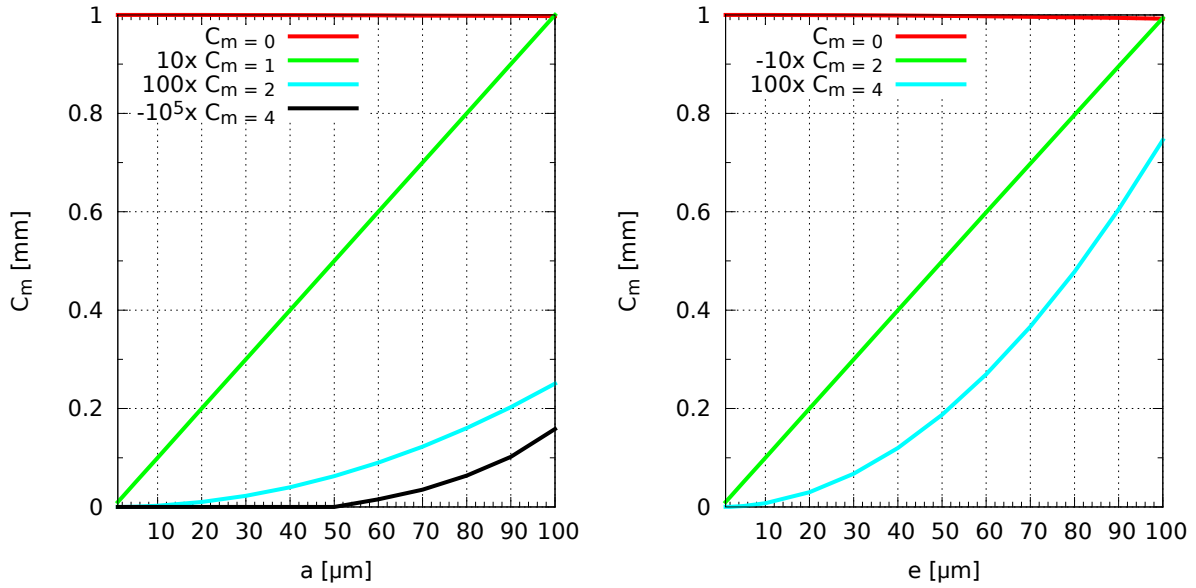


**Figure B.2:** Dependency of non-zero Fourier coefficients up to  $m = 5$  for the displaced circle (left) and the ellipse (right) on the displacement and elliptic parameters  $a$  and  $e$ . Radius of the circle  $\rho$  is 1 mm.

of lens pole pieces discussed in chapter 7. A tilt is similar to a misalignment — the only difference is, that the parameter  $a$  is not constant, but depends on the  $z$  coordinate along the optical axis.

According to these results, a misalignment and a tilt causes parasitic dipole, quadrupole field, and really weak and negligible octupole field. An ellipticity causes parasitic quadrupole and octupole field. It is not necessary to explore higher order multipole fields, because their effects would be insignificant, which is confirmed, for example, in figure 6.8 on page 45, where not so weak octupole field has no visible effect on particle trajectories, which is in agreement with [10]. Consequently, a suitable approximation is substituting misalignments and tilts by parasitic dipole and quadrupole field, and ellipticities by parasitic quadrupole field.

# C Modification of the wavelet interpolation for 2D fields

The algorithm introduced in section 5.3 can be easily modified to evaluate the axial field and its high order derivatives from calculated 2D fields. An application of the wavelet interpolation to 2D fields is illustrated on the unperturbed magnetic objective lens of K. Tsuno [43] (figure 4.2 on page 28), discussed in section 4.3.

In the case of the rotationally symmetric magnetic field, the magnetic flux  $\Phi_B$  is solved by EOD [36] in  $Q$  mesh points. Using (5.6) with respect to power series (3.23)

$$\begin{aligned}\Phi_B(r, z) &\approx \sum_{j=1}^J \sum_{i=0}^{N-1} (-1)^i \frac{2\pi}{(2i+2)4^i(i!)^2} \frac{d^{2i+1}}{dz^{2i+1}} \left\{ \exp \left[ -\frac{(z-z_j)^2}{(\sigma d_z)^2} \right] \right\} r^{2i+2} A_{0,j} \\ &= \sum_{j=1}^J K_{j,N} A_{0,j}.\end{aligned}\tag{C.1}$$

Unknown parameters  $A_{0,j}$  are calculated by the least squares fit. In the matrix notation

$$\mathbf{A} = (\mathbf{M}' \cdot \mathbf{M}) \backslash \mathbf{M}' \cdot \mathbf{F},\tag{C.2}$$

with  $\mathbf{A}$  as the vector of length  $J$  including the unknown parameters  $A_{0,j}$ ,  $\mathbf{M}$  as the matrix of size  $Q \times J$  including the coefficients  $K_{j,N}$  from equation (C.1), and  $\mathbf{F}$  as the vector of length  $Q$  consisting of the magnetic flux  $\Phi_B(r, z)$ . The matrices are

$$\mathbf{A} = \begin{bmatrix} A_{0,1} \\ A_{0,2} \\ \dots \\ A_{0,J} \end{bmatrix}, \mathbf{F} = \begin{bmatrix} \Phi_B(r_1, z_1) \\ \Phi_B(r_2, z_2) \\ \dots \\ \Phi_B(r_Q, z_Q) \end{bmatrix},\tag{C.3}$$

$$\mathbf{M} = \begin{bmatrix} K_{1,N}(r_1, z_1) & K_{2,N}(r_1, z_1) & \dots & K_{J,N}(r_1, z_1) \\ K_{1,N}(r_2, z_2) & K_{2,N}(r_2, z_2) & \dots & K_{J,N}(r_2, z_2) \\ \dots & \dots & \dots & \dots \\ K_{1,N}(r_Q, z_Q) & K_{2,N}(r_Q, z_Q) & \dots & K_{J,N}(r_Q, z_Q) \end{bmatrix}.$$

The vector  $\mathbf{S}$  of the standard deviations  $SD(A_{0,j})$  is calculated as

$$\mathbf{S} = \sqrt{\frac{(\mathbf{M} \cdot \mathbf{A} - \mathbf{F}') \cdot (\mathbf{M} \cdot \mathbf{A} - \mathbf{F})}{Q - J}} \sqrt{\text{diag}(\text{inv}(\mathbf{M}' \cdot \mathbf{M}))}.\tag{C.4}$$

Finally, the axial field  $B_0$  is evaluated according to equation (5.6), its standard deviations using (5.13), and any of its derivative via (5.11).

The axial field and its first seven derivatives of the unperturbed magnetic objective lens are smooth (figure C.1), which is necessary for further analysis of optical properties and aberrations.

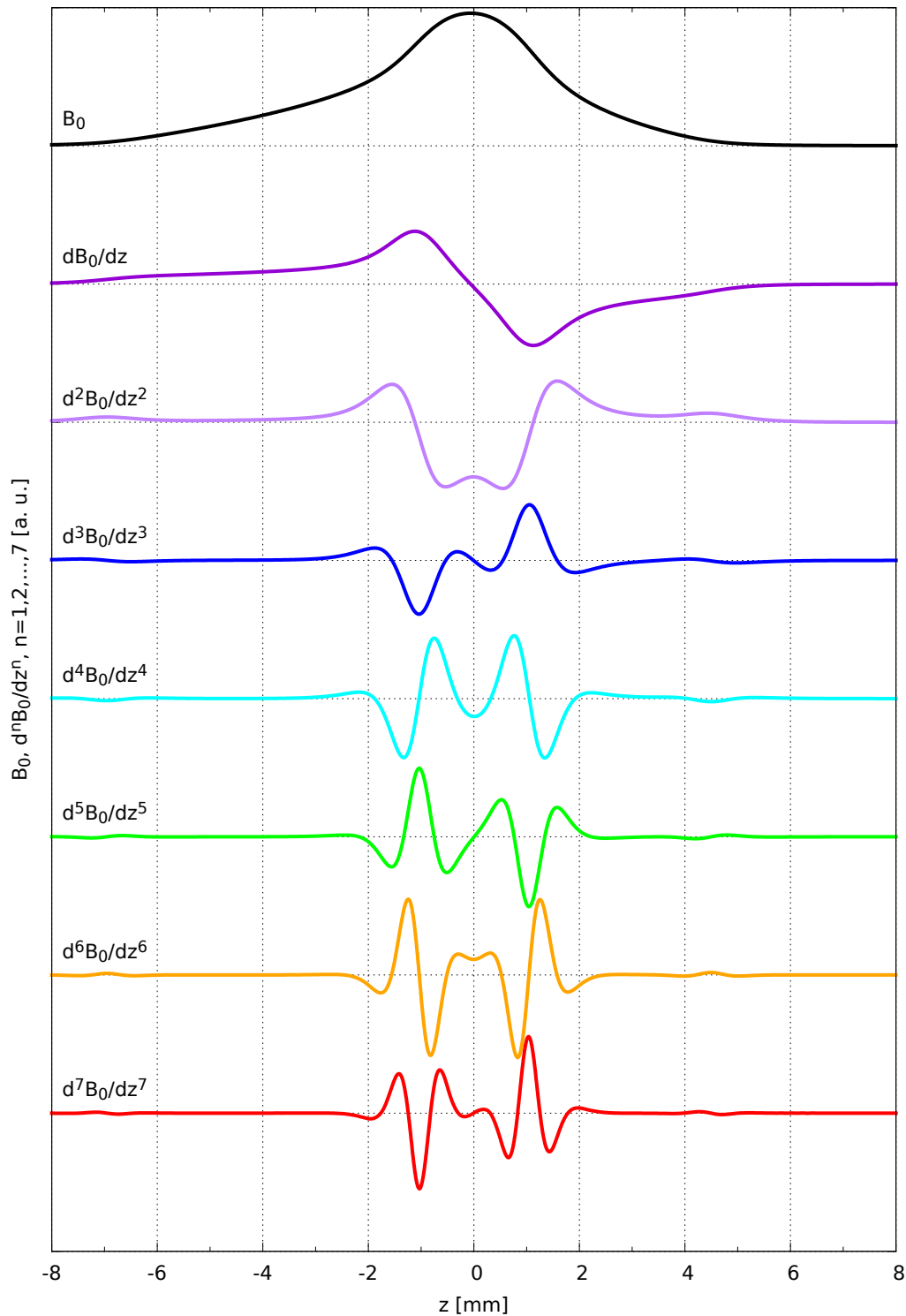


**Figure C.1:** Axial field  $B_0$  of the magnetic objective lens of Tsuno [43] and its first seven derivatives. The excitation of the lens is 10 500 A-turns, which corresponds to the performance of the objective lens in the 200 kV scanning transmission electron microscope.

# References

- [1] DELLBY, N.; et al. Tuning High Order Geometric Aberrations in Quadrupole-Octupole Correctors. *Microscopy and Microanalysis*, 2014, vol. 20, supplement 3, p. 928–929. ISSN 1431-9276.
- [2] SHÁNĚL, O. *Tolerances and misalignment aberrations for electron optical elements and systems* (doctoral thesis). Brno: Brno University of Technology, Faculty of Mechanical Engineering, 2014, 87 p.
- [3] SHÁNĚL, O.; ZLÁMAL, J.; ORAL, M. Calculation of the performance of magnetic lenses with limited machining precision. *Ultramicroscopy*, 2014, vol. 137, p. 1–6. ISSN 0304-3991.
- [4] HORÁK, M.; ZLÁMAL, J. Accurate Interpolation of 3D Fields Close to the Optical Axis. *Proceedings of the 9th International Conference on Charged Particle Optics*. To be published.
- [5] ZLÁMAL, J.; LENCOVÁ, B. Influence of Saturation of Magnetic Lens Material on Fields of Deflectors and Parasitic Fields. *Proceedings of the 9th International Conference on Charged Particle Optics*. To be published.
- [6] GLASER, W. Über elektronenoptische Abbildung bei gestörter Rotationsymmetrie. *Zeitschrift für Physik*, 1943, vol. 120, p. 1–15. ISSN 0044-3328.
- [7] HILLIER, J.; RAMBERG, E. G. The Magnetic Electron Microscope Objective: Contour Phenomena and the Attainment of High Resolving Power. *Journal of Applied Physics*, 1947, vol. 18, p. 48–71. ISSN 0021-8979.
- [8] HAWKES, P. W.; KASPER, E. *Principles of Electron Optics: Volume 1, Basic Geometrical Optics*. London: Academic Press Limited, 1996. ISBN 978-0-12-333340-7.
- [9] ORLOFF, J. *Handbook of Charged Particle Optics*. Boca Raton: CRC Press, 2009. ISBN 978-1-4200-4554-3.
- [10] BERTEIN, F. Influence des défauts de forme d’une électrode simple en optique électronique. *Journal de Physique et le Radium*, 1948, vol 9, p. 104–112.
- [11] STURROCK, P. A. The aberrations of magnetic electron lenses due to asymmetries. *Philosophical Transactions of the Royal Society A*, 1951, vol. 243, p. 387–429. ISSN 1471-2962.
- [12] ZLÁMAL, J.; LENCOVÁ, B. Development of the program EOD for design in electron and ion microscopy. *Nuclear Instruments and Methods in Physics Research A*, 2011, vol. 645, p. 278–282. ISSN 0168-9002.

- [13] *COMSOL Multiphysics* [online]. [cit. 2014-11-21] <<http://www.comsol.com/>>
- [14] GLASER, W. *Grundlagen der Elektronenoptik*. Wien: Springer-Verlag, 1952. ISBN 978-3-23620-8.
- [15] HAWKES, P. W. *Magnetic Electron Lenses*. Berlin: Springer-Verlag, 1982. ISBN 3-540-10296-5.
- [16] YAVOR, M. I. Methods for Calculation of Parasitic Aberrations and Machining Tolerances in Electron Optical Systems. *Advances in Electronics and Electron Physics*, 1993, vol. 86, p. 225–281. ISBN 0-12-014728-9.
- [17] ROUSE, J. Three-dimensional computer modeling of electron optical systems. *Advances in Optical and Electron Microscopy*, 1994, vol. 13, p. 1–121. ISBN 0-12-029913-5.
- [18] ROSE, H. H. *Geometrical Charged-Particle Optics*. Berlin: Springer-Verlag, 2009. ISBN 978-3-540-85915-4.
- [19] JANSE, J. Numerical treatment of electron lenses with perturbed axial symmetry. *Optik*, 1971, vol. 33, p. 270–281. ISSN 0030-4026.
- [20] MUNRO, E. Finite difference programs for computing tolerances for electrostatic lenses. *Journal of Vacuum Science & Technology B*, 1988, vol. 6, p. 941–948. ISSN 2166-2746.
- [21] LIU, H.; ZHU, X. Numerical computation of the error effect in electron beam focusing and deflection systems. *Optik*, 1990, vol. 84, p. 123–136. ISSN 0030-4026.
- [22] EDGCOMBE, C. J. On the perturbation of trajectories by small displacement of electrodes. *Optik*, 1991, vol. 86, p. 120–128. ISSN 0030-4026.
- [23] WEI, L.; HANCHUN, Y. Perturbation of trajectory caused by small displacement of electrode. *Nuclear Instruments and Methods in Physics Research A*, 1999, vol. 420, p. 369–379. ISSN 0168-9002.
- [24] WEI, L.; YAN, T. Determination of the acceptable tolerance in the manufacture of electron optical system. *Nuclear Instruments and Methods in Physics Research A*, 1999, vol. 427, p. 393–398. ISSN 0168-9002.
- [25] ARCHARD, G. D. Magnetic electron lens aberrations due to mechanical defects. *Journal of Scientific Instruments*, 1953, vol. 30, p. 352–358. ISSN 0950-7671.
- [26] AMBOSS, K.; JENNINGS, J. C. E. Electron-Optical Investigation of the Origin of Asymmetries in Air-Cored Solenoids. *Journal of Applied Physics*, 1970, vol. 41, p. 1608–1616. ISSN 0021-8979.
- [27] BARANOVA, L. A.; READ, F. H. Aberrations caused by mechanical misalignments in electrostatic quadrupole lens system. *Optik*, 2001, vol. 112, no. 3, p. 131–138. ISSN 0030-4026.
- [28] BATSON, P. E. Control of parasitic aberrations in multipole optics. *Journal of Electron Microscopy*, 2009, vol. 58, no. 3, p. 123–130. ISSN 2050-5698.

- [29] GRIME, G.W.; et al. Real and parasitic aberrations of quadrupole probe-forming systems. *Nuclear Instruments and Methods*, 1982, vol. 197, p. 97–109. ISSN 0168-9002.
- [30] TSUMAGARI, T.; et al. Aberration of electrostatic systems with machining error. *Journal of Vacuum Science & Technology B*, 1986, vol. 4, p. 140–142. ISSN 2166-2746.
- [31] OZAKI, T.; HISAOKA, Y. H.; MURAKAMI, H. Approximation formula for parasitic aberrations due to mechanical defects of an electrostatic deflector. *Microelectronic Engineering*, 1993, vol. 21, p. 217–220. ISSN 0167-9317.
- [32] KURIHARA, K. Aberration due to misalignment in electrostatic lens and deflection systems. *Journal of Vacuum Science & Technology B*, 1990, vol. 8, p. 452–455. ISSN 2166-2746.
- [33] YAVOR, M. I.; BERDNIKOV, A. S. Parasitic aberrations in static sector field mass analyzers and their correction. Part 1. First order approximation. *International Journal of Mass Spectrometry and Ion Processes*, 1993, vol. 128, p. 149–156. ISSN 1387-3806.
- [34] GRIFFITHS, D. J.; COLLEGE, R. *Introduction to Electrodynamics*. New Jersey: Prentice Hall, 1999. ISBN 0-13-805326-X.
- [35] VANDERLINDE, J. *Classical Electromagnetic Theory*. Dordrecht: Kluwer Academic Publishers, 2004. ISBN 1-4020-2699-4.
- [36] LENCOVÁ, B.; ZLÁMAL, J. A new program for the design of electron microscopes. *Physics Procedia*, 2008, vol. 1, p. 315–324. ISSN 1875-3892.
- [37] *CPO Charged Particle Optics* [online]. [cit. 2014-11-21] <<http://www.electronoptics.com/>>
- [38] *SIMION Ion and Electron Optics Simulator* [online]. [cit. 2014-11-21] <<http://simion.com/>>
- [39] *Field Precision LCC: Finite-element Software for Electromagnetics* [online]. [cit. 2014-11-21] <<http://www.fieldp.com/>>
- [40] *INTEGRATED Engineering Software* [online]. [cit. 2014-11-21] <<https://www.integratedsoft.com/>>
- [41] *Munro's Electron Beam Software Ltd.* [online]. [cit. 2014-11-21] <<http://www.mebs.co.uk/>>
- [42] ROUSE, J.; MUNRO, E. Three-dimensional computer modeling of electrostatic and magnetic electron optical components. *Journal of Vacuum Science & Technology B*, 1989, vol. 7, p. 1891–1897. ISSN 2166-2746.
- [43] KATO, M.; TSUNO, K. Optimization of electron lens shape giving minimum spherical aberration coefficient. *IEEE Transactions on Magnetics*, 1990, vol. 26, p. 1023–1026. ISSN 0018-9464.

- [44] RADLIČKA, T.; LENCOVÁ, B. Determination of analytical expansion from numerical field data. *Ultramicroscopy*, 2010, vol. 110, p. 1198–1204. ISSN 0304-3991.
- [45] *MATLAB – The Language of Technical Computing* [online]. [cit. 2014-10-23] <<http://www.mathworks.com/products/matlab/>>
- [46] ORAL, M. *Určení přesných trajektorií nabitých částic a vad soustav v částicové optice* (dizertační práce). Brno: Masarykova univerzita, Přírodovědecká fakulta, 2009, 101 s.
- [47] BERZ, M. *Modern Map Methods in Particle Beam Physics*. Academic Press: London, 1999. ISBN 0-12-014750-5.
- [48] MAKINO, K.; BERZ, M. COSY INFINITY version 8. *Nuclear Instruments and Methods in Physics Research A*, 1999, vol. 427, p. 338–343. ISSN 0168-9002.
- [49] LIU, Z. Differential algebraic method for aberration analysis of typical electrostatic lenses. *Ultramicroscopy*, 2006, vol. 106, p. 220–232. ISSN 0304-3991.
- [50] ORAL, M.; LENCOVÁ, B. Calculation of aberration coefficients by ray tracing. *Ultramicroscopy*, 2009, vol. 109, p. 1365–1373. ISSN 0304-3991.
- [51] *Maple 2015 – Technical Computing Software for Engineers, Mathematicians, Scientists, Instructors and Students – Maplesoft* [online]. [cit. 2015-5-5] <<http://www.maplesoft.com/products/maple/>>

# List of symbols

$x, y, z$	Cartesian coordinates
$r, \varphi, z$	cylindrical coordinates
$\phi'(z) = \frac{\partial \phi}{\partial z}$	derivative with respect to $z$
$\Delta$	Laplace operator
	in cylindrical coordinates $\Delta = \frac{\partial^2}{\partial r^2} + \frac{1}{r} \frac{\partial}{\partial r} + \frac{1}{r^2} \frac{\partial^2}{\partial \varphi^2} + \frac{\partial^2}{\partial z^2}$
$\vec{E} = (E_r, E_\varphi, E_z)$	electric field/electric field intensity
$\Phi$	electrostatic potential
$\vec{H} = (H_r, H_\varphi, H_z)$	magnetic field intensity/magnetic field strength
$\vec{B} = (B_r, B_\varphi, B_z)$	magnetic flux density/magnetic induction
$\vec{A} = (A_r, A_\varphi, A_z)$	magnetic vector potential
$\Phi_B$	magnetic flux
$\Psi$	scalar magnetic potential
$\mu_0$	vacuum permeability/magnetic constant ( $\mu_0 = 4\pi \cdot 10^{-7} \text{ H m}^{-1}$ )
$\mu_r$	relative permeability
$m$	$m$ -th multipole; $m = 1$ dipole, $m = 2$ quadrupole, ...
$M$	the highest multipole component used in calculation
$N$	number of terms in series
$i, n$	index of term in series
$\Phi_m$	$m$ -th multipole electrostatic potential
$F_m$	$m$ -th multipole electrostatic potential with separated angular dependency
$\phi_0$	axial electrostatic potential of rotationally symmetric field
$f_m$	axial $m$ -th multipole electrostatic field function
$B_0$	axial magnetic flux density of rotationally symmetric field
$\Psi_m$	$m$ -th multipole scalar magnetic potential
$\psi_m$	axial $m$ -th multipole reduced scalar magnetic potential
$D_m = -\mu_0 \psi_m$	axial $m$ -th multipole magnetic field function
$\vec{s}$	vector of surface deformation
$\alpha$	rotation of the perturbation
$e$	ellipticity
$a$	misalignment
$t$	tilt
$Z$	number of $z$ positions in the algorithm based on the Fourier series expansion
$R$	number of circles in every $z$ position in the algorithm based on the Fourier series expansion
$C_{\{r,\varphi,z\},m}$	Fourier coefficients
<b>A</b>	vector of unknown parameters

<b>M</b>	matrix of coefficients
<b>F</b>	vector of Fourier coefficients, respectively field components
<b>S</b>	vector of standard deviations
$SD(B_0)$	standard deviation of $B_0$
$z_j$	node points of the base Gaussian function
$J$	number of node points of the base Gaussian function
$A_{m,j}$	amplitudes of the base Gaussian function
$\sigma$	parameter determining the width of the base Gaussian function
$d_z$	distance between two nearby node points of the base Gaussian function
$K_{\{r,\varphi,z\},m,j,N}$	coefficients used in the algorithm based on the wavelet interpolation
$P$	number of points with known field used in the algorithm based on the wavelet interpolation
$L$	number of circles used in the combined algorithm
$z_t$	cross-section of tilt axis an $z$ -axis
$z_o$	$z$ coordinate of the object plane
$z_i$	$z$ coordinate of the Gaussian image plane
$w_i = x_i + iy_i$	complex position of the particle in the Gaussian image plane
$\omega_i$	complex slope of the trajectory at the Gaussian image plane
$\gamma_i$	deflection in the Gaussian image plane
$L_D$	coma of deflection
$A_D$	astigmatism of deflection
$C_F$	defocus with field curvature
$C_S$	spherical aberration
$\rho$	radius of the circle
$Q$	number of mesh points in the area of interest used in the modification of the wavelet interpolation for 2D fields
$K_{j,N}$	coefficients used in the modification of the wavelet interpolation for 2D fields

# List of figures

4.1	Three types of mechanical imperfections — (a) ellipticity, (b) misalignment, and (c) tilt, using nomenclature as in [3, 20], respectively (a) elliptic distortion, (b) eccentricity, and (c) orientation, using nomenclature by Sturrock [11]. Dotted lines show ideal unperturbed lenses, solid lines the perturbed lenses. . . . .	27
4.2	200 kV magnetic objective lens – pole pieces (red), yoke (blue), coil (green). Bore diameter and gap are both 2 mm. . . . .	28
5.1	Components of the field are evaluated in points on $R$ concentric circles. . .	30
5.2	Magnetic lens with the hole drilled perpendicular to the optical axis – hole (yellow), pole pieces (red), yoke (blue), coil (green). . . . .	36
5.3	Axial field functions of the magnetic objective lens with the hole in the pole piece determined by three discussed methods – method based on the Fourier series expansion (green points), method based on the wavelet interpolation (red solid lines), and the combined method (black dashed line). . . . .	37
5.4	The first three derivatives of the axial field functions of the magnetic objective lens with the hole in the pole piece evaluated by the combined algorithm. . . . .	38
6.1	Magnetic lens with an elliptic pole piece – coil (green), yoke (blue), pole pieces (red), perturbed part of pole piece (light blue). Bore diameter and gap are both 2 mm. . . . .	39
6.2	Comparison of the axial magnetic flux density of the magnetic objective lens and the magnetic objective lens with modified shape of pole pieces for two excitations. . . . .	40
6.3	Fine mesh of the magnetic lens in COMSOL Multiphysics. The undistinguishable black region corresponds to the area of the smallest mesh elements in the gap region, which is shown in detail on the right. Polepieces in the detailed view are red coloured. . . . .	40
6.4	Seventh derivative of the quadrupole axial field function for different values of $d_z$ . The second parameter $\sigma = 2$ is fixed. The functions are shifted with step of $100 \text{ T mm}^{-8}$ . The ellipticity of upper pole piece is $100 \mu\text{m}$ , and the excitation of the lens is $1000 \text{ A-turns}$ . . . . .	42
6.5	Seventh derivative of the quadrupole axial field function for different values of $\sigma$ . The second parameter is fixed to $d_z = 0.12 \text{ mm}$ . The functions are shifted with step of $100 \text{ T mm}^{-8}$ . The ellipticity of upper pole piece is $100 \mu\text{m}$ , and the excitation of the lens is $1000 \text{ A-turns}$ . . . . .	42

6.6	Axial field functions and its first seven derivatives for the rotationally symmetric (left) and quadrupole (right) field using $d_z = 0.12$ mm and $\sigma = 2.2$ . The ellipticity of upper pole piece is $100 \mu\text{m}$ , and the excitation of the lens is $1\,000$ A-turns. . . . .	43
6.7	Comparison of the axial field functions evaluated from the 3D field and computed using the 2D perturbation theory of the lens with the ellipticity of upper pole piece of $100 \mu\text{m}$ and the excitation of $1\,000$ A-turns. . . . .	44
6.8	Comparison of positions of electrons in the Gaussian image plane $z_i = 0$ mm calculated using the axial field functions evaluated from the 3D field without the octupole component (green), including the octupole component (blue), and calculated using the axial field functions computed by the perturbation theory (red). . . . .	45
6.9	Comparison of fitted (red) and traced (green) positions of electrons in the Gaussian image plane using the axial field functions evaluated from the 3D field. The magnetic lens pole piece ellipticity is $100 \mu\text{m}$ and the excitation of the lens is $1\,000$ A-turns. . . . .	46
7.1	Rotationally symmetric axial field components $B_0$ for different exciations of the lens computed using 2D (dotted lines) and 3D calculation (solid lines). . . . .	48
7.2	Maxima of the rotationally symmetric axial field components $B_0$ for different exciations of the lens. If the lens is not saturated, the maximum of $B_0$ is linear to the excitation. The linear dependence, shown by the green line, is extrapolated from the maximum of $B_0$ for the excitation of $1\,000$ A-turns. . . . .	48
7.3	Quadrupole axial field functions $D_2$ for different exciations of the under-saturated lens computed using 2D perturbation theory (dotted lines) and 3D calculation (solid lines). The ellipticity of the pole piece is $2 \mu\text{m}$ . . . . .	50
7.4	Quadrupole axial field functions $D_2$ for different exciations of the saturated lens computed using 2D perturbation theory (dotted lines) and 3D calculation (solid lines). The ellipticity of the pole piece is $2 \mu\text{m}$ . . . . .	50
7.5	Quadrupole axial field functions $D_2$ for different values of the ellipticity computed using 2D perturbation theory (dotted lines) and 3D calculation (solid lines). The excitation of the lens is $1\,000$ A-turns. . . . .	52
7.6	Two-fold axial astigmatism size $ A_1 $ calculated by the least square fit as a function of the ellipticity. Linear dependency is extrapolated from the $ A_1 $ for the ellipticity of $2 \mu\text{m}$ . The excitation of the lens is $1\,000$ A-turns. . . . .	53
7.7	Octupole axial field functions $D_4$ for different values of the ellipticity evaluated from the 3D solution of the field. The excitation of the lens is $1\,000$ A-turns. . . . .	53
7.8	Dipole axial field functions $D_1$ for different values of the misalignment computed using 2D perturbation theory (dotted lines) and 3D calculation (solid lines). The excitation of the lens is $1\,000$ A-turns. . . . .	54
7.9	Coma size $ L_D\gamma_i $ (left) and astigmatism size $ A_D\gamma_i^2 $ (right) as a function of misalignment. Linear dependency is extrapolated from the $ L_D\gamma_i $ for the misalignment of $2 \mu\text{m}$ , respectively quadratic dependency is extrapolated from the $ A_D\gamma_i^2 $ for the misalignment of $2 \mu\text{m}$ . The excitation of the lens is $1\,000$ A-turns. . . . .	56
7.10	Quadrupole axial field functions $D_2$ for different magnitudes of the misalignment evaluated from the 3D solution of the field. The excitation of the lens is $1\,000$ A-turns. . . . .	56

7.11	Dipole axial field functions $D_1$ for different values of the tilt computed using 2D perturbation theory (dotted lines) and 3D calculation (solid lines). The axis of tilted pole piece intersects the $z$ -axis in $z_t = 0$ mm. The excitation of the lens is 1 000 A-turns. . . . .	58
7.12	Coma size $ L_D\gamma_i $ (left) and astigmatism size $ A_D\gamma_i^2 $ (right) as a function of tilt. Linear dependency is extrapolated from the $ L_D\gamma_i $ for the tilt of 2 mrad, respectively quadratic dependency is extrapolated from the $ A_D\gamma_i^2 $ for the tilt of 2 mrad. The axis of tilted pole piece intersects the $z$ -axis in $z_t = 0$ mm. The excitation of the lens is 1 000 A-turns. . . . .	59
7.13	Quadrupole axial field functions $D_2$ for different values of the tilt evaluated from the 3D solution of the field. The axis of tilted pole piece intersects the $z$ -axis in $z_t = 0$ mm. The excitation of the lens is 1 000 A-turns. . . . .	60
B.1	Displaced circle with radius $\rho$ and center in $(a, 0)$ (left), ellipse with center in the origin, major semiaxis $\rho + e$ , and minor semiaxis $\rho - e$ (right). . . . .	67
B.2	Dependency of non-zero Fourier coefficients up to $m = 5$ for the displaced circle (left) and the ellipse (right) on the displacement and elliptic parameters $a$ and $e$ . Radius of the circle $\rho$ is 1 mm. . . . .	68
C.1	Axial field $B_0$ of the magnetic objective lens of Tsuno [43] and its first seven derivatives. The excitation of the lens is 10 500 A-turns, which corresponds to the performance of the objective lens in the 200 kV scanning transmission electron microscope. . . . .	70

# List of tables

4.1	Comparison of the computation in 2D and 3D. . . . .	28
6.1	Selected aberration coefficients ( $C_S$ and $A_1$ ) of the magnetic lens with ellipticity of $100\ \mu\text{m}$ and excitation of $1\ 000\ \text{A-turns}$ . . . . .	46
7.1	Optical properties of the magnetic lens for different excitations calculated using EOD software. Object and image planes of the lens are $z_o = -130\ \text{mm}$ and $z_i = 0\ \text{mm}$ . . . . .	47
7.2	Relative permeability $\mu_r$ of the material near the pole piece tip and difference in the maxima of the quadrupole axial field functions $D_2$ of the magnetic lens with an elliptic pole piece for different excitations of the lens. The ellipticity of the lens is $2\ \mu\text{m}$ . . . . .	49
7.3	Size of two-fold axial astigmatism aberration coefficients $ A_1 $ caused by the quadrupole field component of the magnetic lens with an elliptic pole piece for different excitations of the lens calculated by the fit. The ellipticity of the lens is $2\ \mu\text{m}$ . . . . .	51
7.4	Size of two-fold axial astigmatism aberration coefficients $ A_1 $ caused by the quadrupole field component of the magnetic lens with an elliptic pole piece for different magnitudes of ellipticity calculated by the least square fit. The excitation of the lens is $1\ 000\ \text{A-turns}$ . . . . .	52
7.5	Beam deflection $\gamma_i$ of the magnetic lens with a misaligned pole piece for different magnitudes of misalignment. The excitation of the lens is $1\ 000\ \text{A-turns}$ . . . . .	55
7.6	Coma size $ L_D\gamma_i $ of the lens with a misaligned pole piece for different magnitudes of misalignment. The excitation of the lens is $1\ 000\ \text{A-turns}$ . . . . .	55
7.7	Astigmatism size $ A_D\gamma_i^2 $ of the magnetic lens with a misaligned pole piece for different magnitudes of misalignment. The excitation of the lens is $1\ 000\ \text{A-turns}$ . . . . .	55
7.8	Size of two-fold axial astigmatism aberration coefficients $ A_1 $ caused by the quadrupole field component, evaluated from the 3D field of the magnetic lens with a misaligned pole piece, for different magnitudes of misalignment calculated by the least square fit. The excitation of the lens is $1\ 000\ \text{A-turns}$ . . . . .	57
7.9	Beam deflection $\gamma_i$ of the magnetic lens with a tilted pole piece for different magnitudes of tilt. The axis of tilted pole piece intersects the $z$ -axis in $z_t = 0\ \text{mm}$ . The excitation of the lens is $1\ 000\ \text{A-turns}$ . . . . .	58
7.10	Coma size $ L_D\gamma_i $ of the magnetic lens with a tilted pole piece for different magnitudes of tilt. The axis of tilted pole piece intersects the $z$ -axis in $z_t = 0\ \text{mm}$ . The excitation of the lens is $1\ 000\ \text{A-turns}$ . . . . .	59

7.11	Astigmatism size $ A_D \gamma_1^2 $ of the magnetic lens with a tilted pole piece for different magnitudes of tilt. The axis of tilted pole piece intersects the $z$ -axis in $z_t = 0$ mm. The excitation of the lens is 1 000 A-turns. . . . .	59
7.12	Size of two-fold axial astigmatism aberration coefficients $ A_1 $ caused by the quadrupole field component, evaluated from the 3D field of the magnetic lens with a tilted pole piece, for different magnitudes of tilt. The axis of tilted pole piece intersects the $z$ -axis in $z_t = 0$ mm. The excitation of the lens is 1 000 A-turns. . . . .	60